Department of
Industrial Engineering

XXXVI cycle

Doctoral School in Materials, Mechatronics
and System Engineering

Pushing Forward Distributed Positioning Systems: Unleashing the Potential of Ultrawide-Band Networks

Luca Santoro

April 2024

To my father... who never saw this adventure...

Pushing Forward Distributed Positioning Systems: Unleashing the Potential of Ultrawide-Band Networks

Luca Santoro

e-mail: luca.santoro@unitn.it

Supervisor:

Professor Daniele Fontanelli
Professor Davide Brunelli
Dept. of Industrial Engineering
University of Trento, Italy

University of Trento

Department of Industrial Engineering

April 2024

University of Trento - Department of Industrial Engineering

Doctoral Thesis

Luca Santoro - April 2024
Published in Trento (Italy) - by University of Trento

Abstract

This doctoral thesis presents a comprehensive exploration of ultrawideband technology in addressing diverse challenges within localization systems. Beginning with the development of an innovative, cost-effective, and anonymous contact tracing solution for industrial environments during the COVID-19 pandemic, the research integrates ultra-wideband positioning, Bluetooth low-energy, and inertial measurement units. The subsequent sections delve into relative positioning systems, device-free localization, UWB bistatic radar sensors, and UAV-based tracking, showcasing novel methodologies and hardware implementations with promising outcomes. The work extends to groundbreaking approaches in deploying UWB infrastructure through self-deployable robots and cooperative positioning schemes using a UAV swarm. The contributions highlight versatility, cost-effectiveness, and scalability, opening new possibilities for applications in security, logistics, IoT services, and space exploration. In summary, this thesis represents a significant advancement in localization systems, offering practical solutions and paving the way for future research and applications.

Contents

Abstract **i**

Preface **1**

1 Unveiling the World of Indoor Positioning Systems: An Introductory Exploration **7**

1.1 Challenges of Indoor Positioning Systems 10
1.2 Indoor Positioning: Systems Performance Metrics 10
1.3 Indoor Positioning: Systems Technologies 12
1.4 Ultrawide-Band Indoor Positioning Systems 17
1.4.1 Basic Measuring Principles 18

2 Human-Centric Positioning Systems: Enhancing Spatial Awareness and Navigation **22**

2.1 The Absolute Localisation System's Role in Safeguarding Industrial Environments 31
2.1.1 Data analytics for COVID-friendly re-layout 31
2.1.2 Indoor localization System Architecture 34
Hardware 36
Software 36
2.1.3 Evaluation 39
2.2 Navigating Spaces: an UWB Relative Localisation System for Pedestrians with Ranging Information 40
2.2.1 Background and Problem Formulation 41
Problem formulation and solution overview . . 44
2.2.2 WhereAreYou: the WAY Algorithm 44

2.2.3 Uncertainty analysis . . . 47
2.2.4 Results . . . 48
Hardware Implementation . . . 49
Experimental results . . . 51
2.3 Beyond Devices: Harnessing Cost-Effective Bistatic Radar and Ultrawide-Band Radios in a Device-Free Localisation System . . . 52
2.3.1 Related Work . . . 53
2.3.2 Methodology . . . 54
DW1000 CIR estimate . . . 56
Proposed solution . . . 58
2.3.3 Experimental Setup . . . 59
Results . . . 59
2.4 Invisible Trails: Unveiling the Capabilities of a Tag-Less Ultrawide-Band Passive Tracking System . . . 61
2.4.1 Background and Problem Formulation . . . 62
Position estimation . . . 64
Problem formulation and solution overview . . . 65
2.4.2 Solution . . . 65
2.4.3 Experimental Results . . . 67
Hardware . . . 68
Results . . . 69
2.4.4 Crossing Channels: Assessing the Performance of UWB Bistatic Radar Sensors in an Across-Channels Evaluation . . . 71
Hardware . . . 71
Preliminary experimental results . . . 72
2.5 Overcoming Scalability Hurdles: UWB-based Indoor Positioning System with Infinite Scalability . . . 74
2.5.1 Measurement models . . . 75
2.5.2 Uncertainty Models Validation . . . 82
2.6 INFALLIBLE: Positioning Systems Enhancing Human Welfare . . . 95

3 Robot-Centric Positioning Systems: Enhancing Spatial Awareness and Navigation 98

3.1 Flight Dynamics: Exploring an Infrastructure-Less UWB-Based Leader-Follower System for Compact UAVs in a Relative Positioning Framework . . . 104

3.1.1 The Catch-Me-If-You-Can Solution . . . 105

Leader positioning solutions . . . 108

Kalman filter for tracking . . . 109

3.1.2 Characterisation and preliminary results . . . 111

UWB characterisation and calibration . . . 111

Simulation results . . . 113

Anchors distance . . . 113

Effect of bias on measurements . . . 113

Consistency of the position algorithms . . . 114

Validation . . . 115

Preliminary experimental results . . . 116

3.2 Optimizing Exploration: On-Line Deployment of Optimal Ranging Sensors for Robotic Exploration . . . 118

3.2.1 Background and Problem Formulation . . . 119

Problem formulation . . . 120

3.2.2 Anchors Deployment Algorithm . . . 123

Deploying Manoeuvres . . . 125

3.2.3 Uncertainty analysis . . . 128

Position Dilution of Precision . . . 128

Anchor deployment uncertainty . . . 128

3.2.4 Simulations and Experiments . . . 131

Experimental results . . . 134

3.3 Roaming the Red Planet: Revolutionizing Mars Exploration with Dynamic Mobile Infrastructure . . . 136

3.3.1 Background and Problem Formulation . . . 137

Problem formulation and solution overview . . . 139

3.3.2 Infrastructure Positioning . . . 140

3.3.3 Results . . . 142

Uncertainties evaluation . . . 143

Preliminary Hardware Implementation 147

4 Conclusion **148**

Bibliography **150**

List of Figures

1.1 Multilateration: positioning using four reference point. . . . 8
1.2 Number of scientific documents in the five-year period 2018 − 2023. 9
1.3 In (a) LoS condition, in (b) NLoS condition. 10
1.4 Categorazation for IPS. 13
1.5 Angle of arrival principles. 19
1.6 In (a) Time of arrivals principles; in (b) Time of difference arrivals principles. 20

2.1 In (a) the traditional UTDoA approach where the tag emits the broadcast message, thus limiting the scalability of the system. In (b) the implemented DTDoA approach, where the anchors emit the messages used by the entity to localisation awareness. 29
2.2 Wearable Sensor schematic block diagram. 35
2.3 ILS flowchart. On the left the wearable sensor's flowchart. On the right the infrastructure flowchart 37
2.4 Wearable Sensor prototype. 38
2.5 Power consumption trace of a single execution discovery and localization tasks exploiting only UWB radio. As can be noted, the tasks take around 25 ms to complete (without considering the INIT phase executed only once at startup). 39

2.6 Power consumption trace of a single execution of discovery and localization tasks exploiting both BLE and UWB. As can be noted, the tasks take around 600 ms to complete (without considering the INIT phase executed only once at startup). 40
2.7 Example of a report generated starting from the data provided by the proposed system. The orange track shows a tag that implements both discovery and localization using UWB, while the blue one is a tag with a mesh approach. The system detects real-time risk of contagion due to the small distance between employees. 41
2.8 MDS algorithm may generate an ambiguous map (purple squares), resulting in a wrong final reciprocal position reconstruction. 43
2.9 Geometry of the translation vector T: the displacement computed by the moving node 0 is equivalent to the shift of all the other nodes. Back-projecting T reconstruct the moving node displacements t_k and t_{k+1}. 45
2.10 Removing final ambiguity on the estimated map. Blue circles (N_i) represent the true map, while purple squares ($\overline{N}_i$) and green triangles ($'\overline{N}_i$) are the flipped solutions. Solution to (2.11) removes the set $\overline{N}_i$, while Corollary 2 removes the flipping given by $'\overline{N}_i$. 47
2.11 (a) Schematic block of the proposed device. (b) and (c) 3D rendering of the proposed device. 49
2.12 Scheduling protocol. 50
2.13 Experimental results. N (blue circles) represent the true position of the nodes retrieved from the MoCap, $\hat{P}$ (red squares)) represent instead the estimated position using the proposed system. True displacement of the moving node is denoted with s (dashed blue line), while $\hat{s}$ is the estimated displacement retrieved form the algorithm (dashed red line). 51

2.14 Bistatic radar configuration. τ_{LOS}^{FP} is the time of flight (ToF) in line-of-sight condition between receiver and transmitter, τ_T^{Rx} and τ_T^{Tx} is the ToF of the reflected signal between target and receiver and transmitter, respectively, τ_R the ToF with respect the centre of the bistatic radar and the target and τ_T is the major axis of the ellipse. 56
2.15 Different configuration for the bistatic radar, varying the values of the distance between the transmitter and the receiver. 57
2.16 Estimated target distance $c\tau_{TP}$ with target speed 0.13 $\frac{m}{s}$. . . 60
2.17 In (a) Estimated target distance $c\tau_{TP}$ with target speed 0.26 $\frac{m}{s}$; in (b) Estimated target distance $c\tau_{TP}$ with target speed 0.39 $\frac{m}{s}$. 60
2.18 Error on the estimated distance by the bistatic radar. The ground truth is a motion capture system power by Qualisys. 61
2.19 Representation of the detection area identified by anchors and transmitter. 64
2.20 Experimental setup 67
2.21 In (a) the developed prototype, in (b) the HW architecture. 68
2.22 In (a) comparison between the distance estimated by our approach (blue line) and distance retrieved by the motion capture (dashed-orange line), in (b) the histogram of the error. 69
2.23 Comparison between target path estimated by UWB and by the MoCap. 70
2.24 In (a) experimental setup. A single couple Tx-Rx oriented in the same direction. The receiver analyses CIR to identify the time delay of the target and computes the distance. The target performs various motion patterns within a range of 1-5 m. In (b) radar node prototype. 71
2.25 Bistatic radar for the "Z" shaped motion pattern of Figure 2.24-(a) with channel 9. (a,c) baseline 2.3 m, (b,d) baseline 4.3 m. (a,b) Tx power level 28.6 dBm/MHz, (c,d) low Tx power level 24.6 dBm/MHz. 73

2.26 (a,b) Channel 9 and baseline 4.3 m Square motion pattern of Figure 2.24-(a): (a) comparison between MoCap and UWB; (b) Histogram of the error. (c,d) UWB radar traces (collected simultaneously) with baseline 2.3 m and back and forth motion pattern of Figure 2.24-(a): (c) channel 5 (d) channel 9, power transmission level 24.6 dBm/MHz. 74
2.27 In (a), the estimated distance using the standard windowing approach on the old generation of UWB devices using channel 5. In (b), the new UWB generation devices using channel 9. Transmission power 24.6 dBm/MHz and baseline 2.3 m . 75
2.28 Indoor testing infrastructure. In the top, we show the MoCap cameras along with the UWB anchors and the acquisition chain. The bottom part depicts the effect of tag moving affecting reception's time instant and the spatial location of the 12 messages sent by the $n = 5$ reference anchors (the sixth is the master). Each message is received at a different time/space instant/location, causing the estimation shifting problem. The highlighted P_i locations show where the static tests were conducted. 83
2.29 Laboratory environment. In particular, the quadruped and barrier for the anthropomorphic robotic arm created the conditions for the multi-path effect and NLoS condition, respectively. 84
2.30 Histogram of the error for the dynamic test along the X_w (a) and Y_w (b) reference axes over 5000 repeated measurements. 89
2.31 Distribution of the error in the static positions of Figure 2.28 along the X_w (a) and Y_w (b) over 5000 repeated measurements. 90
2.32 Experimental setup inside the hall of the "Dipartimento Ingegneria Industriale" of the University of Trento. Inside the orange circle the receiver mounting point on the tester arm. 91
2.33 Graphical representation of the experimental setup, with the static testing point reported. 92

2.34 Dynamic test trajectories: 8-shape pattern (a) and Z-shape pattern (b). The trajectories are executed by the tester in the area depicted in Figure 2.32. 92
2.35 Distribution of the error in the static positions of Figure 2.28 along the X_w (a) and Y_w (b) over 5000 repeated measurements and with $\Delta_{i,m} = 16$ ms. 94
2.36 Graphical representation of the experimental setup, with the static testing point reported. 94
2.37 Dynamic test trajectory. The tester walks along a predefined path. 96
2.38 Bear Population Trend 97

3.1 Scenario: a swarm of UAVs that localise themselves and provides simultaneously a positioning services to humans and robots on the ground. This image was created with the assistance of DALL-E. 102
3.2 (a) UAV follower prototype. (b) Follower system architecture. On the left the three UWB radios along with the RPi 4 companion board. The master DWM1001C is in charge of collecting the data from the other UWB radios and stream them to the RPi 4. On the right the UAV avionics. Companion board to flight controller communication is implemented using a MAVLINK. 105
3.3 Reference systems considered for the leader-follower application. The blue circles represent the positions of the three UWB anchors, all expressed in the depicted UAV reference frame $\langle U \rangle$. 106
3.4 Position of the UAV desired position $\mathbf{p}_d$, which is computed using two consecutive KF position estimates $\hat{\mathbf{p}}_{f,k+1}$ and $\hat{\mathbf{p}}_{f,k}$. 111
3.5 (a) Distance measured by $\mathbf{a}_1$ (red line) and the actual distance (blue line) to infer the bias $\beta_1(\overline{\rho}_1)$. (b) Error histogram of $\overline{\rho}_1 - \rho_1$ after the bias in Table 3.1 has been compensated. 112

3.6 Average position error $\|\mathbf{p}_r - \hat{\mathbf{p}}_r\|$ of the Monte Carlo simulations for different values of the baseline b and for both the LLS and the NLSS solutions. 114
3.7 Histogram of the position error $\|\mathbf{p}_r - \hat{\mathbf{p}}_r\|$ for the NLLS and LLS solutions with a bias $\beta_i = 0.2$ m. 115
3.8 Distributions of error $e_x = x - \hat{x}$ and $e_y = y - \hat{y}$ for the solutions with $N_{rep} = \{1, 25\}$. 116
3.9 (a) Gazebo simulation environment with the UAV (a quadrotor) and the target (represented by the red cylinder). (b) The path traveled by the target. 116
3.10 Histogram of the tracking error $x - \hat{x}_f$ and $y - \hat{y}_f$ returned by the KF. 117
3.11 Preliminary outdoor test. 117
3.12 Circular sector intersections from (a) bad or (b) good distributions of satellites 119
3.13 A graphical representation of the problem statement. Example of subareas $S(i + (j-1)r/n, jr/n)$, with j=1,...,n, using the described simplified approach. 121
3.14 Flowchart of GANP algorithm. 124
3.15 Overall logic that govern the behaviour of the drone during its mission. 126
3.16 Deployment manoeuvres followed in DS and PS: (a) Deployment path generation, each anchor has its relative intersections point. (b) Deployment path generation, from first intersection point, all anchors in list are deployed. 127
3.17 (a) PDoP level curves computed using $\mathcal{D}_k(s_k)$, where s_k covers the entire map; (b) PDoP level curves computed using $\mathcal{D}_k(s_k)$ for the straightforward algorithm sketched at the beginning of Section 3.2.2. 133
3.18 PDoP evolution along the simulations in Figure 3.17-(a) (GANP) and Figure 3.17-(b) (trivial), respectively. 134

3.19 Monte Carlo trials for the placement problem. When the placement error δ_i is treated as a random variable, a bias of about 15 cm is induced (dashed line), while if it is treated as an unknown but constant quantity estimated through (3.17) (solid line), the estimator is practically unbiased (bias around 1 mm). 134
3.20 (a) Characterisation of the ranging measurements $\bar{\rho}_{i,k}$ by means of an histogram obtained with 3000 consecutive measurements (b) Histogram of positioning error with 30000 consecutive measurements 135
3.21 (a) Experimental results for the bias δ_5 compensation; (b) Comparison between the LM and the LS solution to (3.17) with respect to the initial deployment error. 136
3.22 Flowchart of the cooperative positioning algorithm. 143
3.23 Dynamic example with a ground entity following an 8-shape trajectory, while the surrounding $q = 6$ UAVs move along straight trajectories and denoted with different colors (the black trajectories denote the actual positions in time). . 146
3.24 Distribution of the estimation error in the positions of a moving ground entity, moving according to Figure 3.23, along the X_w (a) and Y_w (b) axes over 5000 repeated measurements. 146
3.25 The UAV prototype 147

List of Tables

2.1 Possible classification of risk level for COVID contamination at workplace. 33
2.2 Monte Carlo analysis: Theoretical performance of the proposed system against 5 values σ_ρ. All the quantities are expressed in mm 48
2.3 Comparison between the true nodes' position N and estimated one $\hat{P}$. All the quantities are expressed in mm. . . . 52
2.4 DW1000 supported UWB channels. 57
2.5 CIR characteristics with varying PRF. 58
2.6 DWM1001 configuration parameters: standard SFD and PHY header mode are used, SFD timeout is set to 129, transmitted power gain is set to 19 dB. 59
2.7 Tested conditions. 59
2.8 Experimental standard uncertainty $\overline{\sigma}_\lambda(t_i, t_m)$ collected from the positions reported in Figure 2.28. All the quantities are expressed in millimetres and should be compared with the model-based value of the standard uncertainty $\sigma_\lambda(t_i, t_m)$. Results are the same for all the testing positions P_1, P_2, ..., P_9 in Figure 2.28. 86
2.9 Comparison between the theoretical nonlinear value (2.48) and the CRLB. All the quantities are expressed in mm^2. . . 87
2.10 Mean error of the UWB position estimates on 5000 position cycles for a linearly moving tag with respect to the three ground truth references. All the quantities are reported in millimetres. 89

2.11 Mean error $\{\mu_x, \mu_y\}$ and standard deviation $\{\sigma_x, \sigma_y\}$ along the X and Y axis, respectively, and computed in the five locations of Figure 2.33. All the quantities are expressed in millimetres. 92
2.12 Mean error $\{\mu_x, \mu_y\}$ and standard deviation $\{\sigma_x, \sigma_y\}$ for the dynamic tests of Figure 2.34. All the quantities are expressed in millimetres. 93
2.13 Mean error $\{\mu_x, \mu_y\}$ and standard deviation $\{\sigma_x, \sigma_y\}$ along the X and Y axis, respectively, and computed in P_5 of Figure 2.36. All the quantities are expressed in millimetres. . . 95

3.1 Value of bias β_i and σ_i for the UWB anchors. The size of the batch for each anchor in each position is of 2000 samples. . 112
3.2 Performance of the GANP algorithm versus parameter choices. 132
3.3 Optimal choices of the parameters. 132
3.4 Characterisation of bias and standard deviation of the ranging measurements 135
3.5 Monte Carlo simulations results. Both the first (uncertainties in the positioning of the infrastructure) and the second (uncertainties on the ranging measurements) set of simulations are reported. All the quantities are reported in millimetres. 145

Preface

The advent of the global navigation satellite system (GNSS) has ushered in a plethora of new deployment opportunities. This technology revolutionizes navigation and environmental awareness by providing precise positioning data for objects, individuals, and robots, even down to a few meters. Consequently, it has spurred the development of various downstream services, particularly in logistics, consumer applications, and robotics.

While GNSS excels in outdoor environments, where unobstructed communication with satellites enables accurate positioning, its limitations become apparent indoors. This underscores the necessity for indoor localization systems, which can extend outdoor applications to indoor settings and facilitate the creation of new applications.

This doctoral thesis tackles the challenges specific to indoor environments and puts forth practical and theoretical solutions aimed at expanding and enhancing the implementation of positioning systems within indoor spaces. It offers solutions tailored for both human-centric and robotic applications, thereby addressing a wide range of needs and scenarios. Addressing these challenges entails several aspects, such as designing wearable devices with integrated sensors to improve navigation and localization accuracy. Additionally, specialized algorithms are necessary to handle the localization of multiple receivers, with scalability being a significant concern for indoor positioning systems. Unlike GNSS, indoor systems demand precise scheduling to prevent message conflicts during position calculations, leading to inevitable delays that scale with the number of receivers involved. Furthermore, the need for temporary and self-deployable infrastructure to facilitate navigation for both humans and robots within unstructured

environments is increasingly apparent in this field, a challenge that this thesis aims to address. Furthermore, there is a notable gap in research concerning relative positioning systems reliant solely on ranging information, presenting promising avenues for exploration in both human and robotics applications. Another captivating area of study revolves around device-free localization, which facilitates the tracking of moving entities devoid of electronic devices. This thesis tackle these challenges and make significant contributions to the growth of indoor positioning systems and their applications.

The organization of this thesis is as follows:

Chapter 1 offers a concise overview of current indoor positioning technologies, outlining the challenges associated with indoor positioning systems and methods for evaluating their performance. Additionally, an introduction to ultrawide-band technology, which is utilized in this thesis, is provided. This section discusses the advantages and disadvantages of this technology, as well as the fundamental mechanisms for leveraging it in the field of localization.

Chapter 2, focus on positioning systems tailored for human applications, examining and suggesting solutions for the aforementioned issue. In particular, in *Section* 2.1 a customized anonymous tracking device designed for workers and operators of manufacturing companies and logistic providers. The device exploits a mesh UWB/BLE approach to extend the device's battery life without the need for a big battery. The system is able to dynamically discover new workers/tags within the monitoring area without time synchronization. The tracking device also integrates an inertial and a magnetometer module for gathering more insightful information regarding the tracked worker, such as moving directions and orientation. Thanks to the data provided by the tracking device, adequate data analytics can be done to measure the interaction between workers automatically in the different monitored factory areas. These algorithms are designed to provide each operator a detailed assessment of her/his personal behavior during the working shift and a risk index of the monitored processes or plant areas to their responsible/leader. The results can be used to proceed with a

spatial re-layout of the workplace, e.g., face-to-back or side-to-side layout workstations [1], and/or temporal rescheduling the activities to reduce the risk of Covid-19 contagion and diffusion at the workplace and targeted cleaning activities based on busiest areas. The main contribution of this sections is two-fold:

- The development and characterization of a custom wearable sensor able to provide localization information along with orientation and direction
- The development of an anonymous contact tracing framework to reduce contagion and improve the implementation of social distancing measures.

Regarding the relative localisation system *Section* 2.2 aims at providing a preliminary study to build a lightweight systems, dubbed Where Are You (WAY), that is able to generate a common map for every agent belonging to the WSN and removing the ambiguities given only pairwise distances. We identify the minimal set of information needed to solve the problem and we additionally provide an uncertainty analysis, investigating via Monte Carlo simulations how the ranging uncertainties impact on the overall final estimates. Finally, we propose a compact device prototype, based on ultrawide-band technology, used for the experiments and to practically show the technical viability of the solution.

To face with the device-free positioning system *Section* 2.3 presents the preliminary evaluation of a radar-like localization system based on commercial-off-the-shelf components. Our work aims to assess the feasibility of realizing an UWB-based radar exploiting the capability to estimate the CIR of cost-effective DecaWave's DWM1001 UWB transceiver. The validation was done by implementing a simple mono-dimensional tracker exploiting just two DWM1001 UWB transceivers. The relationship between target speed, baseline, and sampling frequency of the system was assessed in different scenarios demonstrating that an inexpensive UWB-based radar solution is feasible.

Section 2.4 extends the preliminary evaluation done in 2.3 of an ultrawideband bistatic radar in the following ways:

- We introduce a cost function to improve the estimates;
- We realised a distributed system to detect and track moving entities in the surrounding environment;
- We developed an IoT architecture to handle and sort the data using as much as possible the available bandwidth of the chosen UWB module;
- We enhance the processing update rate of the receiver, improving the maximum target velocity that the proposed system can track.

Furthermore, *Section* 2.4 provides a comparison with the latest generation of UWB modules.

Finally, to solve the problem of scalability on the indoor positioning systems, *Section* 2.5 presents innovative DTDoA ranging techniques solving both accuracy and scalability problems of the current state of the art. Results highlight how the systems can theoretically scale to infinity (i.e., any number of assets can be tracked), improving the measurement accuracy with an error in the range of 20 cm, at worst. The evaluation is carried out in a structured indoor environment encompassing 8 Qualisys Arqus A9 high-performance cameras[1] providing a position estimation with a much higher accuracy with respect to the UWB infrastructure (down to 0.03 mm). By using the MoCap estimated trajectory as a reference, we validated the UWB one. Results highlights that the effect of the tag motion for the typical human being speed, is negligible.

It's worth noting that due to the research conducted in this thesis, *Section* 2.6 presents a project that emerged as the recipient of the prestigious *10th Fondazione VRT Mountain Innovators Grant*. This project delves into the examination of how positioning systems can offer a solution to a pertinent issue in my hometown of Trento — the dynamic between humans and wildlife in the surrounding forests.

[1] https://cdn-content.qualisys.com/2020/06/PI_Arqus.pdf

Chapter 3 discusses the integration of positioning systems into the robotics domain, drawing insights from developments in human-centric positioning. It presents solutions across various domains, spanning from human tracking to applications in space exploration.

In particular *Section* 3.1 presents the preliminary results of a human-robot interaction use case in which an autonomous UAV is in charge of following a human subject exploiting only UWB-based positioning. The paradigm chosen for the UAV control is known as *Leader-Follower* and consists of an autonomous UAV follower that plans its action from the action of a human leader. This paradigm applies to different type of mobile robots and it is based on the computation of a reference point placed in the neighbours of the human being and used for scheduling its motion [2]. In the proposed application, the human being is equipped with a single UWB transceiver (referred to as the *target* or *tag*), while the follower is a compact 250 mm wheelbase UAV equipped with 3 UWB transceivers (called *anchors*) deployed in a triangular shape to avoid positioning ambiguities [3]. The main contributions of this section are:

- An analysis of the impact of the geometric shape and baseline of the 3 UWB anchors mounted on the follower on the accuracy of the position estimates;
- The development of an algorithm that given the position estimates, track the tag with desired precision;
- The development of Hardware-in-the-Loop simulations for the algorithm evaluation and the integration of the proposed solution on a commercial compact 250 mm UAV with preliminary experimental results.

When an absolute reference frame is required for the positioning phase, it is common to see a network of reference nodes deployed by the human being.

From this perspective a self-deployable network is preferable, and under this perspective *Section* 3.2 propose a solution that overcome infrastructure

setup inaccuracies and provide a positioning system also for unstructured environments, where off-line analysis is inapplicable, we developed a method for dynamic placement and runtime extension of the infrastructure anchors. In the discussed solution, while exploring the environment, the mobile robot deploys new anchors to strengthen the infrastructures. Thus the ranging sensors are self-deployable and will extend the positioning reference at runtime during the robot exploration. Notice that this marks a striking difference with respect to the known literature. Indeed, existing solutions, e.g., [4, 5], cannot change the nodes infrastructure at runtime based on robot needs nor can adequately leverage the ratio of information versus uncertainty that a new added anchor injects in the multilateration problem. Moreover, our solution is robot-centered: existing solutions usually try to optimize the entire region as a whole, with evident computational burden issues and difficulties in unknown or partially known environments, while our solution is extremely light in terms of computing power and can be computed onboard the vehicle while it explores the (possibly unknown) environments. In particular, our solution proposes an online-incremental algorithm based on a genetic approach to solve the constrained optimization problem, which finds the most convenient placement for new anchors and reduces the number of deployments. The algorithm keeps the maximum target uncertainty below the user requirement, which is based on the Geometric Dilution of Precision (GDoP). It has to be noted that the proposed solution works with any metric able to express the positioning uncertainty, but the GDoP comes handy for this purpose [6].

Finally *Section* 3.3 makes significant contributions to the progress in the complex field of exploration, with special reference to planetary exploration, including: i) the design of a distributed algorithm for Unmanned Aerial Vehicles (UAVs) cooperative localisation; ii) the definition of a positioning framework for multiple robots with unlimited scalability; iii) the analysis of the uncertainties involved in the process and their experimental validation.

Chapter 1

Unveiling the World of Indoor Positioning Systems: An Introductory Exploration

Positioning, encompassing the determination of locations for entities such as humans, equipment, and robots, has emerged as an active and dynamic research domain. Positioning systems are categorised into outdoor and indoor types, depending on the specific environment in which a positioning problem occurs. Outdoor positioning unfolds in open spaces, whereas indoor positioning is restricted to interior spaces such as homes, healthcare facilities, and shopping malls, introducing distinct challenges and considerations.

Indoor positioning systems continuously and in real-time determine the position of an object within a physical space, as illustrated in Figure 1.1. IPSs employ a variety of positioning approaches, exhibiting differences in accuracy, cost, precision, technology, scalability, robustness, and security [7, 8]. The escalating demand for precise indoor positioning has transformed it into an active research area, yielding diverse proposed solutions [9].

Indoor positioning presents specific demands that make it radically different from outdoor positioning. The evaluation of indoor positioning systems revolves around four pivotal quality metrics, as outlined in [10]:

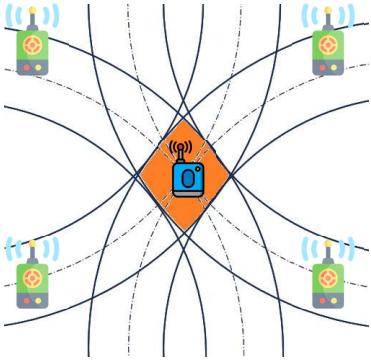

FIGURE 1.1: Multilateration: positioning using four reference point.

- System accuracy and precision;
- Coverage and resolution;
- Latency in updating positions;
- Susceptibility to signal interference (e.g. reflections).

Indoor positioning finds numerous applications, such as the development of indoor navigation systems for individuals with visual impairments, locating devices within buildings, assisting tourists in museums, guiding individuals to emergency exits, tracking children in crowded areas, and facilitating robotics in navigating shared environments with humans. The diverse range of indoor positioning applications requires careful consideration of various quality attributes, prompting the meticulous selection of IPSs tailored to meet the specific requirements of each application. Developers of indoor positioning systems must struggle with two fundamental questions: (1) *which technologies are suitable for implementing the desired IPS?* and (2) *how can we achieve an optimal equilibrium among various quality metrics to establish an efficient IPS?*

Accuracy and precision in position measurement stands as a crucial prerequisite for indoor positioning techniques. With ultra-wide band (UWB) emerging as a pivotal technology demonstrating effectiveness in indoor

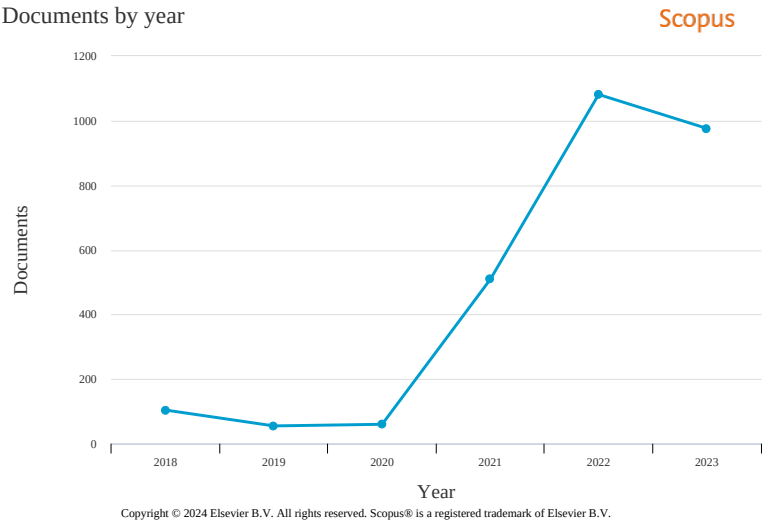

FIGURE 1.2: Number of scientific documents in the five-year period 2018 – 2023.

positioning, coupled with the authorization by the Federal Communications Commission (FCC) for unlicensed UWB communications, there has been an intensive exploration and study of civilian applications employing UWB.

Hence, the active pursuit of developing novel algorithms to enhance UWB positioning performance and the exploration of new applications are evident in current research trends, as indicated by the Scopus database query (refer to Figure 1.2). There has been a significant surge in activity, particularly in 2020, likely attributed to the recent pandemic crisis, which has underscored the importance of indoor positioning systems utilizing UWB technology as a key solution for monitoring interpersonal distances in confined spaces.

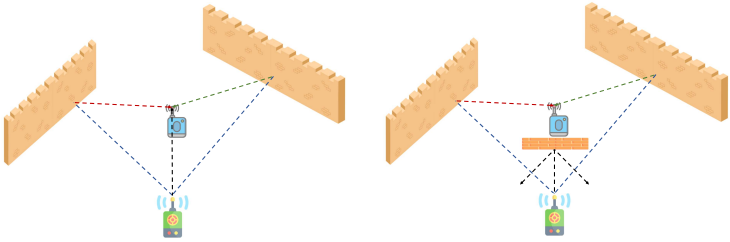

(a) (b)

FIGURE 1.3: In (a) LoS condition, in (b) NLoS condition.

1.1 Challenges of Indoor Positioning Systems

Indoor positioning differs significantly from outdoor positioning, as outlined in prior research [11]. The intricate nature of indoor environments arises from the presence of numerous elements, posing challenges such as signal reflection that give rise to multipath and delay issues. Moreover, indoor settings frequently feature non-line-of-sight (NLoS) propagation, hindering signals from traveling directly in a straight path from an emitter to a receiver. This characteristic introduces irregular time delays at the receiver, as depicted in Figure 1.3. Furthermore, the existence of objects contributes to substantial signal attenuation and scattering. Indoor positioning encounters issues associated with signal stability, as the signal strength is susceptible to frequent fluctuations due to the presence of numerous radio-frequency interference sources in the surrounding environment, including mobile devices, Bluetooth devices, Zigbee devices, and other wireless devices [12].

1.2 Indoor Positioning: Systems Performance Metrics

IPSs utilize various positioning methodologies that exhibit significant variations in terms of cost, accuracy, precision, technology, scalability, robustness, and security [7, 11, 13]. Certain applications may demand cost-effective IPS solutions, while others necessitate high-precision IPS, as seen in medical

tracking or industrial environmental monitoring. In the subsequent section, we will delineate the principal features of IPSs.

- Accuracy: The concept of accuracy, refers to *"the closeness of agreement between a measured quantity value and a true quantity value of a measure"* [11]. Within the realm of an indoor positioning system, accuracy is defined by the average Euclidean distance between the estimated and true positions [13]. While IPS accuracy holds paramount importance across various applications, there are situations where trade-offs between accuracy and other performance metrics must be contemplated [11, 13];

- Availability: This denotes the percentage of time during which the positioning service is operational, taking into account the required level of accuracy. Typically, availability is categorised into three tiers: 1) low availability if $\leq 95\%$, 2) standard availability if between 95% and 99%, 3) high availability if $\geq 99\%$ [14];

- Coverage area: In the context of indoor positioning systems, coverage is classified into two levels: local and scalable. Local coverage relates to a well-defined but limited area, such as a building, where the coverage size is specified. On the other hand, scalable coverage denotes a system's capability to expand the area by deploying additional sensors [11];

- Scalability: Denotes the system's capability to ensure its standard positioning function while expanding in either of two dimensions: area and the number of users. Scalability concerning the number of users indicates a rise in the number of units located per time period within a specified area.

- Cost: The cost of an IPS is evaluated in terms of money, time, space, and energy across various system levels, including installation, maintenance, infrastructure components, and positioning devices [8, 13]. Installation and maintenance costs encompass initial setup and ongoing expenses, while infrastructure and device costs include acquisition of required hardware, configuration, and energy

usage.Moreover, efficient energy management is crucial in IPSs to ensure service continuity and support enhanced mobility solutions.

- Privacy: Strengthening user privacy necessitates the implementation and maintenance of security measures to protect data from unauthorized access, theft, and misuse.

1.3 Indoor Positioning: Systems Technologies

Indoor positioning technologies are structured into two main categories:

- Building-Dependent Technologies: These technologies hinge on the specific building in which they operate, leveraging either existing technologies or the building's map and structure. The suite of technologies employing the building's infrastructure includes 1) WIFI, 2) cellular based; and 3) Bluetooth. Further segmentation within this category are Technologies Requiring Dedicated Infrastructure such as 1) radio frequency (RFID or UWB), 2) infrared, 3) ultrasonic, 4) Zigbee, and 5) laser.
- Building-Independent Technologies: This classification encompasses technologies that do not depend on specific hardware within a building. Examples include dead reckoning, where an object establishes its current position based on past position, speed, and direction, and image-based technologies utilizing cameras.

It is important to note that image-based technologies may be categorised as building-dependent if they depend on special signs or a map within the building. In contrast, building-independent technologies do not require such information. Figure 1.4 provides a comprehensive overview of the classification based on the infrastructure of the system implementing these technologies. A brief introduction regarding each technology can be found in the subsequent subsections.

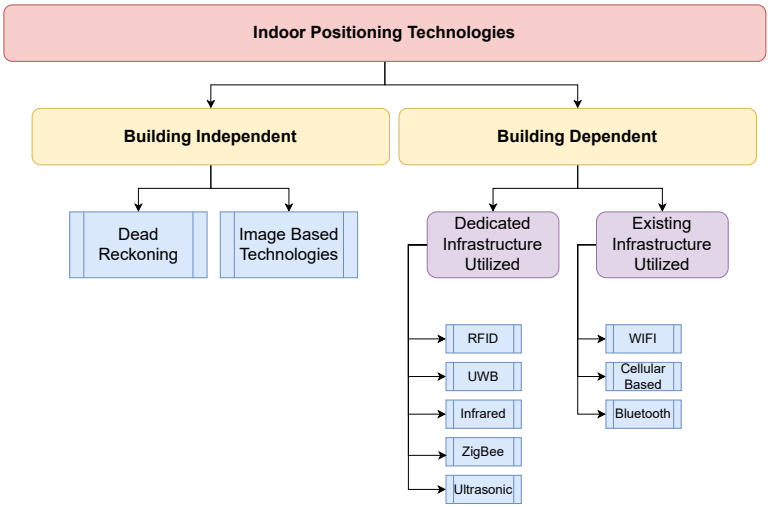

FIGURE 1.4: Categorazation for IPS.

1.3.1 Radio Frequency Identification

Radio Frequency Identification (RFID) employs radio waves for wireless transmission of an entity's identity. Mainly employed for automated identification within expansive systems, RFID operates through the exchange of radio signals at various frequencies between readers and tags. While various positioning methods can be employed with RFID, proximity sensing is the most common, known as Cell of Origin, detecting the presence of RFID tags rather than their exact position by using techniques based on received signal strength indicators [11, 13, 15].

1.3.2 Infrared

Infrared (IR) wireless communication utilizes the non-visible spectrum of light near the red edge of the visible spectrum. Infrared technology can be deployed in two distinct manners: a) *direct* IR and b) *diffuse* IR. Direct IR is illustrated by the Infrared Data Association (IrDA), which is a point-to-point ad-hoc data transmission standard specifically designed for very

low-power communications and short distances, supporting data rate up to 16 Mbps. On the flip side, diffuse IR generates more robust signals compared to direct IR, facilitating an extended communication distance, typically ranging from 9 meters to 12 meters. Diffuse IR allows point-to-multipoint communication (P2MP) without requiring a LoS condition [15] by using wide-angle LEDs. Positioning methods are commonly associated with IR technology are proximity, differential phase-shift, and angle of arrival (AoA) [16–18].

1.3.3 Ultrasonic

Sound represents a mechanical wave distinguished by pressure oscillations transmitted through a medium, commonly air in the context of positioning systems. Determining the distance between nodes deployed in the environment entails measuring the time it takes for ultrasound pulses to travel from an emitter to a receiver. Architectures employing this approach are referred to as active device systems and commonly utilize a multilateration approach. This approach relies on three or more ranges to fixed receivers at known locations, enabling the estimation of the emitter's coordinates. Conversely, an alternative architecture utilizes a backward signal direction, deploying multiple static emitters at known locations and one or more passive receivers to capture the signal, thereby enhancing flexibility and adaptability.

1.3.4 Zigbee

ZigBee is a wireless technology standard classified as a low-rate Wireless Personal Area Network (WPAN), specifically designed for applications that demand low power consumption and low data throughput [11]. In free space and LoS conditions, a ZigBee node can achieve a communication range of up to 100 meters. However, in indoor environments, this range typically falls within 20 to 30 meters. A ZigBee node is characterized by low complexity and cost, incorporating a microcontroller and a multichannel two-way radio [19]. Positioning functionalities are reached through coordination and communication with neighboring nodes. Typically, Received

Signal Strength Indication (RSSI) values are employed to estimate the distance between nodes [11].An alternative method, proposed for determining the distance between nodes in the ZigBee network [20, 21], utilizes the phase shift of the reflected signal from the target node. This shift is a result of the time delay between the target and transmitter.

1.3.5 Ultrawide-Band

Ultra-Wideband stands out as a radio technology tailored for short-range, high-bandwidth communication, featuring robust multipath resistance and a certain level of penetrability through building materials. These characteristics make UWB particularly well-suited for activities such as indoor distance estimation, localisation, and tracking. A standard UWB setup comprises a radio wave generator and receivers for capturing both propagated and scattered waves. A radio wave qualifies as UWB if its bandwidth is ($\geq$ 500 MHz) or constitutes 20% of the carrier frequency. To mitigate interference with other radio services, the Federal Communications Commission (FCC) in the USA has imposed restrictions on the unlicensed use of UWB. This includes maintaining an equivalent isotropically radiated power density of -41.3 dBm/MHz and confining the frequency band to 3.1 GHz - 10.6 GHz, or 6.0 GHz - 8.5 GHz as per the European Communications Committee (ECC) guidelines.

1.3.6 WLAN/WiFi

Indoor positioning systems utilizing WiFi technology depend on acquiring information about the accessible wireless routers within the operational area of the system. The most common approach for WLAN positioning is founded on RSSI, easily obtainable in 802.11 networks and compatible with off-the-shelf WLAN hardware [11]. Less frequently utilized methods over this technology include Time of Arrival (ToA), Time Difference of Arrival (TDoA), and Angle of Arrival (AoA), primarily due to challenges associated with angular measurements and the complexity of time delays. Positioning systems usually attain accuracy levels within the range of 3 to 30 meters, as indicated by [13].

1.3.7 Cellular Based

The Global System for Mobile Communications (GSM) network offers global accessibility in most countries, surpassing WLAN coverage, albeit with reduced positioning accuracy. GSM operates in licensed bands, minimizing interference from devices using similar frequencies, unlike WLAN [11]. Indoor positioning becomes viable on a mobile cellular network when a building is covered by one or more base stations with strong RSSI [13]. As documented in the literature, 5G has bring a plethora of technologies, encompassing large-scale antenna arrays, ultradense networking, novel multi-access schemes, full-spectrum access, and a new network architecture built upon software-defined networks (SDNs). These advancements enable the development of cellular based positioning algorithms, which are typically classified into two primary categories: geometry-based methods and feature matching-based methods [11, 22].

1.3.8 Bluetooth

Bluetooth serves as a standard for wireless personal area networks (WPANs) [11]. Designed as a very low-power technology for peer-to-peer communications, Bluetooth operates within the 2.4 GHz ISM band. Compared to WLAN, Bluetooth exhibits a lower bit rate and a shorter range, typically ranging from approximately 10 cm to 10 m [13, 19]. Proximity and RSSI methods are commonly employed in Bluetooth technology for position estimation [19].

1.3.9 Dead Reckoning

Dead reckoning involves estimating a position based on previously determined positions and known or estimated speeds over elapsed time, primarily utilizing an inertial navigation system as the main sensor. However, a drawback of dead reckoning lies in its cumulative inaccuracy, leading to deviation in the position that increase with time. By incorporating a sufficient number of absolute position updates, dead reckoning aims to restrict the linear growth of position errors within predetermined bounds [23].

To enhance accuracy and minimize errors, dead reckoning must employ additional methods to adjust the object's position after each interval [24].

1.3.10 Image-based

Indoor positioning technologies based on images encompass camera and computer vision-based technologies [11, 25]. Various types of cameras, spanning from smartphone cameras and 3D cameras to 360-degree cameras, can be utilized; however, their performance varies based on the information obtainable from their images [26]. Image-based positioning systems can be divided into: a) *egomotion systems*, utilizing the motion of a camera in relation to a fixed scene to estimate its present position, and b) *static sensor systems*, which detect mobile entities within the images.

1.4 Ultrawide-Band Indoor Positioning Systems

UWB emerges as an accurate, precise, and promising technology for real-time inventory indoor tracking, localisation systems for emergency services, and indoor navigation [27, 28]. It spreads radio energy across a wide frequency band with low power spectral density, ensuring high data throughput and effective signal penetration through obstacles such as walls and objects [27]. The main application areas for UWB encompass 1) communication, 2) localisation, 3) radar [27, 29].

UWB stands out among other technologies due to its distinctive features [13, 27, 30]. It boasts a high data rate, reaching up to 100 Mbps, making it a favorable choice for near-field data transmission. Additionally, its high bandwidth and short pulses contribute to mitigate the multipath problem. This characteristic permits to accurately determining the reception time of messages between transmitter and corresponding receiver, making this technology the preferred option for indoor positioning in comparison to alternative technologies [19, 28, 31].

The UWB period pulse signals define the maximum observable multipath delay, allowing for unambiguous resolution of multipath, while the duration of UWB pulses determines the resolution on the path delay.

Unlike positioning technologies such as infrared and ultrasound sensors, UWB technology does not need line-of-sight, thanks to the ability of its low-frequency components to penetrate building materials. This feature is advantageous for indoor positioning, allowing ranging under non-line-of-sight conditions. Moreover, UWB remains unaffected by the presence of other communication devices or external noise due to its high bandwidth and signal modulation capabilities [32, 33]. Furthermore, UWB equipment is cost-effective and consumes less power than alternative solutions.

Due to these characteristics, UWB has garnered attention not only from the scientific community but also from businesses, as evidenced by the TechNavio report forecasting a growth from 21.8 billion dollars in 2022 to 182.2 billion dollars by 2030. This reflects a compound annual growth rate of 30.4%[1].

1.4.1 Basic Measuring Principles

UWB positioning systems rely on various estimation algorithms to determine the location of objects. These algorithms are classified into three main categories: 1) Time of Arrival (ToA), 2) Angle of Arrival (AoA), and 3) Time Difference of Arrival (TDoA). Each of these techniques utilizes different principles to calculate position information based on the timing or angles of radio signals transmitted between reference nodes and the target device.

ToA algorithms measure the time taken for a signal to travel from the transmitter to the receiver, providing information on the distance between them. AoA algorithms, on the other hand, determine the direction from which the signal arrives at the receiver, typically by analyzing the phase differences between signals received by multiple antennas. TDoA algorithms calculate position based on the differences in arrival times of signals at different reference nodes, leveraging the known locations of these nodes to triangulate the position of the target device.

[1]https://www.researchandmarkets.com/report/ipin#tag-pos-8

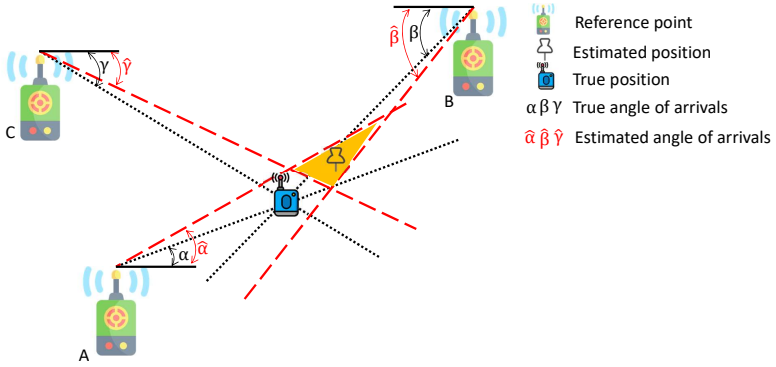

FIGURE 1.5: Angle of arrival principles.

Each of these algorithms has its strengths and weaknesses, and the choice of which to use depends on factors such as accuracy requirements, environmental conditions, and hardware constraints. In the upcoming sections, a concise overview of each of these algorithms is provided.

Angle of Arrivals approach

Calculating the AoA involves determining the direction of a radio-frequency wave by comparing either the signal amplitude or carrier phase across an antenna array. This process includes measuring the TDoA between elements of the antenna array and considering the antenna's geometrical properties. The positioning feature is obtained by the intersection of the angle lines corresponding to each signal source, as illustrated in the Figure 1.5. AOA estimation algorithms exhibit higher complexity compared to other methods and are highly sensitive to various factors, potentially leading to errors in the estimation of the target position.

Time of Arrival approach

The Time of Arrival principle revolves around measuring the signal travel time from a transmitter to a receiver. This measurement allows us to derive the Euclidean distance between two devices by multiplying the travel time

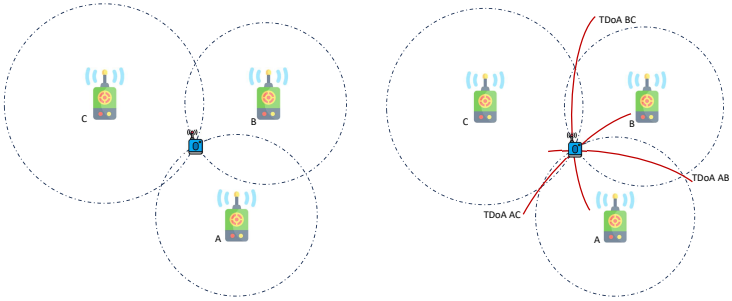

FIGURE 1.6: In (a) Time of arrivals principles; in (b) Time of difference arrivals principles.

by the wave speed across the medium (e.g., speed of light in a vacuum). The drawback of this approach is its dependence on precise synchronisation among the devices' clocks. Even a one-nanosecond error in synchronisation can result in a distance estimation error of 30 centimeters. To address the challenge of tight time synchronisation, Round-Trip-Time (RTT), also known as Two-Way Ranging (TWR), is employed. This involves measuring the time taken by the signal to travel from a transmitter to a receiver and back. However, this method necessitates sequential message transmission, which may introduce significant latencies. The Time of Arrival or Round-Trip-Time approaches for positioning functionality typically involve the geometric intersection of circles originating from multiple transmitters, as illustrated in Figure 1.6-(a).

Time Difference of Arrival approach

The Time Difference of Arrival (TDOA) method relies on measuring the time difference between when a signal is transmitted by an object and its reception by three or more receivers, as depicted in Figure 1.6-(b). Unlike the Time of Arrival approach, the receiver doesn't need to know the absolute transmission time; only the time difference of arrival from synchronised receivers is required. In 3D space, the coordinated of an emitter can be determined from four synchronised receivers by the intersection of three

hyperboloids. However, the precise synchronisation of all receivers remains a prerequisite for this approach.

Given the requirements of indoor environments, which demand technology capable of achieving accuracy, precision, and robustness against multi-path phenomena, as well as seamless integration into various applications with different communication schemes, UWB technology emerges as the most promising solution. In this thesis, we address positioning systems for both humans and robots, necessitating flexibility, compactness, and adaptability in the implementation of positioning solutions. Leveraging commercial UWB modules, this thesis explores the diverse applications of this technology, demonstrating its potential as a viable and assistive solution.

Chapter 2

Human-Centric Positioning Systems: Enhancing Spatial Awareness and Navigation

In light of what we have seen so far, Ultra-Wideband technology emerges as a compelling solution for calculating distances among individuals. This innovative approach presents a promising avenue for addressing the spread of the Covid-19 virus during the pandemic, which has instigated significant changes in various aspects of billions of people's lives worldwide. One of the most relevant changes was the temporary interruption of the production activities of many manufacturing companies. At the same time, however, most of the logistic providers could not reduce their operations. Instead, during the 2020 lockdown, they faced a remarkable increase in the required delivery orders, particularly by private citizens forced to stay at home. However, both these scenarios are distinguished by the same criticalities determined by the necessity to fully operate after the first wave of Covid-19 diffusion coping with the eventual virus presence at the workplace. This particular circumstance generates on the manufacturing and logistics companies' non-decreasing productivity while guaranteeing workers' safety and health.

Unfortunately, guidelines widely promoted to prevent Covid-19 contagion at the workplace were not enough if left alone [34]. In fact, during the

first wave of Covid-19 from March to May 2020, more than 50'000 Italian workers get infected at the workplace, while a German area of 500'000 population experienced a second lockdown due to a new hotbed of coronavirus originated in a slaughter industrial plant. Similar mass contaminations inside a factory were also experienced even in the UK and USA [35]. It is clear that further organizational and technological measures are fundamental and largely asked to be developed to ensure employees' safety and protect their health during the necessary working activities [36, 37].

Proper technologies could be of substantial help to reach such a fundamental goal [38]. In particular, Internet of Things (IoT) solutions combined with Indoor Localization Systems (ILS) could offer relevant and remarkable opportunities. ILS or Real-Time Location Services (RTLS) are known to be a set of hardware/software architectures developed to provide the location of a tagged entity in a specific time frame, usually within a building or other contained area [39]. These technologies are typically leveraged to trace the evolution of tagged entities' positions over time, thus evaluating their spatial movement inside a monitored area or facility [40]. In the literature we can already find several implemented architectures, exploiting different communication technologies; including, Bluetooth [41], ZigBee [42], ultrasound [43], vision [44], infrared [45], Wi-Fi [46], RFID [47], and more recently ultra-wide-band (UWB) [48].

RTLS is an emerging technology for manufacturing and logistic companies that recently began to adopt it for multiple purposes [49]. For example, RTLS is used to monitor the actual travel paths of human-driven forklifts between the isles of warehouses [50], to identify the current location of missing parts or components of manufacturing processes, and to ensure the operator safety avoiding their entrance in dangerous areas of industrial plants [51]. UWB is considered one of the most promising technologies for high-precision ILS due to a number of desirable advantages like low-power capabilities, centimeter-level resolution, robustness to multi-path effect, and a certain degree of obstacle penetration capability [52].

In their pioneering work, Cheng et al. [53] proposed the utilization of RFID-Based Real-Time Location Systems (RTLS) technologies to mitigate

the risk of epidemic outbreaks, specifically addressing the SARS pandemic within a Hong Kong hospital setting. A parallel approach has been recently introduced by Ho et al. [54], who applied a similar strategy to avert potential patient-to-medical-staff contagion, thereby safeguarding the well-being of hospital employees during the Covid-19 outbreak in Singapore.

Contrary to these efforts, various solutions, such as smartphone applications like Tabaud, Aarogya Setu App, TraceTogether, COVID Safe, Immuni, and COVID Watch [55], rely on Bluetooth beaconing or GPS positioning, rendering them unsuitable for achieving precise indoor localization. Addressing the inherent accuracy limitations associated with Bluetooth and RFID technologies, Istomin et al. [56] proposed the use of Ultra-Wideband technology to develop a robust contact tracing system. Their work introduces a comprehensive hardware/software architecture based on a UWB Indoor Localization System (ILS), aimed at preventing COVID-19 contagion in industrial environments through anonymous contact tracing.

Among the solutions outlined above, the most promising one involves harnessing UWB technology. This approach leverages a predeployed network of UWB nodes, referred to as anchors, serving as reference points for multilateration-based techniques. Although categorized as an absolute localization system, it is noteworthy that our focus may not necessarily be on determining the absolute positions of receivers. Instead, our emphasis may lies in establishing relative positions with respect to other nodes, essentially realizing a relative localization system. This entails the creation of a Wireless Sensor Network (WSN) among the mobile nodes, eliminating the necessity for a predeployed infrastructure.

WSN are becoming a reality in many application fields, manly due to the ever decreasing cost and reduced and effective power consumption. Low energy radio frequency modules for data transmission make WSN a viable solution for, e.g., health care [57], assisted living [58], fitness monitoring [59], building automation [60] and security [61] application scenarios.

WSNs have been widely applied to tracking and positioning systems. This is witnessed by the large literature solutions available in the field, where

the adopted technologies range from ultrasound [62] to visible light [63], WiFi [64] to ultrawide-band [65–69]. One emerging problem in this research area refers to *relative* localisation, that is localising the nodes of the network with respect to each other but without a fixed, external and global reference. In such a case, each node has to reconstruct the location of all the other nodes with respect to a local reference. Application scenarios where this is turning to be quite useful are coverage, deployment and routing, especially if they are carried out autonomously by either human beings or robots.

Given that one of the most effective measurements obtainable from WSN nodes is the relative distance between a pair of node, utilizing techniques such as time-of-flight [70] or RSSI [71], distance-based solutions are commonly applied to tackle the challenge of relative localization. These solutions employ diverse methodologies, including trilateration, multilateration, and multidimensional scaling (MDS) [72–74].

The MDS algorithm, in particular, represents dissimilarities within the data as distances in an $\mathcal{N}$-dimensional space, creating a map of the measurements. In the realm of robot localization, MDS finds extensive use in constructing relative maps of agents when the system lacks reliance on an external infrastructure [75]. Although MDS is a straightforward approach, it contends with geometric ambiguities, limiting the map estimation to isometric transformations, a common drawback shared by various relative localization algorithms.

The problem of relative localisation and tracking has been addressed extensively using the MDS algorithm for robotic applications in conjunction with known positions of some team members. For example, in [72, 76], the authors extend and generalise the MDS algorithm including the knowledge of some nodes positions. In [77, 78], the geometric ambiguities are mitigated by the knowledge of the node velocities, which are used to correlate the relative maps at two consecutive time instants. A similar problem is investigated in [79, 80] considering the additional complexity enforced by the partial connectivity between the nodes. In [81], the authors build a cooperative navigation for coordinated-team based on dead reckoning, ranging data and particle filters, while [82] uses inter-node range measurements and

odometry data to estimate the nodes positions. Wenchao et al. [83] address the ambiguity problem by letting one agent to move and using the displacement vector computed via inertial information to produce an analytical solution for the ideal noise-free case. All the presented literature entries are based on the (partial) knowledge of a subset of the node positions, thus automatically solving the roto-translation and flipping geometric ambiguities, or mitigating the inconsistencies induced by the MDS algorithm fusing additional available data, such as velocity and acceleration, to the ranging measurements. In situations where ranging measurements serve as the sole source of information, it becomes apparent that existing solutions may not be applicable. This characteristic not only streamlines the computational and communication aspects of the nodes but also results in inherent power savings for the nodes.

The prospect of a solution relying solely on ranging measurements opens up the possibility of its application to scenarios involving human subjects equipped with ranging sensors, navigating through either structured or unstructured environments. Examples include groups of individuals hiking in the mountains, families attending large public events, or patrons exploring a vast shopping mall. In all these instances, the knowledge of members' locations becomes a critical safety factor.

Up until now, the approaches we have discussed depend on the collaboration of individuals who are equipped with either active or passive electronic devices, seamlessly integrated into UWB networks. However, there specific application scenarios, such as surveillance or patient monitoring, where we can not - or do not want to - equip the entity to be tracked with an electronic device. In those scenarios, device-free approach is getting increasing attention as a solution that offer the flexibility of not equipping an entity with electronic, paying a small cost in term of accuracy.

As a direct result of the escalating interest in this domain and the substantial advancement of wireless technologies, there has been a surge in the development of innovative indoor positioning technologies and algorithms [84]. Notably, many of these technologies are categorized as *device-based*, indicating that the tracked agents need to be outfitted with active devices to

determine their spatial location.. This approach takes the name of Device-Based-Localization (active localization). While these solutions still cover a key role as positioning solutions [85], a significant amount of work has also been dedicated to the development of *Device-Free* (DF) methods [86]. DF positioning systems localize targets within an environment without the need for target-mounted sensors. This approach is particularly useful in all the scenarios where we can not – or do not want to – fit an active device on the entity we want to track and takes the name of Device-Free-Localization [87] (passive localization). Multiple applications in the literature exploit passive localization, intrusion detection, assisted living, customer and/or worker tracking, and smart-home monitoring.

Passive localization techniques have the potential to greatly increase in number in the coming years [88], as the advantages of not using a target-mounted device will outweigh the loss of precision of passive systems with respect to active solutions [66, 67, 89, 90]. Device-Free localization can be implemented in multiple ways and can mainly be divided into 3 big classes [91]: **1)** RF-Based; **2)** Light-based; **3)** Acoustic-Based. In the literature, we can find passive localization infrastructures that have been realized by using cameras [92] or by detecting changes in the infrared spectrum of the analyzed environment [93]; by tracking echos of ultrasonic signals in a sonar-like fashion [94, 95].

Apart from the prominent radar systems developed at the beginning of the 20th century, contemporary research interests in device-free localization, particularly in indoor and IoT applications, freshen by low-power radio systems and human-centric services. A comprehensive exploration of IoT localization methods is available in [96]. The Ultra-Wide-Band technology stands out among RF-based techniques due to its recognized robustness against multipath effects [97] and compatibility with various radio communication technologies.

An in-depth analysis of the UWB radio frequency spectrum, particularly addressing the Channel Impulse Response (CIR), enables the localization of moving objects within the propagation area. The CIR, representing signal power at different time delays, provides insights into the various

paths a signal takes from a transmitter to a receiver. UWB radar systems leverage this information to detect objects based on the trace identified in the measured CIR.

An interesting approach involves employing UWB sensors in a radar-like system inspired by the concept of *pulsed radar*, as elucidated in [68, 98]. In an RF-flooded environment, the movement of entities induces disturbances on the RF spectrum, allowing the detection of the target's location. This method, termed *multipath-assisted* localization, relies on detecting RF scattering sources using multipath components or the originally transmitted signal. To implement this technique, an analysis of the RF spectrum of the static environment is required to establish the background model. Upon the entry of a moving entity, the background and RF spectrum are compared to localize the entity by observing CIR time variations. Signal reflections, known as Multi-Path Components (MPC), are replicas of the original signal reaching the receiver side with an unavoidable delay. While MPCs are generally considered noise in localization, target-originated MPCs are pivotal in device-free systems, often termed *multipath-assisted* localization techniques. These solutions rely on evaluating the CIR, representing the RF channel's status through the magnitude and phase of the MPCs. Once the background contribution is computed, variations in the CIR can be correlated with the motion of entities in specific positions, enabling Device-Free Localization (DFL).

Until now, the indoor positioning approaches discussed share a common drawback: scalability. This aspect distinguishes positioning systems based on GNSS from indoor positioning systems utilizing the aforementioned technologies, as it pertains to the effective tracking capacity of nodes, or in other words the scalability of the system. This poses a big problem due to the necessity of scheduling all nodes in the network to prevent conflicts in transmitted messages. The requirement for scheduling translates into a maximum number of nodes that can be tracked before saturating the bandwidth of UWB networks. Furthermore, this imposes an update rate on localization that is contingent on the number of nodes involved in the network.

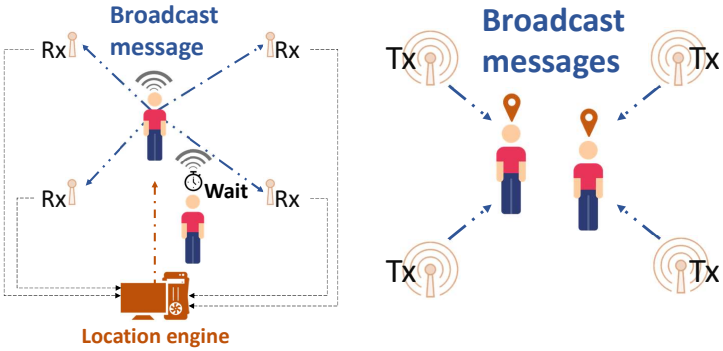

FIGURE 2.1: In (a) the traditional UTDoA approach where the tag emits the broadcast message, thus limiting the scalability of the system. In (b) the implemented DTDoA approach, where the anchors emit the messages used by the entity to localisation awareness.

In the case of RF-based localisation systems, the fundamentals ranging techniques to estimate the distance from two nodes are: *Received Signal Strength* (RSS); *Time of Arrival* (ToA); *Time Difference of Arrival* (TDoA) and *Angle of Arrival* (AoA). ToA and TDoA ranging techniques are the most commonly used. In ToA, two different communication schemes can be implemented: Single-side (SS) or double-side (DS) two-way ranging (TWR) [99]. With TWR, a synchronisation mechanism between nodes is not required. In fact, accurate calibration of the crystal oscillators is sufficient to achieve the desired accuracy, especially in SS-TWR. The maximum achievable measurements data rate [100] is one of the major drawbacks of TWR, and it depends on the number of messages that the tag has to exchange with the anchors. To overcome this issue, the TDoA approach has been proposed. In this case, a crystal oscillator trimming is not enough to achieve the desired accuracy because a tighter synchronisation between the nodes is required. As for the ToA approach, also for TDoA two possible schemes can be implemented. A centralised, or uplink, TDoA (UTDoA) and a decentralised, or downlink, TDoA (DTDoA). Figure 2.1 presents the DToA and UTDoA approaches. In the first approach, a tag emits a UWB signal, and the difference in the reception times at the anchors side is used to calculate the position of the

tag with respect to a reference point [101]. On the contrary, the second transmission scheme mimics a common GPS. The anchors – as the satellites – continuously broadcast timestamped messages that can be received by listening tags/robots. The Uplink Time Difference of Arrival (UTDoA) communication protocol assumes that position information is stored on the infrastructure side, which can be problematic in some applications, e.g., robotic swarm. Sharing position information among all robots can add unnecessary overhead to the estimation process, and installing a router to create a sink node may not always be feasible. The proposed solution is a distributed system where information resides directly on the tag, allowing each entity to choose the right update rate for its calculation without being affected by other tags accessing the information. Notice that the proposed approach generalises the UTDoA, since each entity can in case share the information with the infrastructure, thus resuming the UTDoA paradigm.

In [102, 103] authors developed a DTDoA system, where a tag can determine its position with respect to a reference point exploiting the concurrent ranging (i.e., anchors simultaneously emit a UWB signal). Unfortunately, due to hardware limitations and the precision of the timestamps, the system can achieve a maximum position accuracy in the order of a couple of meters. To mitigate this problem in [104] the authors exploit the idea that each anchor sequentially blinks a message, reducing the error on the estimated position below 1 meter.

The next sections delves into the methodologies for implementing the previously described solutions, providing a theoretical perspective and presenting simulative and experimental results. The discussion encompasses various aspects that influence the accuracy of UWB-based systems. The evaluations of applications below explore strategies to optimize the placement of solutions within energy budgets and address scalability concerns.

2.1 The Absolute Localisation System's Role in Safeguarding Industrial Environments

This section introduces an anonymous tracking device tailored for workers and operators in manufacturing and logistics sectors. Utilizing a mesh UWB/BLE approach, the device conserves battery life without requiring a large battery. It dynamically identifies new workers/tags within the monitoring area, independent of time synchronization. Additionally, the device integrates inertial and magnetometer modules to gather comprehensive data on the tracked worker's movements and orientation. This data facilitates detailed analytics to assess worker interaction and measure risk levels in various factory areas automatically. Algorithms provide operators with personalized behavior assessments and risk indices for monitored processes or plant areas. Findings can be used for spatial re-layouts of the workplace and temporal rescheduling activities to minimize Covid-19 transmission risks.

2.1.1 Data analytics for COVID-friendly re-layout

The developed ILS based on the mesh approach is adopted to tackle the COVID spread in workplaces and contagion among operators. For an effective and proactive countermeasure, it is necessary to define in which area, department, or workspace the proposed technology must be used. Then, the anchors must be properly displaced in the monitored layout to avoid possible NLOS problems. Consequently, to ensure a correct COVID safeguard system, each operator involved must wear the developed BLE-UWB tag on her/his belt like a pager or like a pendant badge for the entire shift duration. It is relevant to underline the peculiarities of wearing such devices by workers. Indeed, it would be likely to encounter some reluctance or aversion to such ILS for multiple reasons, from fears of being constantly monitored by the employer to worries of potential health damage due to radio propagation. Thus, several measures have been conceived to mitigate these barriers as:

- participatory design or co-design to involve the final adopters (workers) since the early stages of tag definition to integrate in its design their possible requirements;
- involvement of operators on voluntary basis and informed consent to provide them with all the necessary information about potential effect on the health of the adopted BLE and UWB technologies as well as the usage and access to the data collected by their tags.
- compliance to GDPR requirements for data protection and utilization. In particular, the data collected data by the ILS are not managed by the company in which the ILS is installed and are secure-by-design. In fact, the report generation is provided to the company in an anonymous and aggregated manner, to ensure the highest privacy requirements to the end-users (i.e., the workers).

The proper adoption of the proposed mesh based ILS enables to collect at worker level a set of precious information to prevent and limit the COVID contagion at the workplace. In particular, the proper combination of BLE and UWB allows recording relevant data only in risky circumstances for COVID contamination, i.e., the distance between two or more workers wearing the tag, is less than a specific safety fence (e.g., 2.0 meter). For every time instant in which this safeguard condition is not satisfied, the ILS records a set of information for every operator:

- Indoor location (e.g., occupied area, zone, or workplace with accurate positioning on facility layout).
- Distance between the other workers at decimeter accuracy (e.g., 0.8 m).
- Absolute orientation of the worker (e.g., north-west).
- The timestamp of the human contact (e.g., 13/07/2020-10:04:37).

All the information is locally recorded on the worker's tag. Data are further processed overnight by customized data analytics algorithms to extract value and provide risk assessment measures daily. In particular, the core

TABLE 2.1: Possible classification of risk level for COVID contamination at workplace.

	Risk Level		
Work Process Feature	**Low**	**Medium**	**High**
Worker contact duration [min]	<1	1-5	>5
Worker contact distance [m]	>2	1-2	<1
Worker Contact orientation	Back to back	Shoulder to shoulder	Face to face
Workspace ventilation	Substantial	Limited	Absent
Worker density at workplace [m2/worker]	>4	2-4	<2

of the proposed method consists of comparing the multiple information generated by the worker contacts that occurred during the shift with the layout characterization and the risk factors. Concerning the former, it is necessary to define the most relevant features of the monitored working spaces as their ventilation and the available area in square meters. For the latter, the classification of risk levels must be defined to let the data analytics algorithms automatically assess the COVID contagion risk at the workplace. An example of processed classification is proposed in the following Table 2.1. The aim of the developed data analytics is threefold, and it is summarized in the following. It is important to underline that its purpose is not only the damage containment (number of infected co-workers) in case of an adverse event (employee positive to COVID), but also the prevention of possible contagions by reducing their probability of occurrence.

1. **Prevention of COVID contagion by assessing individual behavior.** The system generates a personalized daily report that can be consulted privately only by each employee, indicating the activities done during the day and where he has been considered at risk of possible COVID contagion. (e.g., at 4:07 p.m., he/she worked for 8 minutes near the test bench with an anonymous colleague at 0.9 m

distance with face-to-face orientation). The daily feedback gives useful guidance to each worker to improve his/her personal behavior at the workplace to protect his/her own health and the community.

2. **Prevention through COVID-friendly re-layout.** It provides a report to the manager/responsible/head of the working area (e.g., warehouse, production plant, office, laboratory, etc.) about the riskiness of the work activities done by his/her employees. This assessment is carried out automatically and quantitatively at fixed intervals (e.g., daily/weekly), evaluating the real interactions within the considered workplace. Thus, the manager is enabled to assess which corrective action to take to reduce the risk of COVID contagion in his/her working area of responsibility (e.g., changing the layout of the workplace, rescheduling the production activities, etc.).

3. **Reconstruction of the COVID contagion chain.** In the unfortunate event that a worker in the facility should test positive to COVID, it would be possible to objectively and accurately trace all the interpersonal contacts that she/he had in the different facility areas in the time window of coronavirus incubation (e.g., 14 days). By leveraging the information collected in the previous days, it would be possible to assess the risk of infection of his/her colleagues accurately for each of them (e.g., personal contact lasted 7 mins, 0.7 m distance, face-to-face orientation, in a small and airless area, etc.) and proceed to the quarantine/medical tests of the employees most at risk of contagion.

2.1.2 Indoor localization System Architecture

An Indoor Localization System (ILS) is a framework that allows to localize an entity, in a given area, as the GPS system normally permits outdoors. There is no standard in terms of the wireless spectrum for indoor positioning due to all the various types of complex indoor environments and different technologies available.

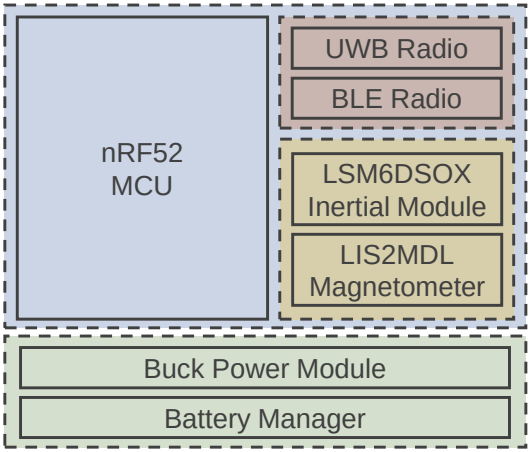

FIGURE 2.2: Wearable Sensor schematic block diagram.

UWB is considered one of the promising technologies for high-precision ILS due to a number of desirable properties, including low energy consumption, centimeter-level range resolution, immunization to multipath, and certain obstacle penetration capability [52]. However, the UWB localization accuracy deteriorates when the signal propagates under non-line-of-sight (NLOS) conditions, like the case of a harsh industrial environment. Therefore, NLOS identification and mitigation have been a popular research topic in UWB localization [105].

A possible strategy to reduce the probability of NLOS condition is to split the environment that we want to monitor into smaller areas covered by different anchors' sets. In this way, the probability of working under NLOS is lower, making the system more robust and accurate. However, this approach requires the ability to discover new tags that can arrive from different sub-area dynamically. Therefore, the proposed tracing framework implements a dynamic node discovery and positioning strategy, allowing adequate flexibility and scalability.

Hardware

The wearable sensor's schematic block is presented in Figure 2.2. As can be noted, it is based on a nRF52[1] low-power MCU from Nordic Semiconductor with integrated Bluetooth functionalities. The MCU is then connected using SPI communication to a DWM1000 module, a fully integrated single chip Ultra Wideband low-power low-cost transceiver IC compliant to IEEE802.15.4-2011. These two modules are provided by Qorvo DWM1001C[2] compact SoM. To detect the moving direction and orientation of the sensor, the device integrates respectively a LSM6DSOX[3] low-power 6D digital accelerometer and gyroscope and a LIS2MDL[4] low-power 3-axis magnetometer. The sensor also integrates a battery charger and a buck power module to provide a stable power line to the DWM1001 SoM and inertial sensors.

Software

The firmware implemented is presented in the flowchart in Figure 2.3 and it is mainly divided into two phases: **1)** Node discovery; **2)** Node Localization

1. **Dynamic Node Discovery**: A master anchor coordinates and schedules the operations to avoid radio collisions and to permit the discovery of new nodes. This, however, poses tight constraints on the tag's battery life, as it must always be in receiving mode waiting for commands from the master anchor that coordinates the network.

   The developed wearable sensor presents different approaches that can be exploited by the master anchor to discover new nodes. The first one is implemented using only the UWB radio and a periodic message sent by the master anchor. The second one exploits the BLE capabilities of the DWM1001 module to discover new nodes periodically.

[1] https://www.nordicsemi.com/Products/Low-power-short-range-wireless/nRF52832
[2] https://www.qorvo.com/products/p/DWM1001C
[3] https://www.st.com/en/mems-and-sensors/lsm6dsox.html
[4] https://www.st.com/en/mems-and-sensors/lis2mdl.html

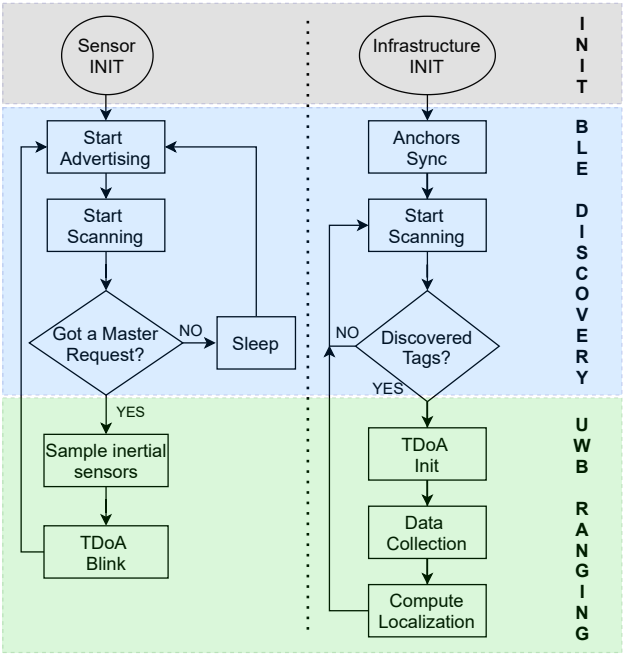

FIGURE 2.3: ILS flowchart. On the left the wearable sensor's flowchart. On the right the infrastructure flowchart

In the presented implementation, the wearable devices are periodically discovered by leveraging BLE Advertising and Scanning functionalities. The discovery window is set to 750 ms to increase the probability of discovering all the nodes in the monitored area before the localization phase.

This strategy avoids keeping the UWB radio in RX mode all the time, and reduces remarkably the wearable tag's energy requirements. In turn, we can achieve the same lifetime with a smaller battery, making the tracking device more compact and less intrusive while worn. The result is a $50 \times 55 \times 20$ mm device. The prototype is showed in Figure 2.4.

2. **Node Localization**: Different approaches exist to estimate a tag's

FIGURE 2.4: Wearable Sensor prototype.

location. Most of the time, they are based on ranging techniques that involve exchanging UWB packets between tags and anchors. These techniques can mainly divide into two methods, Time of Arrival and Time Difference of Arrival. Time of Arrival is the simplest method that can be used to estimate a position [106]. This approach, however, is not suitable for implementing a battery-powered contact tracing system. This due to the large number of messages required to be exchanged between the anchors and the tag to complete a localization cycle.

To enable the capability of tracking simultaneously multiple tags we choose to implement a TDoA approach. TDoA architectures are mainly divided into two categories [107] [108]:

1. **Centralized** In this architecture, a tag emits a signal that is received simultaneously from the anchors. Thanks to a tight synchronization among the anchors, a difference in reception times of the signal with respect to the reference anchor are used to compute the tag's location.

2. **Decentralized**. In this architecture, a signal is emitted from the anchors. The difference in time of signals reception at tag side is used to estimate the position.

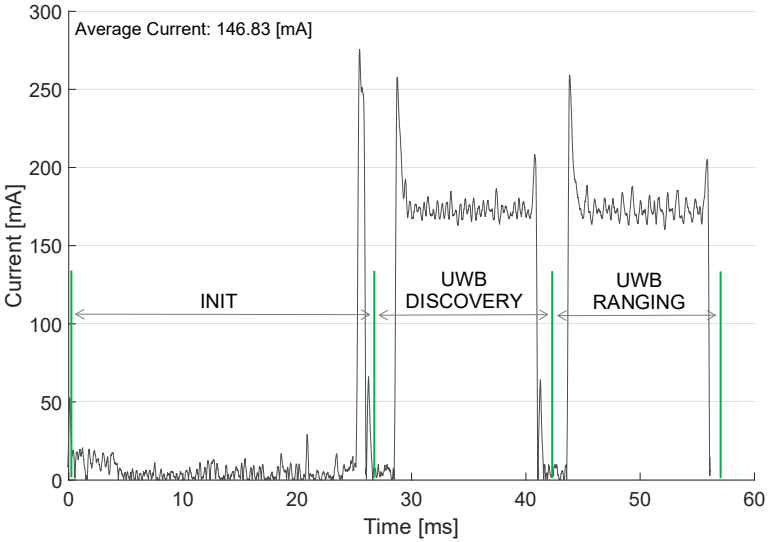

FIGURE 2.5: Power consumption trace of a single execution discovery and localization tasks exploiting only UWB radio. As can be noted, the tasks take around 25 ms to complete (without considering the INIT phase executed only once at startup).

Since the tag location information has to be collected by the infrastructure, we choose to implement a centralized TDoA architecture. Finally, to improve the accuracy of the system, we created an anchor-redundant infrastructure.

2.1.3 Evaluation

Figure 2.5 and Figure 2.6 present the power consumption traces of a tag. Figure 2.5 shows the current consumption when both discovery and localization tasks are implemented using only the UWB radio. Figure 2.6 shows the current consumption for the mesh approach that uses the BLE radio for node discovery and the UWB radio for the localization. A drawback of this approach is the maximum achievable location update rate. In the case of a pure UWB approach, we can achieve up to 40 Hz refresh rate, while the mesh approach can update measurements at 1.6 Hz rate, which is,

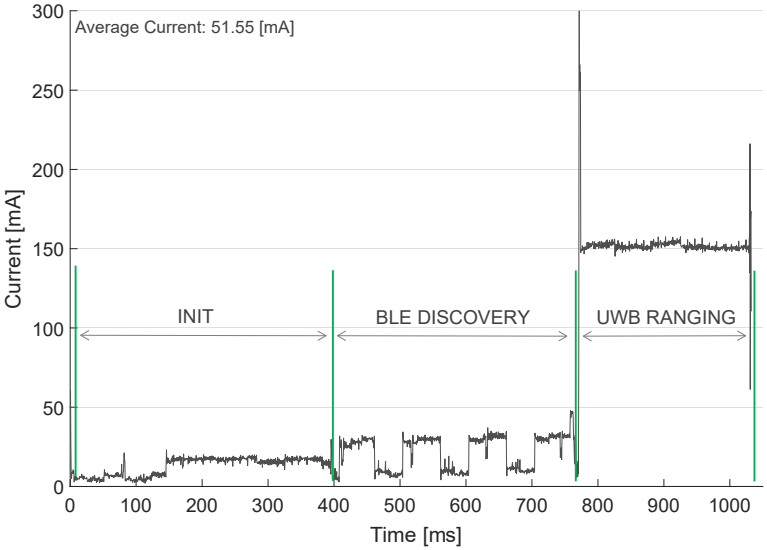

FIGURE 2.6: Power consumption trace of a single execution of discovery and localization tasks exploiting both BLE and UWB. As can be noted, the tasks take around 600 ms to complete (without considering the INIT phase executed only once at startup).

however, enough for the COVID risk assessment service. This can also be noted by comparing Figure 2.5 and Figure 2.6 that present the time needed for a single cycle of node discovery and localization. Even if the localization update rate is lower, the proposed mesh approach allows to gain much higher energy efficiency. For example, in an 8-hour shift, the BLE discovery mechanism reduces battery usage by 65%. Finally, Figure 2.7 presents a preliminary example of the report generated by the proposed work.

2.2 Navigating Spaces: an UWB Relative Localisation System for Pedestrians with Ranging Information

This section aims to conduct an initial investigation into developing a lightweight system, named *Where Are You* (WAY), capable of creating a shared map for every person within the network and resolving ambiguities

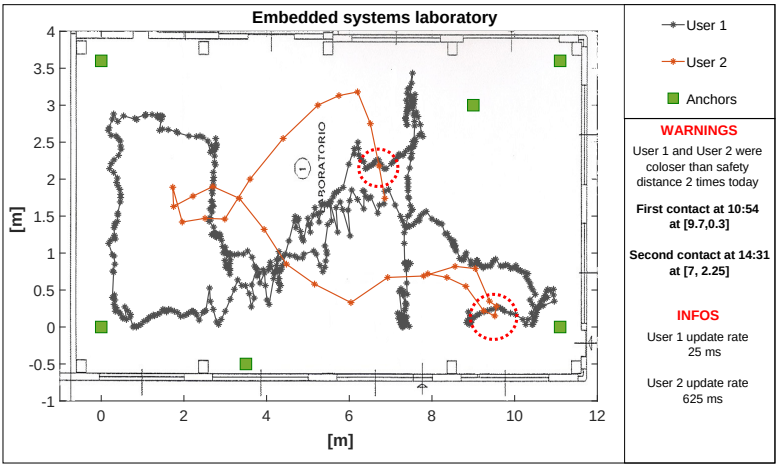

FIGURE 2.7: Example of a report generated starting from the data provided by the proposed system. The orange track shows a tag that implements both discovery and localization using UWB, while the blue one is a tag with a mesh approach. The system detects real-time risk of contagion due to the small distance between employees.

outlined in the introduction of Chapter 2 using only pairwise distances. We determine the minimal information required to address the issue and conduct an uncertainty analysis, utilizing Monte Carlo simulations to assess how ranging uncertainties affect final estimates. Furthermore, we introduce a compact device prototype, utilizing ultrawide-band technology, for experimental purposes to demonstrate the technical feasibility of the solution.

2.2.1 Background and Problem Formulation

Let us consider a set of nodes distributed in a certain area, representing a group of mobile agents (i.e., from now on, each agent is assumed to correspond to one node). We can describe each node by its unknown

coordinate N_i and orientation γ_i, i.e.

$$N = \begin{bmatrix} N_0 & \cdots & N_n \end{bmatrix} = \begin{bmatrix} x_0 & \cdots & x_n \\ y_0 & \cdots & y_n \end{bmatrix}, \\ \gamma^T = \begin{bmatrix} \gamma_0 & \cdots & \gamma_n \end{bmatrix}. \tag{2.1}$$

Let us assume that the i-th node has access to the distances

$$\rho_{i,j} = \|N_i - N_j\| = \sqrt{(x_i - x_j)^2 - (y_i - y_j)^2}, \tag{2.2}$$

so that the symmetric squared Euclidean matrix

$$D = \begin{bmatrix} 0 & \rho_{0,1}^2 & \cdots & \rho_{0,n}^2 \\ \rho_{1,0}^2 & 0 & \cdots & \rho_{1,n}^2 \\ \vdots & \vdots & \ddots & \vdots \\ \rho_{n,0}^2 & \rho_{n,1}^2 & \cdots & 0 \end{bmatrix}, \tag{2.3}$$

can be built. Using the double centring matrix

$$H = I_{n+1} - \frac{e\, e^T}{n+1}, \tag{2.4}$$

where $e\, e^T = \mathbf{1}_{n+1} \times \mathbf{1}_{n+1}^T$, $\mathbf{1}_{n+1}$ is a column vector filled with $n+1$ ones and I_{n+1} is the identity matrix of dimension $n+1 \times n+1$ to transform (2.3), we obtain the Gram matrix

$$G = -\frac{1}{2} HDH, \tag{2.5}$$

that turns pairwise Euclidean distances into pairwise inner products of vectors. Let us define with $P = [p_0, p_2, \ldots, p_n]^T$ the matrix of node coordinates that generates the symmetric Euclidean matrix in (2.3) and that is a replica of N in (2.1) but affected by the geometric ambiguities. In order to derive P, the following optimisation problem has to be solved

$$\arg\min_P ||G - PP^T||^2. \tag{2.6}$$

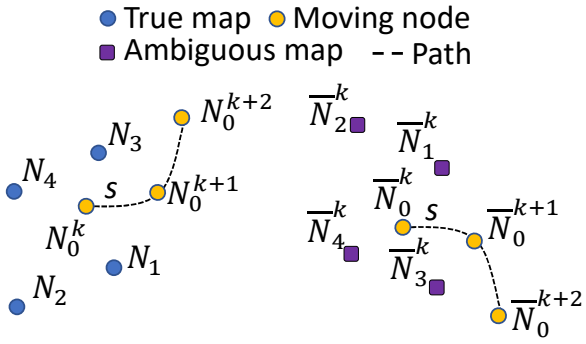

FIGURE 2.8: MDS algorithm may generate an ambiguous map (purple squares), resulting in a wrong final reciprocal position reconstruction.

The solution to (2.6) is given by the eigen-decomposition of (2.5), i.e.

$$P = \begin{bmatrix} p_0 & \cdots & p_n \end{bmatrix} = \begin{bmatrix} \tilde{x}_0 & \cdots & \tilde{x}_n \\ \tilde{y}_0 & \cdots & \tilde{y}_n \end{bmatrix} = U\sqrt{V}, \tag{2.7}$$

where V is the diagonal matrix of the eigenvalues, U the eigenvector matrix of G in (2.5). As aforementioned, the points P are affine transformations of the original set N, i.e., the points in P are rotated and/or flipped versions of the points in N and both verifying the distance matrix D. More precisely, if there exists an angle $\theta \neq 2k\pi$ with $k \in \mathbb{N}$ such that

$$N = \begin{bmatrix} \cos\theta & -\sin\theta \\ \sin\theta & \cos\theta \end{bmatrix} P = R(\theta)P \tag{2.8}$$

then a rotation ambiguity occurs. The flipping problem takes place if

$$N = \pm \begin{bmatrix} -1 & 0 \\ 0 & 1 \end{bmatrix} P = \pm SP. \tag{2.9}$$

An example of geometric ambiguity is reported in Figure 2.8.

Problem formulation and solution overview

Given, $\forall i = 0, \dots, n$, the ranging measurements $\rho_{i,j} + \eta_i$, where $\rho_{i,j}$ is given in (2.2) and where $\eta_{i,j}$ are the ranging uncertainties, we want to estimate the location of all the nodes $\hat{N}$ in a local reference frame centred in one agent, say N_0.

In order to tackle this problem, we first derive an estimate of $\hat{P}$ of the points P, solution of the minimisation problem (2.6). Then, we infer $R(\theta)$ and $\alpha \in \{-1, 1\}$ such that

$$\hat{N} = R(\theta)\alpha S\hat{P}. \tag{2.10}$$

For the this second step, we will use minimalistic information, that is the fact than only one agent, say N_0, moves and we assume the knowledge of its turning direction, i.e., if it turns clockwise and counter-clockwise. We will prove that this information is *necessary and sufficient* to solve the problem at hand. It is worthwhile to note that this information does not need a precise measurement, but just an indicator.

2.2.2 WhereAreYou: the WAY Algorithm

Let us consider three consecutive time instants, i.e., k, $k+1$ and $k+2$, in which the moving node N_0 starts from position N_0^k and moves towards $N_0^{k+1} = N_0^k + t_k$ and $N_0^{k+2} = N_0^{k+1} + t_{k+1}$, where $t_k = [\Delta x_k, \Delta y_k]^T$ and $t_{k+1} = [\Delta x_{k+1}, \Delta y_{k+1}]^T$ are two generic translation vectors, both different from zero (see Figure 2.8). Given the measurements $\rho_{i,j} + \eta_{i,j}$ for such three consecutive time instants, it is possible to build the matrices $\overline{D}^k$, $\overline{D}^{k+1}$, $\overline{D}^{k+2}$ described in (2.3) (we use the $\bar{\cdot}$ notation to denote the measurement results or the function of the measurement results). As described in Section 2.2.1, it is then possible to compute $\hat{P}^k$, $\hat{P}^{k+1}$ and $\hat{P}^{k+2}$, solution of the optimal problem (2.6) given by (2.7).

Then, we first translate $\hat{P}^k$ centred with respect to the moving agent 0, i.e., $\hat{P}_k = \hat{P}_k - \hat{p}_{0,k}$, and then we align $\hat{P}^{k+1}$ to $\hat{P}^k$ by solving the following

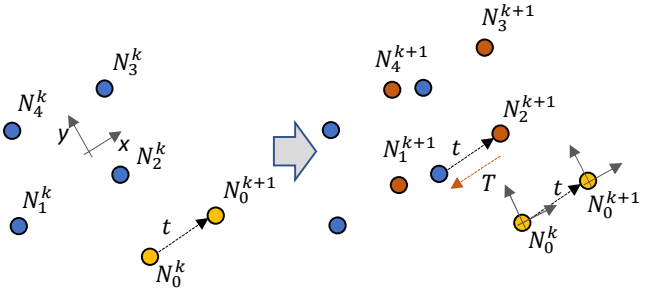

FIGURE 2.9: Geometry of the translation vector T: the displacement computed by the moving node 0 is equivalent to the shift of all the other nodes. Back-projecting T reconstruct the moving node displacements t_k and t_{k+1}.

optimisation problem

$$\arg\min_{\theta,T} \hat{P} = P^k - (R(\theta)\alpha S P^{k+1} + T), \tag{2.11}$$

where θ and T describes the roto-translation between the two sets of points. The situation after this step is depicted in Figure 2.9: the moving node 0 at step k and $k+1$ computes the other nodes' position and centre $\hat{P}^k$ to $\hat{P}^{k+1}$ on itself. From the node 0 view point, the displacement t_k it had taken is exactly the translation T in an opposite direction (see Figure 2.9). As a side effect, the solution of Equation (2.11), once applied also to the points $\hat{P}^{k+1}$ to $\hat{P}^{k+2}$ returns the sequence of motions, i.e. the path, the node 0 has travelled. In essence, we have solved the problem of the localisation of node 0 in the relative frame (i.e., the one centred on the estimated initial position $\hat{p}_{0,k}$) and have solved the mapping of all the other nodes.

However, as discussed in the previous section and explicitly reported in (2.10), the roto-translation does not solve the problem entirely. Indeed, the flipping problem, modelled by α and S remains untouched, whatever is the number of measurement collected, as described in the following theorem.

Theorem 1. *Given a set of $m > 0$ node 0 motions, i.e., $N_0^{k+q} = N_0^{k+q-1} + t_{k+q-1}$, with $q = 1, \ldots, m$, it is not possible to determine αS if no knowledge is*

given about t_{k+q-1}.

Proof. Let us consider the set N in (2.1) and its flipped version $\overline{N} = \alpha S$. Since $\|x\| = \|\alpha S x\|$ (indeed, $\|x\| = \sqrt{x^T x} = \sqrt{x^T S^T \alpha \alpha S x}$), it turns out that

$$\|N_0^{k+q} - N_i\| = \|\alpha S(N_0^{k+q} - N_i)\| = \|\overline{N}_0^{k+q} - \overline{N}_i)\|,$$

which is true for $q = 0, \ldots, m$ and for an arbitrary number of nodes in the network, i.e., $\forall i = 1, 2, \ldots$. This case is depicted in Figure 2.8. As a consequence, given the relative distances (2.2), we obtain the same set of matrices (2.3), hence the same solutions to (2.11). Therefore, without any knowledge about the translations t_{k+q-1}, it is not possible to retrieve αS, which concludes the proof. □

One immediate consequence of Theorem 1 is that (2.11) can only estimate the roto-translation but not the flipping. This situation is depicted in Figure 2.10, where roto-translated locations $\overline{N}_i$ are removed by the solution to (2.11). The following corollary, instead, expresses the minimum amount of additional information needed to solve the flipping problem.

Corollary 2. *Given a set of two node 0 motions, i.e., $N_0^{k+q} = N_0^{k+q-1} + t_{k+q-1}$, with $q = 1, 2$, it is possible to determine αS if the sign of the angle $\beta = \arctan \frac{\Delta y_{k+1} - \Delta y_k}{\Delta x_{k+1} - \Delta x_k}$, i.e., the relative angle between t_k and t_{k+1}, is known.*

Proof. The knowledge of the sign of the angle β is equivalent to the knowledge of the change of direction for the moving agent, i.e., if it is rotating clockwise or counter-clockwise. It is evident to note that a flipping operator as αS transform clockwise rotations into counter-clockwise ones: the knowledge of the sign of β, hence, removes the flipping ambiguity. □

The proof of Corollary 2 is clearly depicted in Figure 2.10, where the flipped locations ${}^{\bar{r}}N_i$ are removed by the knowledge of the angle β: indeed, to be consistent with the distances among the nodes ${}^{\bar{r}}N_i$, the moving node 0 should rotate clockwise from ${}^{\bar{r}}N_0^{k+1}$ to ${}^{\bar{r}}N_0^{k+2}$. The fact that the node has moved in counter-clockwise direction (motion between N_0^{k+1} and N_0^{k+2}), removes the flipping ambiguity.

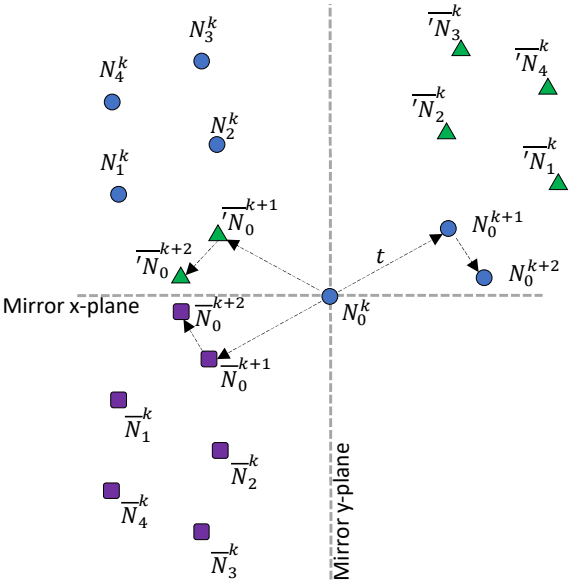

FIGURE 2.10: Removing final ambiguity on the estimated map. Blue circles (N_i) represent the true map, while purple squares ($\overline{N}_i$) and green triangles ($'\overline{N}_i$) are the flipped solutions. Solution to (2.11) removes the set $\overline{N}_i$, while Corollary 2 removes the flipping given by $'\overline{N}_i$.

2.2.3 Uncertainty analysis

To analyse how the ranging uncertainties impact on the final computation, we model the relative distance uncertainties $\eta_{i,j}$ as a white, stationary, zero mean process with standard deviation σ_ρ

$$\overline{\rho}_{i,j} = \sqrt{(x_i - x_j)^2 + (y_i - y_j)^2} + \eta_{i,j} = \rho_{i,j} + \eta_i. \tag{2.12}$$

The distance matrix (2.3) is then computed using the square of (2.12), i.e.

$$\hat{\rho}_{i,j}^2 = \rho_{i,j}^2 + 2\rho_{i,j}\eta_{i,j} + \eta_{i,j}^2, \tag{2.13}$$

TABLE 2.2: Monte Carlo analysis: Theoretical performance of the proposed system against 5 values σ_ρ. All the quantities are expressed in mm

	$\eta_i = 0$ mm				$\eta_i = 100$ mm				$\eta_i = 200$ mm				$\eta_i = 300$ mm				$\eta_i = 400$ mm			
ID	p_1	p_2	p_3	p_4	p_1	p_2	p_3	p_4	p_1	p_2	p_3	p_4	p_1	p_2	p_3	p_4	p_1	p_2	p_3	p_4
μ_x	$< 10^{-3}$	$< 10^{-3}$	$< 10^{-3}$	$< 10^{-3}$	-2	-2	-3	-1	4	-1	-1	-3	-3	-18	-8	-3	11	14	23	7
μ_y	$< 10^{-3}$	$< 10^{-3}$	$< 10^{-3}$	$< 10^{-3}$	-2	-5	-3	-1	1	-6	1	8	5	-11	3	-15	-17	-23	-13	-26
σ_x	$< 10^{-3}$	$< 10^{-3}$	$< 10^{-3}$	$< 10^{-3}$	78	72	75	75	150	157	150	150	229	228	236	222	313	291	289	294
σ_y	$< 10^{-3}$	$< 10^{-3}$	$< 10^{-3}$	$< 10^{-3}$	88	83	89	87	192	191	189	189	257	280	268	285	359	370	381	376

where $2\rho_{i,j}\eta_{i,j}$ has variance $4\rho_{i,j}^2$ and $\eta_{i,j}^2$ is distributed like a chi-square distribution with one degree of freedom. If we consider that $|\eta_{i,j}| << \rho_{i,j}$, it is possible to approximate

$$\hat{\rho}_{i,j}^2 = \rho_{i,j}^2 + \epsilon_{i,j}, \tag{2.14}$$

where $\epsilon_{i,j}$ follows a Gaussian probability density function with zero-mean and variance equal to $4\rho_{i,j}^2\sigma_\rho^2$. Since the estimation process of the node positions $\hat{P}$ is based on a non-linear solution (2.7), which involves an eigenvalue decomposition, it is very complex to derive an explicit solution to propagate the uncertainties starting from the single distance measurements, especially it the number of nodes in the network is larger than 4.

Therefore, the uncertainty analysis has to follow a statistical approach by means of Monte Carlo simulations. In particular, we evaluate the performance of the proposed system against 5 different values standard deviations $\eta_{i,j}$. To randomise on the node configurations, for each level of uncertainty we generated 1000 configurations randomly distributed on an area of 225 m^2. The result of the Monte Carlo simulations are reported in Table 2.2. The system exhibits a linear behaviour with respect to the injected noise $\eta_{i,j}$. Notice that we chose to simulate the ideal case of $\eta_{i,j} = 0$ to validate in simulation the theoretical analysis reported previously.

2.2.4 Results

In this section, the experimental test result is presented to validate the effectiveness of the solution. In addition, a description of the realised prototype and the hardware involved in the experiment is also described.

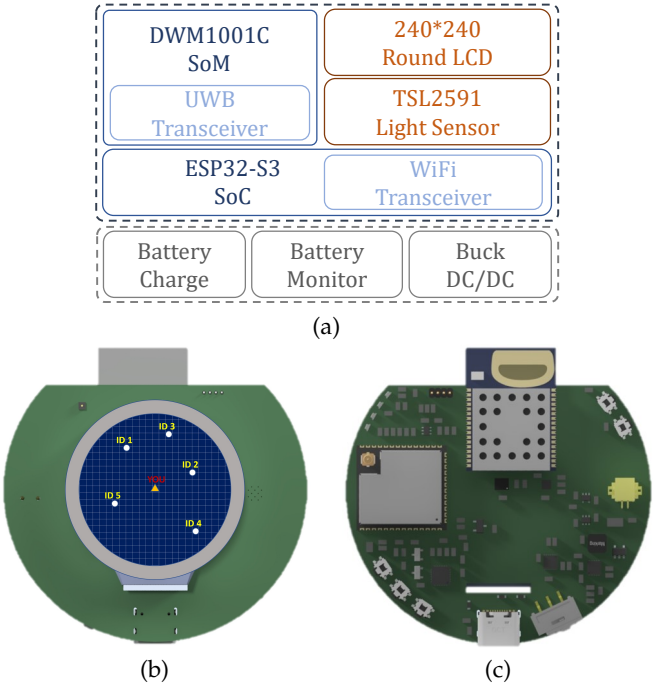

FIGURE 2.11: (a) Schematic block of the proposed device. (b) and (c) 3D rendering of the proposed device.

Hardware Implementation

To evaluate the proposed relative positioning system, a custom, battery powered, portable device was developed. The device, presented in Figure 2.11, is made of COTS components and was developed to be compact, energy-efficient and low-cost. It is based on an Espressif ESP32-S3[5] dual core MCU. It integrates a Qorvo DWM1001[6] SoM for distance measurements and it has a 240×240 LCD display for showing to the user the navigation map, remaining battery level and other useful information. Moreover, it is endowed a complete battery management system for both providing power to the device's peripheral and to charge the integrated

[5]https://www.espressif.com/en/products/socs/esp32-s3
[6]https://www.decawave.com/sites/default/files/dwm1001_datasheet.pdf

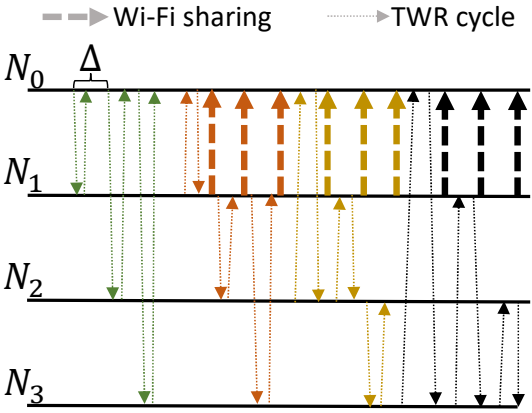

FIGURE 2.12: Scheduling protocol.

LiPo battery and a Luminosity sensor to optimise the energy consumption of the LCD by dynamically change its backlight level. Finally, it integrates a 2000 mAh LiPo battery able to power the device for 5 to 8 hours, depending on WiFi connectivity. During the test, the UWB module was configured to use UWB Channel 5 ($f_c = 6489.6$ MHz, $BW = 499.2$ MHz), a preamble length of 128 symbols, the highest Pulse Rate ($PR = 64$ MHz), and the highest Data Rate ($DR = 6.8$ Mbps). Figure 2.11-(a) presents the architecture overview of the prototype, while device 3D model is presented in Figure 2.11-(b) and Figure 2.11-(c).

Regarding the communication protocol, a TWR [99] is adopted to estimate the distance between two nodes. In particular, the communication is organised into two phases: the first one regards the measurements, while the second is meant to share the data, according to Figure 2.12. The resulting update rate f has a quadratic dependency from the nodes number, i.e.

$$f = \frac{1}{\Delta(n-1)^2}\,, \tag{2.15}$$

where n is the number of nodes and Δ is a predefined time slot in which a node has to complete one TWR-cycle and share via wifi the measurements.

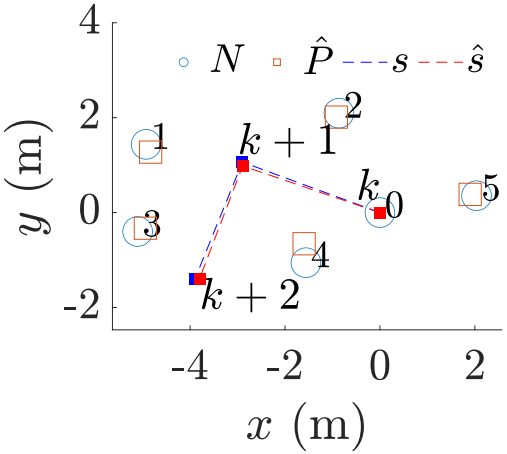

FIGURE 2.13: Experimental results. N (blue circles) represent the true position of the nodes retrieved from the MoCap, $\hat{P}$ (red squares)) represent instead the estimated position using the proposed system. True displacement of the moving node is denoted with s (dashed blue line), while $\hat{s}$ is the estimated displacement retrieved form the algorithm (dashed red line).

For the experimental test $n = 6$, $\Delta = 5$ ms.

Experimental results

The proposed system is finally validated with a laboratory test using 6 anchors, with one that is able to move. We collect 100 inter-distance matrices for each positions, supposed to be taken at time k, $k+1$ and $k+2$. The result is reported in Figure 2.13. To generate a ground truth to assess the obtained results from the UWB relative positioning system, we have acquired the nodes' positions N_i from a Motion Capture (MoCap) system. In particular, the MoCap system adopted is provided by Qualisys with 7 Arqus A9 cameras. The optical tracking system is configured with a working frequency of 240 Hz, with a residual error[7] of lees than 1 mm. Nodes coordinate estimation error are reported in Table 2.3. The mean

[7]The adopted calibration procedure can be found here `https://docs.qualisys.com/getting-started/content/getting_started/running_your_qualisys_system/calibrating_your_system/calibrating_your_system.htm`

TABLE 2.3: Comparison between the true nodes' position N and estimated one $\hat{P}$. All the quantities are expressed in mm.

	e_x	e_y	σ_x	σ_x
$\|N_1 - \hat{P}_1\|$	-95	163	55	119
$\|N_2 - \hat{P}_2\|$	53	82	100	115
$\|N_3 - \hat{P}_3\|$	-160	-70	116	97
$\|N_4 - \hat{P}_4\|$	38	-392	55	310
$\|N_5 - \hat{P}_5\|$	135	-28	175	74
$\|N_0(k+1) - \hat{P}_0(k+1)\|$	-6	-99	-	-
$\|N_0(k+2) - \hat{P}_0(k+2)\|$	81	12	-	-

error on the reconstruction of the moving node in position $N_0(k+1)$ and $N_0(k+2)$ is also reported in Table 2.3. Notice that $N_0(k)$ is known from the beginning: indeed, since we are referring to relative positions, $N_0(k)$ is assumed to be known and placed in the origin of the reference frame.

The experimentally retrieved ranging standard deviation is about $\sigma_\rho = 100$ mm. The experimental results shows a nice matching with the Monte Carlo simulations in Table 2.2. We argue that the motivations for the non perfect matching could be traced to the non perfect-isotropic radiation pattern effect of the UWB antenna and the delay introduced by the internal circuitry. Moreover, although the non-line-of-sight (NLOS) condition is beyond the aims of this study, the data gathered during the experiments are intentionally collected without particular attention to possible NLOS conditions, i.e., a realistic conditions, which exacerbate the difference with the theoretical Monte Carlo simulations results. Finally, in the experimental results collection has been performed without a calibration phase, since the nodes are assumed to be deployed randomly in the environment.

2.3 Beyond Devices: Harnessing Cost-Effective Bistatic Radar and Ultrawide-Band Radios in a Device-Free Localisation System

This application evaluates the feasibility of a radar-like localization system using commercial-off-the-shelf components, particularly the DecaWave's

DWM1001 UWB transceiver. By assessing the relationship between target speed, baseline, and sampling frequency, the study demonstrates the potential for an inexpensive UWB-based radar solution.

2.3.1 Related Work

RF-Based DF localization techniques usually rely either on Radio Signal Strength (RSS) or Channel State Information [109] (CIR/CSI) techniques. For what concerns RSS methods, in the literature, we can already find notable examples as [110]. Another interesting approach is Radio Tomography Imaging (RTI) [111]. RTI uses the shadowing created by the target between a couple of anchors to reconstruct an interference image of the environment. Shadowing is measured as either drop-in RSS mean or increased RSS variance. Another RSS-based approach is presented in [112], where temporal variations in node RSS measurements are linked to the target position through a new RSS model. While previous RSS-based solutions located a target only by estimating non-line-of-sight conditions, which are caused among couples of anchors, this work also makes use of target-induced multi-path components for localization. Unfortunately, RTI based approaches require first collecting an RSS fingerprinting with a pre-deployment data gathering and a training phase.

Concerning CIR/CSI based methods, they are inherently less coarse in terms of positioning accuracy and precision and more informative/stable with respect to RSS measurements. Previous works have focused on UWB pulse radars before [98, 113–116], though these projects were based on DWM1001's more capable but more expensive alternative, the TREK1000. In [115] authors present a system based on a single TX/RX UWB couple transceivers using CIR-based fingerprinting to localize a moving person. Fingerprint collection involves CIR measurement as a person moves on a grid to create a feature map that the localization algorithm can later use. In this case, MPC magnitude and phase information are stored in a feature table representing the point in the grid where the person was standing. MPC components in this work are relative to the environment and are not target originated, unlike in other CIR-based works: by assuming that the

environment is known – making the position of environment-caused reflections known – it is possible to associate the amplitude and phase change with the target's motion. Finally, position estimation results from a trained kNN machine learning algorithm, finding the closest matching fingerprint to the measured CIR. It is worth noting that, to overcome the problem of model training, avoiding the need for feature map creation, authors have also proposed a knife-edge diffraction radio propagation model as future expansion, linking target position to MPCs phase and amplitude variation. In [117] a WiFi-based system that doesn't require offline training or the construction of a database on deployment is proposed, overcoming the problem of a fingerprint map, and linking the target position and measured CSI through a model.

In [98] authors implement a multi-static UWB radar network to track CIR variance in the area associated with MPCs caused by a moving target. While the variance detection in this work is based on a background subtraction and thresholding algorithm, Chenglong [113] proposes to use a CNN network to detect the target path position within the CIR. Despite the promising results, the proposed method needs a preliminary training phase specific to the deployment environment. Another interesting work in the UWB radar development is [114]: in this work, Pearson's correlation is computed between background CIR and incoming CIR, as it was noted that the presence of a moving human formed uncorrelated peaks in the area after the target path location in the CIR.

2.3.2 Methodology

In this paragraph, we briefly introduce the proposed model for estimating the location of an entity inside an area under monitoring. The idea is to exploit a model describing the RF propagation of a UWB signal. In our case, we use the DWM1000 CIR accumulator to derive the MPC components relative to the entity we want to track.

The Channel Impulse Response can be modeled as shown in the Equation (2.16) and presented in [116]. It consists of a sum of deterministic

multipath components with amplitude a_i and delay τ_i and diffuse multipath components modeled as Additive Gaussian White Noise whose autocorrelation is equal to equation (2.17).

$$h(t) = \sum_{i=1}^{i=L} a_i \delta(t - \tau_i) + \nu(t) \tag{2.16}$$

$$E(\nu(t)[\nu(\tau)]*) = S(t)\delta(t - \tau) \tag{2.17}$$

The reflected signal can then be modeled as a delayed signal transmitted from virtual anchors. The delay tau_i in the Equation (2.18), represents the time of flight between the $i - th$ virtual anchor a_i and the receiver p for the $i - th$ multipath component.

$$t_i = \frac{1}{c} \|p - a_i\| \tag{2.18}$$

This model assumes that deterministic MPCs are the delayed and attenuated versions of the transmitted signal. In this case, we chose to neglect the distortion that the UWB pulse experiences due to Fresnel reflection coefficient [118].Considering the bistatic radar configuration as shown in Figure 2.14, composed of a single transmitter-receiver pair, the distance at which the target is detectable depends on several parameters such as the peak transmitted power and the sampling resolution of the receiver [119]. Table 2.5 shows the available CIRs length, which represents the window within it is possible to detect an echo, and it is calculated in Equation (2.19).

$$w = c \; l \; t_{ref} \tag{2.19}$$

where c is the speed of light, l is the length of the CIR and t_{ref} is the unit time of each CIR's sample. Imposing the equation system

$$\begin{cases} \frac{\tau_{LOS}^{FP\ 2}}{4} + \tau_R^2 = \tau_T^{Rx2} \\ \frac{\tau_{LOS}^{FP\ 2}}{4} + \tau_R^2 = \tau_T^{Tx2} \\ \tau_T^{Tx2} + \tau_T^{Rx2} \leq w \end{cases} \tag{2.20}$$

we can compute the maximum target distance for which the delayed echo

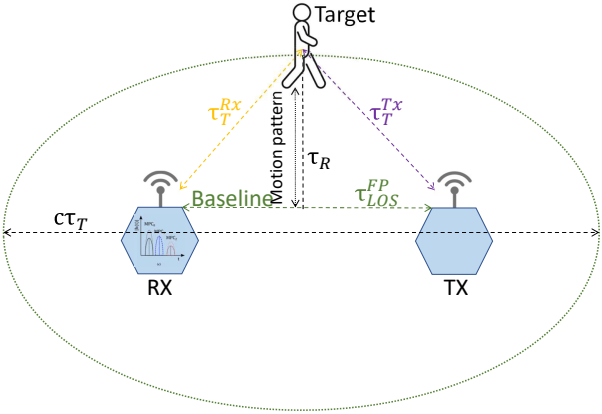

FIGURE 2.14: Bistatic radar configuration. τ_{LOS}^{FP} is the time of flight (ToF) in line-of-sight condition between receiver and transmitter, τ_T^{Rx} and τ_T^{Tx} is the ToF of the reflected signal between target and receiver and transmitter, respectively, τ_R the ToF with respect the centre of the bistatic radar and the target and τ_T is the major axis of the ellipse.

falls inside the observation window. Figure 2.15 shows the maximum geometrical distance at which a target can be identified. This is a simple view of the problem with respect to the problem's formulation presented in [119], considering only the window's length of the collected echoes.

DW1000 CIR estimate

The CIR can be exploited to retrieve information about how signals travel in the air between a couple of transceivers. A single, narrow, and powerful UWB pulse is usually generated at the transmitter side, to collect a CIR measurement. On the receiver side, the impulse response can then be collected [120]. A common method is the so-called *matched filter* [121]. This approach foresees the transmission of a signal whose auto-correlation function is close to a Dirac delta. On the receiver side, the cross-correlation of the incoming signal with the known transmitted signal can be exploited to estimate the CIR.

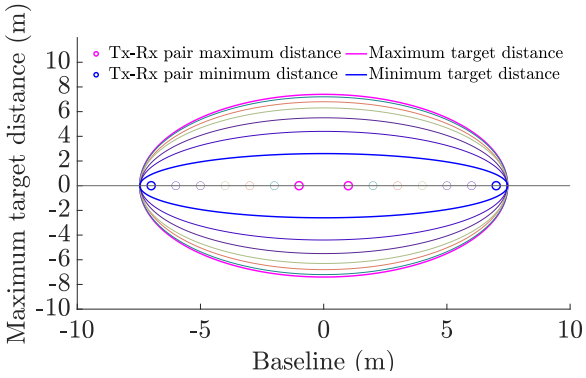

FIGURE 2.15: Different configuration for the bistatic radar, varying the values of the distance between the transmitter and the receiver.

TABLE 2.4: DW1000 supported UWB channels.

Channel	Center frequency (MHz)	Bandwidth (MHz)
1	3494.4	499.2
2	3993.6	499.2
3	4492.8	499.2
4	3993.6	1331.2
5	6489.6	499.2
7	6489.6	1081.6

As reported in Table 2.4 and Table 2.5, the DW1000 can be configured by setting the channel, the Pulse Repetition Frequency (PRF) configuration, the data rates (110 kbps, 850 kbps, and 6.8 Mbps), and the preamble code.From the IEEE 802.15.4z-2020 standard, the UWB limits the maximum transmitted energy to 37 nJ for a 500 MHz bandwidth. The PRF influences the radios' peak power transmitted in the air, and the maximum detectable target distance. The number of samples, that the CIR accumulator can hold, depends on the PRF selected, according to Table 2.5. Each CIR sample corresponds to an accumulator tap, which is half the period of the fundamental frequency – equal to 499.2MHz in this case – and it is represented by a complex number with 16 bit signed integer real and imaginary part, $\Re_i + \Im_i$.

TABLE 2.5: CIR characteristics with varying PRF.

Mean PRF	Accumulator size	Sample capacity	Symbol time
16 MHz	3968 bytes	992 samples	496/499.2 μs
64 MHz	4064 bytes	1016 samples	508/499.2 μ s

Each sample's amplitude is computed as shown in the equation (2.21)

$$\mathcal{A} = \frac{1}{K} \sum_{1}^{K} \sqrt{\Re_i^2 + \Im_i^2} \tag{2.21}$$

where K is the number of preamble accumulated symbols. Accumulation stops either when SFD is detected [114], when the memory needed for storing signed integer values representing real and imaginary parts of a sample within the CIR accumulator grow to be 16 bit numbers, or if SFD timeout condition is reached. Once collected, the CIR has to be normalized with respect to the number of accumulated preamble symbols, as the CIR is the result of the accumulation of the correlator output over the detected preamble symbols [122]. The DWM1001 chip uses CIR estimation to support the timestamping of the RMARKER of a message with a 15.65 ps precision. This is done thanks to DecaWave's internal Leading Edge Detection (LDE) algorithm, which determines the index of the direct path component within the collected CIR. This is implemented using a dynamic threshold that adjusts the RX timestamp estimation, also correcting the delay introduced by the antenna.

Proposed solution

A static environment around a TX-RX couple always provides the same response to a know RF signal, meaning that it always responds by producing the same MPCs. When we introduce a moving object within the environment, new MPCs linked to this entity will appear within the CIR. By subtracting the newly obtained CIR to the previous static CIR, which represents the background CIR, we obtain a signal with just the MPCs components caused by the moving entity at the so-called target path location, τ_{TP}. The difference between τ_{TP} and the identified direct path component

TABLE 2.6: DWM1001 configuration parameters: standard SFD and PHY header mode are used, SFD timeout is set to 129, transmitted power gain is set to 19 dB.

Channel	PRF	Pr. length	PAC	Preamble code	Data rate
4	16 MHz	128	8	7	6.8 MHz

TABLE 2.7: Tested conditions.

Mean PRF	Baseline	Rounds walked	Target average velocity
16,64 MHz	1.2,2.1 m	1,2,3	0.13, 0.26, 0.39 m/s

τ_{DP}, constrains the object location p_{TP} to an ellipse having focal points located at p_{RX} and p_{TX} as described in the Equation (2.22).

$$\|p_{RX} - p_{TP}\| + \|p_{TX} - p_{TP}\| = c(\tau_{DP} - \tau_{TP}) \tag{2.22}$$

To obtain τ_{TP} from the incoming CIR measurements, we use the algorithm described in [98], having the DWM1001 configured as reported in Table 2.6.

2.3.3 Experimental Setup

To assess the effectiveness of our method, the experimental setup consists of a single orthogonally oriented transmitter-receiver couple, as shown in Figure 2.14. The two UWB transceivers are configured to sample the environment at a frequency of about 125 Hz

Results

The experiments consider target speed, TX-RX baseline, and mean PRF on the detection of the identified target distance along the orthogonal direction with respect to the baseline, as shown in Figure 2.14.

To highlight the investigated phenomena, a back-forward motion is adopted, changing the repetition of the movement. Table 2.7 shows the different tested conditions. In Figure 2.16 is reported the experiment for

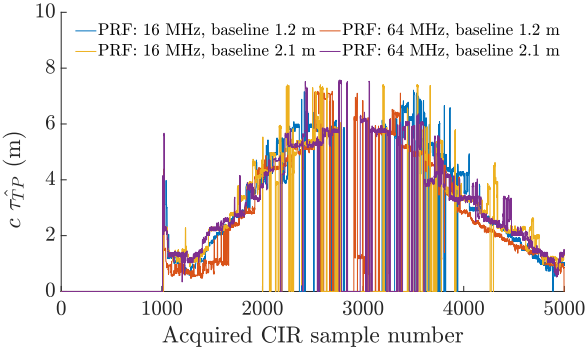

FIGURE 2.16: Estimated target distance $c\tau_{TP}$ with target speed 0.13 $\frac{m}{s}$.

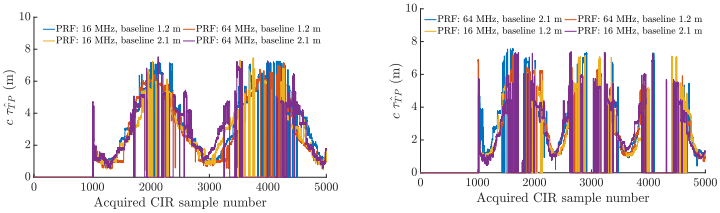

FIGURE 2.17: In (a) Estimated target distance $c\tau_{TP}$ with target speed 0.26 $\frac{m}{s}$; in (b) Estimated target distance $c\tau_{TP}$ with target speed 0.39 $\frac{m}{s}$.

unique backward-forth motion with a walking speed of about 0.13 $\frac{m}{s}$. The x-axis reports the number of the acquired CIR, and the y-axis estimates the target distance from the baseline. Figure 2.17-(a) and Figure 2.17-(b) describe the results obtained for different repetition numbers of the motion pattern, confirming that the estimated distance reflects the real motion.

In all experiments can be observed that the estimation $c\tau_{TP}$ at the maximum distance of the target fails.According to the theoretical maximum detectable distance, as shown in Figure 2.15, the extreme position of the target resides on the limit bound of the ellipse, calculated without considering system losses, causing the non-observability of the target from radar. In Figure 2.18

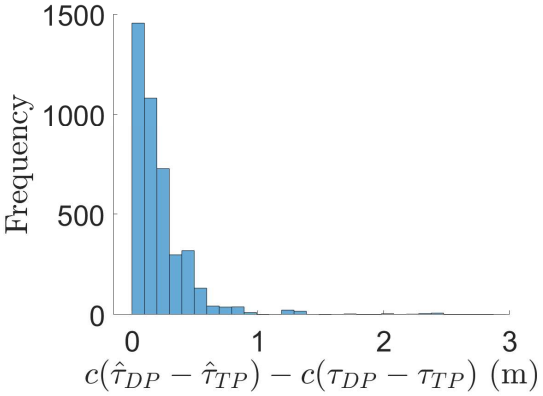

FIGURE 2.18: Error on the estimated distance by the bistatic radar. The ground truth is a motion capture system power by Qualisys.

is shown the histogram of the estimated distance error using as ground truth a motion capture. The proposed bistatic radar has a mean error equal to 16 cm and a variance 33 cm.

2.4 Invisible Trails: Unveiling the Capabilities of a Tag-Less Ultrawide-Band Passive Tracking System

This section builds upon the initial evaluation presented in Section 2.3 of an ultrawide-band bistatic radar, delving into the following aspects:

- We introduce a cost function to improve the estimates;
- We realised a distributed system to detect and track moving entities in the surrounding environment;
- We developed an IoT architecture to handle and sort the data using as much as possible the available bandwidth of the chosen UWB module;

- We enhance the processing update rate of the receiver, improving the maximum target velocity that the proposed system can track.

2.4.1 Background and Problem Formulation

This paragraph provides a brief overview of the equations and models utilised position estimation of a mobile entity. However, for a more detailed understanding, we refer to our previous work that provides an in-depth reference on the topic [68].

Without compromising generality, we assume a scenario with three UWB transceivers consisting of one transmitter and two receivers deployed in a known area. We can describe each node by its known coordinates P_i, i.e.,

$$P = [P_1^{TX}, P_2^{RX}, P_3^{RX}] = \begin{bmatrix} x_1 & x_2 & x_3 \\ y_1 & y_2 & y_3 \end{bmatrix}. \tag{2.23}$$

By employing the UWB signal propagation model and sequentially gathering CIRs, we can extract the multipath components scattered from the target we intend to track. The Channel Impulse Response model, which includes deterministic multipath components with amplitude a_i and delays τ_i, and diffuse multipath components $\epsilon(t)$ modelled as Additive Gaussian White Noise is reported next

$$h(t) = \sum_{i=1}^{l} a_i \delta(t - \tau_i) + \epsilon(t), \tag{2.24}$$

where l is the length of the CIR signal and where the autocorrelation of the uncertainty $\epsilon(t)$ is given by

$$E(\epsilon(t) * \epsilon(t)) = S(t)\delta(t - \tau). \tag{2.25}$$

The tracked target can be considered as a virtual anchor with coordinates $P_T = [x_T, y_T]^T$ that transmits a delayed and attenuated version of the original signal emitted from the transmitter. The time of flight t_i between the receiver P_i^{RX} and the target for the i-th multipath component is given

by

$$t_i = \frac{1}{c}\|P_i - T\|. \tag{2.26}$$

Considering a bistatic radar configuration as reported in Figure 2.14, the maximum distance at which the target is detectable can be calculated using the transmitted power peak and the sampling resolution of the receiver [119]. By imposing the following system of inequalities (2.20) we can compute the theoretical maximum distance for which the delayed signal falls inside the observation window permitted by the selected hardware, i.e., the hardware enables varying CIR lengths, which establishes the maximum duration of the observation window. In (2.20), the observation window is denoted by w, the speed of light by c, the length of the CIR by l, and the unit time for each CIR sample by t_{ref}. Additionally, we define τ_{LOS}^{FP} as the time-of-flight (ToF) in line-of-sight (LoS) between the transmitter and receiver, τ_R as the ToF between the target and the baseline of the bistatic radar, and τ_T^{Rx} and τ_T^{Tx} as the ToF between the target and the receiver and transmitter respectively.

The CIR signal should remain constant in a stable environment, but due to the instability of transmitters and receivers, a phase difference can occur between them. As a result, when a single receiver samples the CIR of a packet, the sampling point may differ from the previous sample. This sampling drift can be utilised to accumulate data and generate a more detailed structure of the CIR. In other words, by exploiting clock drift, we can obtain multiple samples, resulting in a wider sample rate compared to a single sampling operation. Once a series of consecutive CIRs are obtained, they can be aligned based on the line-of-sight (LOS) peak time instant τ_{LOS}^{FP}.

In a static environment, a TX-RX couple will consistently produce the same response to a known RF signal, resulting in the same Multipath Components (MPCs) being generated. As such, the model of the background response h^B through the CIRs measurements can be obtained. A moving object into the environment results in new MPCs within the CIR associated with this entity. Computing the differences between the incoming and the background CIRs, the MPCs components coming from the moving entity can be determined. Considering each bistatic configuration of the

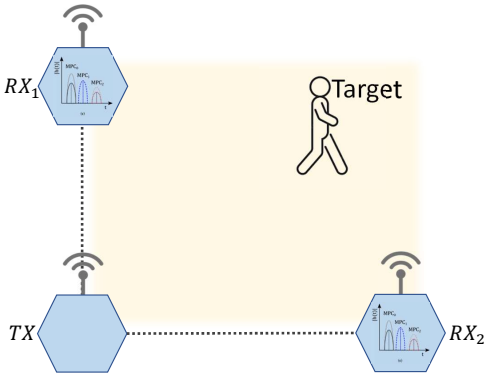

FIGURE 2.19: Representation of the detection area identified by anchors and transmitter.

system proposed in Figure 2.14, the target's position P_T, is subject to the constraint of lying on an ellipse. This ellipse has focal points located at P_1^{TX} and P_i^{RX}, major axis equal to $c\ \tau_T$, and is described by (2.22) where τ_T is obtained using a variation of the algorithm described in [68, 98]. Once the location P_T is determined, we implicitly obtain the ranging information. With two receivers, we can compute the target position within the convex area defined by the line-of-sight between each couple TX-RX as shown in Figure 2.19, with a maximum detecting range defined by (2.20).

Position estimation

Once τ_T is obtained, different approaches could be used to estimate the coordinate of the target $\hat{P}_T = [\hat{x}_T, \hat{y}_T]^T$. For example, in [123] a method is presented that employs analytical techniques to determine the intersection points of multiple ellipses. In [124], an ellipse-resampling particle filter is developed for cooperative target tracking. This study does not focus on creating a complex estimation filter. Instead, we aim to enhance the precision of the raw data, which motivates the use of a particle filter. The particles' movements are modelled using a random walk, meaning that the

position of each particle $p = [x_p, y_p]^T$ is assumed to change over time as

$$\begin{cases} x_p^{t+\Delta t} = x_p(t) + \Delta t \eta_{x_p}(t), \\ y_p^{t+\Delta t} = y_p(t) + \Delta t \eta_{y_p}(t). \end{cases} \tag{2.27}$$

At each prediction step, particle positions are updated with Δt, that is the elapsed time since the last measurement reception. The random variables $\eta_{x_p}(t)$ and $\eta_{y_p}(t)$ are a realisation of a stochastic process that follows a normal distribution with zero mean and standard deviation σ_η. Whenever an estimated $\hat{\tau}_T$ is received, the particles' weights are updated according to the marginalisation

$$w_p = p(\tau_T | \hat{\tau}_T), \tag{2.28}$$

where the expected τ_T is calculated using (2.22).

Problem formulation and solution overview

Considering a multi-static radar as depicted in Figure 2.19 and given the CIRs measurements $h(t)$ in (2.24), we want to improve the $(\hat{\tau}_T^{RX_1}, \hat{\tau}_T^{RX_2})$ estimates. Besides, an IoT architecture capable of handling, sorting, and processing the CIRs measurements to estimate the target location $\hat{p}_T$ within the tracked area is required.

We have developed an IoT infrastructure using MQTT for realising data sharing between the UWB nodes and the processing unit. We have also introduced a new cost function to enhance the estimates of $\hat{\tau}_T$ and increased the update rate of the bistatic radar, thus making the infrastructure more flexible and user-friendly. Moreover, to prevent the bottleneck effect, we have implemented a message size reduction strategy to minimise the data transmitted within the IoT network.

2.4.2 Solution

To estimate the target distance from each TX-RX couple, we need to build the RF response of the static environment by using consecutive CIR measurements h. Once the background model h_B is computed, to highlight the

foreground h^F, i.e., the moving objects, the following background subtraction technique is performed

$$h^F = h - \alpha h_B, \tag{2.29}$$

where $\alpha \in (1, 2]$ is a constant value that scales the background signal to avoid ripples for very small values after applying (2.29). To improve the precision of the estimate of $\hat{\tau}_T$, we introduce a cost function to weight each single values of the signal h^F, i.e.

$$\text{cost} = W(h_i^F, h_j^F) \frac{h_i^F}{h_{max}^F} \frac{h_{peak}^F}{h_{max}^F}, \tag{2.30}$$

where $W(h_i^F, h_j^F)$ is the observation window, whose length is defined by the number of elements in $\{i, \ldots, \min\{j \in \mathbb{N} | h_j^F \leq h_i^f \wedge j \geq i\} - 1\}$, h_{peak}^F is the value of the the first peak within $W(h_i^F, h_j^F)$, h_i^F is the i-th sample of the resulting signal h^F, and h_{max}^F the maximum value of the entire CIR.

The cost function in (2.30) emphasises the significance of several factors that affects the estimate of $\hat{\tau}_T$. One such factor is the window dimension, since it should be large enough to ensure that the detected target has produced multiple MPCs that were not present in the background model. The starting value h_i of the window is also essential, as a higher value suggests that the target detection is more significant. Finally, the first peak value is critical since it indicates the direct multipath generated when an object enters the scene. This value should be sufficiently high to ensure that the starting point of the window coincides precisely with the direct multipath time location $\hat{\tau}_T$. To avoid erroneous timestamps transmitted by the receivers, caused by the influence of ambient noise that may lead to a faulty reading of the complex values to reconstruct the CIR, the incoming signals are filtered by a Gaussian filter. At this stage, we can multiply the value of $\hat{\tau}_T$ by the speed of light c to obtain the estimated distance between the i-th radar baseline and the target. Once at least two measurements $\hat{\tau}_T$ are collected, we can use the particle filter to estimate the target position.

Sensor data is gathered and transmitted to a Raspberry Pi via the UART

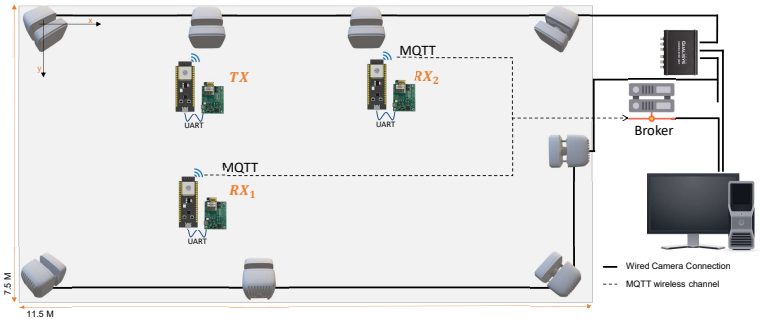

FIGURE 2.20: Experimental setup

interface, which enables string-based data transfer. As a result, all important sensor data must be serialised to obtain a string of data representing the incoming information in ASCII format. To optimise the performance in real-time applications, we strive to keep the size of the transmitted data as small as possible.

After decoding all the data, they need to be sent to the central computing unit for processing and extracting the location of the tracked object. To achieve this, we utilise MQTT middleware, which operates on a publish/subscribe protocol. The overall architecture is reported for reference in Figure 2.20.

2.4.3 Experimental Results

We performed multiple tests to evaluate the proposed architecture and the effectiveness of the cost function. Initially, we concentrated on a single couple TX-RX, to assess the effectiveness of the previously depicted estimation process of τ_T. This first phase is also helpful to highlight the issues related to the reconstruction using sequential CIR measurements and the leading edge detection algorithm

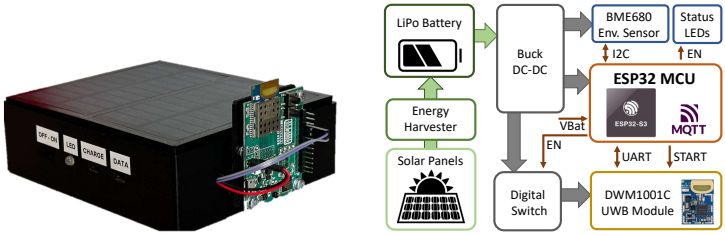

FIGURE 2.21: In (a) the developed prototype, in (b) the HW architecture.

Hardware

We have developed an UWB radar node, as shown in Figure 2.21, to implement the proposed IoT architecture. The UWB radio module is built around the Qorvo DWM1001 transceiver, compliant with the IEEE 802.15.4-2011 standard [125]. It can operate on six different frequency bands with centre frequencies ranging from 3.5 to 6.5 GHz and bandwidths of either 500 or 900 MHz. The chip can measure range and retrieve the measured CIR, and it offers three different data rates: 110 kbps, 850 kbps, and 6.8 Mbps. The DW1000 timestamps transmitted and received frames with a precision of 40 bits, using a nominal 64 GHz resolution. This results in a timing precision of 15.65 ps for packet timestamps. The UWB module is connected to an Espressif ESP32 microcontroller through the UART port. This microcontroller is powered by the Xtensa dual-core 32 bit LX6 microprocessor with a clock speed of up to 240 MHz. It also features WI-FI and Bluetooth modules enabling seamless wireless network integration. The microcontroller is also optimised for low power consumption, making it well-suited for wireless IoT applications. In order to facilitate tracking in areas without access to electricity, we have incorporated two solar panels to power the radar node. We track the experimental area using both the radar system and a motion capture system, which provides the ground truth to evaluate the accuracy of the proposed system. For the following experiments, we used a motion capture system provided by Qualisys with 8 Arqus A9 cameras, a synchronisation unit, and a dedicated workstation (see Figure 2.24).

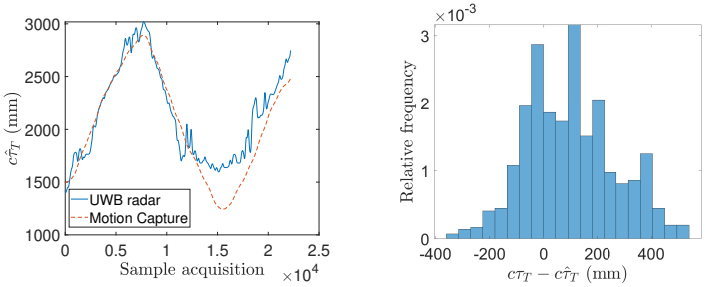

(a) (b)

FIGURE 2.22: In (a) comparison between the distance estimated by our approach (blue line) and distance retrieved by the motion capture (dashed-orange line), in (b) the histogram of the error.

One crucial factor to consider in the setup is the placement of the sensors within the environment. It is imperative to position the receivers at a distance from each wall in the room that is not similar to the distance estimated for the tracked entity. Otherwise, the wall could cause a peak in CIRs, leading to a false detection by the leading edge detection algorithm. In order to address this issue, it may be advisable to relocate the transceiver nearer to the wall. However, in our particular experimental configuration, this course of action is not feasible due to the physical limitations imposed by the furniture and the requirement to connect the receivers to a USB cable for the purpose of downloading supplementary data that is crucial to validate the proposed system.

Results

Initially, a single couple TX-RX is used to evaluate the proposed method's effectiveness in distance calculation. In Figure 2.22-(a) is shown the results of the experiment conducted while performing a backward-forth movement with a varying motion speed ranging from 0.5 m/s to 1.5 m/s. As highlighted in Figure 2.22-(a) and described in the previous work [68], regions that are closer or farther away from the bistatic radar exhibit greater errors in the distance estimation. In Figure 2.22-(b) is reported the histogram of

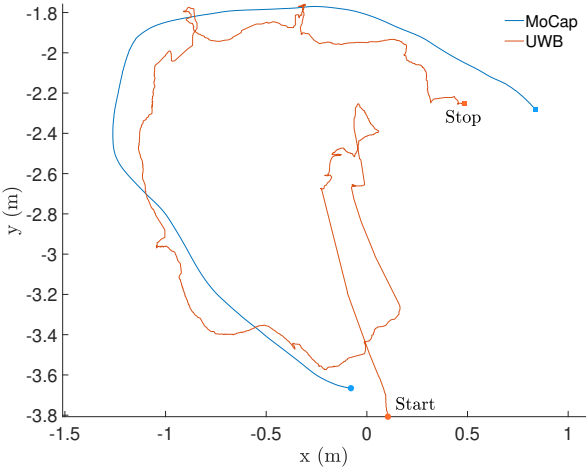

FIGURE 2.23: Comparison between target path estimated by UWB and by the MoCap.

the experiment, with a mean error $\mu = 101$ mm and a standard deviation $\sigma = 195$ mm.

It is worthwhile to note that the sampling rate of the receivers is fundamental. In our previous work [68], we limit the target velocity to be lower than 0.15 m/s to account for the system sampling rate and increase the tracking precision. Indeed, the bottleneck of the previous architecture was related to the bandwidth of the UART interface. Due to this constraint, we take care of the data encoding and, after the fine-tuning the algorithm, the system can now process and transmit data via MQTT at a frequency of 115 Hz, which is four times the previous work, that was capable of operating at 30 Hz rate.

Finally, Figure 2.23 shows the result of one tracking experiment. After the initial stage of convergence, the estimated position has an RMSE($\hat{P}_T$) of approximately 30 centimetres.

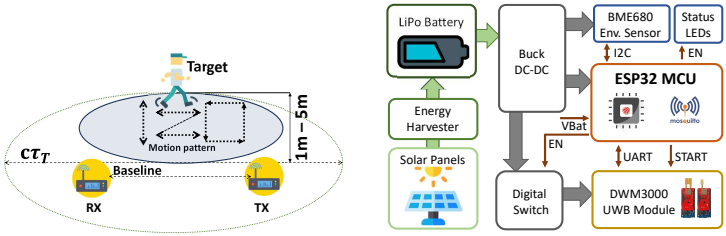

FIGURE 2.24: In (a) experimental setup. A single couple Tx-Rx oriented in the same direction. The receiver analyses CIR to identify the time delay of the target and computes the distance. The target performs various motion patterns within a range of 1-5 m. In (b) radar node prototype.

2.4.4 Crossing Channels: Assessing the Performance of UWB Bistatic Radar Sensors in an Across-Channels Evaluation

With the availability of new commercial-off-the-shelf UWB modules that also integrate the transmission channel 9, operating at a center frequency of 7987.2 MHz, additional tests are conducted to assess the potential for enhancing the accuracy of the DFL systems. To evaluate the effectiveness of our method, we designed an experimental setup consisting of a single transmitter-receiver pair aligned in the same direction, as depicted in Figure 2.24-(a). Both the UWB transceivers were configured to sample the surrounding environment at a frequency of approximately 125 Hz.

Hardware

The DWM3120 is a second-generation, fully integrated UWB transceiver developed by Qorvo as part of their DW3000 family. It follows the IEEE *802.15.4z* and has the new communication channel 9, operating at a carrier frequency of 7987.2 MHz. Moreover, it is optimized for low-power battery-operated operation, making it suitable for a wide range of mobile, consumer, and industrial applications. To ensure smooth integration into networks, we have developed a prototype whose hardware architecture enables seamless connectivity as depicted in Figure 2.24-(b). The prototype is endowed

with a *Espressif ESP32* microcontroller, a cost-effective and energy-efficient device that comes with built-in WiFi and Bluetooth functionalities; a *TP4056* handling the charge of the batteries; a 3.7 V 1900 mAh LiPo battery; two 5V 1W photovoltaic panels.

Preliminary experimental results

The experiments consider four baselines $bl = (1.3, 2.3, 3.3, 4.3)$ m between the transmitter and the receiver, the communication channel 5 and 9, and two transmission power levels 28.6 dBm/MHz and 24.6 dBm/MHz, while various motion patterns are considered, as depicted in Figure 2.24-(a). The experiments presented in Figure 2.25 report the results obtained from conducting experiments with channel 9 using both transmission power levels and two different baselines while performing a "Z"-shaped pattern. Based on these preliminary results shown in Figure 2.25, the choice of the baseline impacts the target distance estimation. Note that for smaller baseline values, the distance estimation significantly deteriorates. We have determined the optimal baseline for our experimental setup through these experiments. This baseline will serve as the reference for comparing and evaluating the performance with channel 5, now. The evaluation is done in a structured indoor environment by using 8 Qualisys Arqus A9 high-performance cameras[8]. Figure 2.26-(a) illustrates the comparison between the UWB and MoCap traces, while Figure 2.26-(b) displays the histogram representing the error. Note that the point tracked with motion capture does not align with the virtual point tracked by the UWB radar (i.e., the human body). Consequently, this discrepancy introduces a systematic error in the evaluation, which can be quantified to be approximately 10 cm. For the remaining experiments, raw traces are depicted to provide a comprehensive overview of the experiment's dynamics. A qualitative comparison confirms the improved estimation on channel 9, showing a more stable signal. Channel 5 produces the worst outcomes compared to channel 9, primarily because channel 9 is less susceptible to RF noise in the indoor environment (e.g., WiFi), owing to its higher center frequency. Better results are achieved when the default power transmission (i.e., 24.6 dBm/MHz)

[8] `https://t.ly/kPI_7`

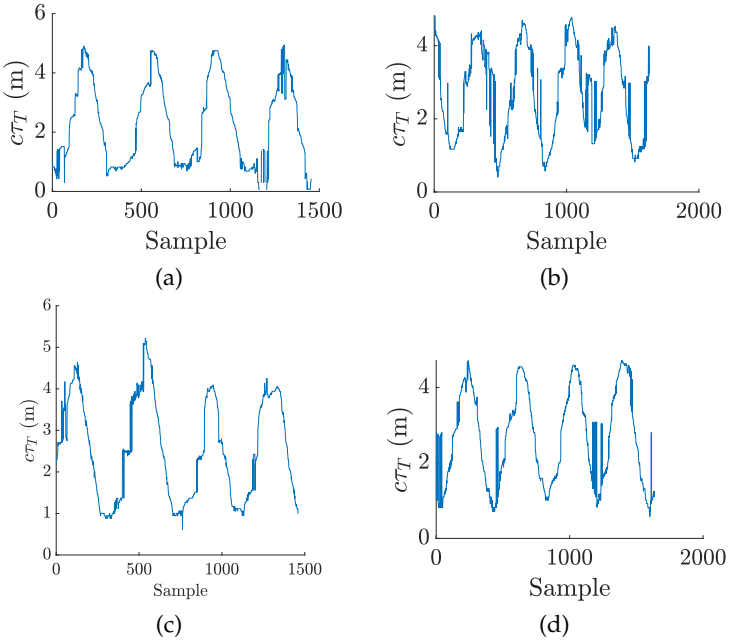

FIGURE 2.25: Bistatic radar for the "Z" shaped motion pattern of Figure 2.24-(a) with channel 9. (a,c) baseline 2.3 m, (b,d) baseline 4.3 m. (a,b) Tx power level 28.6 dBm/MHz, (c,d) low Tx power level 24.6 dBm/MHz.

is utilized. The increase in transmission power amplifies the amplitude of the noise, leading to more significant fluctuations in the estimated τ_T value. It is important to note that these fluctuations are not solely caused by the estimator but also arise from the variability in timestamping due to internal circuitry sources and the outcome of the leading edge algorithm. Finally, the weighting function (2.30) greatly enhances the stability and reliability of target distance estimation as compared to our previous work [126] (see Figure 2.27).

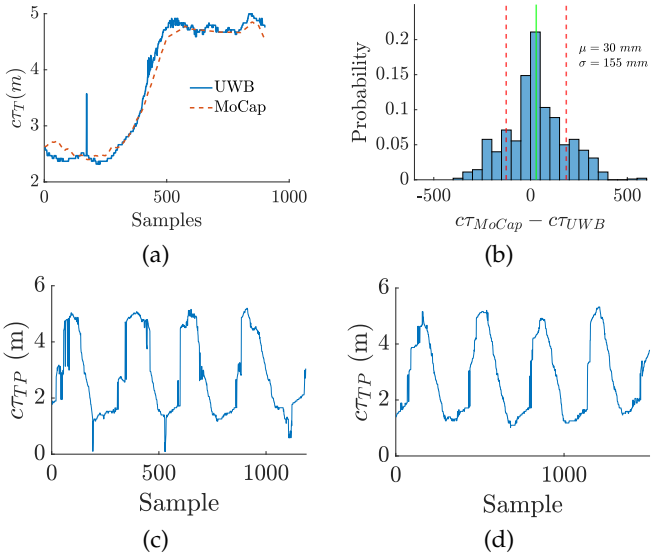

FIGURE 2.26: (a,b) Channel 9 and baseline 4.3 m Square motion pattern of Figure 2.24-(a): (a) comparison between MoCap and UWB; (b) Histogram of the error. (c,d) UWB radar traces (collected simultaneously) with baseline 2.3 m and back and forth motion pattern of Figure 2.24-(a): (c) channel 5 (d) channel 9, power transmission level 24.6 dBm/MHz.

2.5 Overcoming Scalability Hurdles: UWB-based Indoor Positioning System with Infinite Scalability

This section introduces the DTDoA ranging technique proposed in [66], which addresses both accuracy and scalability issues in current localization methods. Scalability is identified as a significant challenge in various multi-agent environments, such as smart cities and Industry 4.0, due to limitations in UWB systems where each subject must complete its localization before others can start. The proposed technique offers a constant update rate for positioning services, theoretically scalable to track an infinite number of assets while maintaining an error range of 20 cm at worst. Validation against MoCap movement data confirms the accuracy of the UWB positioning infrastructure. In particular, the main contributions of this section are:

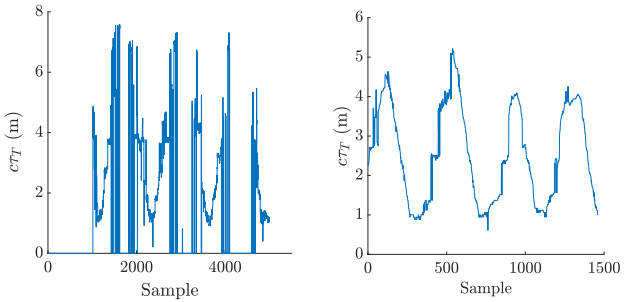

FIGURE 2.27: In (a), the estimated distance using the standard windowing approach on the old generation of UWB devices using channel 5. In (b), the new UWB generation devices using channel 9. Transmission power 24.6 dBm/MHz and baseline 2.3 m

- We revised the models presented in [66], and we validated the model experimentally with a ground truth provided by optical tracking MOCAP system [127]. Furthermore, we developed a testbed using the sync unit [127] and a wired connection with the UWB receiver.
- We analysed the effect of the tag motion on the positioning and the effect of additional distortions generated by a harsh environment like in our laboratory (small gantry crane, pvc panels).
- We evaluate the performance of the proposed system in both dominant and complete Non-Line-of-Sight (NLoS) conditions, evaluating how the proposed system works in more realistic and complex scenarios.

2.5.1 Measurement models

The Local Positioning System (LPS), detailed in [66], considers an environment with a master UWB, a set of n anchors $\mathbf{a}_i$ and a tag. We can thus denote t as the actual, ideal time and with τ the time measurement from either the master $\tau^m(t)$; the i-th anchor $\mathbf{a}_i$ as $\tau^i(t)$; or the tag $\tau(t)$. Since we do not have an external time reference, we can assume that the time measurements of the master are the reference signal for the UWB positioning

algorithm, following the simplified clock model presented in [66], i.e.

$$\tau^{m\star}(t) = o_m + \nu_m t + \eta_m(t) = \tau^m(t) + \eta_m(t), \tag{2.31}$$

where we use the superscript $\cdot^\star$ to denote each measurement result. o_m is the time offset of the master, $\nu_m = \frac{\overline{f}_m(t)}{f_m}$ the normalised clock rate with respect to the ideal time (i.e., the ratio between the instantaneous frequency of the local oscillator $\overline{f}_m(t)$ and the corresponding nominal value f_m, usually on the order of some part per million (ppm) [128]) and we implicitly assume that the measurement uncertainty $\eta_m(t)$ is a random variable generated by a white, stationary and zero mean process with variance $\sigma^2_{\eta_m}$. Notice that the main source of uncertainties – neglecting the effects of ageing or the drift changes induced by harsh environmental conditions (e.g., mechanical vibrations or temperature effects [128]) – is related to timestamping operations accuracy. Albeit those effects can be mitigated by implementing double consecutive message transmissions, the effect cannot be entirely removed. Similarly, for the i-th anchor $\mathbf{a}_i$ we have

$$\tau^{i\star}(t) = o_i + \nu_i t + \eta_i(t) = \tau^i(t) + \eta_i(t), \tag{2.32}$$

where o_i and ν_i are the i-th offset and clock rate of the time of the anchors with respect to the ideal time, while $\eta_i(t) \sim \mathcal{N}(0, \sigma^2_{\eta_i})$ and white as before. Finally, for the tag time measurements, we have

$$\tau^\star(t) = o + \nu t + \eta(t) = \tau(t) + \eta(t), \tag{2.33}$$

where the quantities have the same meaning as in the previous two cases.

Anchors clock analysis The main idea underlying this approach is that no message exchange should be carried out from the tag to the anchors, but only from the anchors to the tag, thus ensuring infinite scalability in terms of trackable number of tags. In the ideal case, the quantities o_i, ν_i (with $i = 1, \ldots, n$) in (2.32) with respect to the master reference time are retrieved through the following synchronisation algorithm: starting at a generic time $\bar{t}$, the master anchor sends two messages $\tau^m(\bar{t})$ and $\tau^m(\bar{t} + \Delta_{i,m})$ to $\mathbf{a}_i$, whose timestamps at the receiving side are $\tau^i(\bar{t} + \delta_{i,m})$ and

$\tau^i(\bar{t} + \Delta_{i,m} + \delta_{i,m})$, where $\delta_{i,m}$ is the Time of Flight (ToF) from the master to the anchor. By denoting with $[x_m, y_m]^T$ and $\mathbf{a}_i = [x_i, y_i]^T$ respectively the master and the anchor known Cartesian coordinates in the $X_w \times Y_w$ plane with respect to a fixed reference frame $\langle W \rangle = \{X_w, Y_w, Z_w\}$, it turns out that

$$\rho_{i,m} = \| [x_m, y_m]^T - \mathbf{a}_i \| = \sqrt{(x_m - x_i)^2 + (y_m - y_i)^2},$$

is the distance among the two anchors. Therefore, assuming that c is the known propagation speed of the radio frequency signal in LOS conditions, we have that the ideal ToF $\delta_{i,m}$ can be obtained as

$$\delta_{i,m} = \frac{\rho_{i,m}}{c}. \tag{2.34}$$

As a consequence, using (2.31) and (2.32) and defining $\overline{\nu}_{i,m} = \frac{\nu_i}{\nu_m}$, we can derive the first-order Taylor approximation for the relative clock rate

$$\overline{\nu}_{i,m}{}^\star = \frac{\tau^{i\star}(\bar{t} + \Delta_{i,m} + \delta_{i,m}) - \tau^{i\star}(\bar{t} + \delta_{i,m})}{\tau^{m\star}(\bar{t} + \Delta_{i,m}) - \tau^{m\star}(\bar{t})} \approx \overline{\nu}_{i,m} + \beta, \tag{2.35}$$

where the uncertainty mean $\mu_\beta = \mathrm{E}\{\beta\} = 0$ (the $\mathrm{E}\{\cdot\}$ is the usual expected operator), while its variance is

$$\mathrm{E}\left\{\beta^2\right\} = \sigma_\beta^2 = \frac{2}{\nu_m^2 \Delta_{i,m}^2}(\sigma_{\eta_i}^2 + \overline{\nu}_{i,m}^2 \sigma_{\eta_m}^2).$$

It can thus be argued that the larger the synchronisation interval $\Delta_{i,m}$, the smaller the uncertainty on the indirect measurement of $\overline{\nu}_{i,m}{}^\star$ (i.e., this is the effect of averaging on longer periods).

Similarly, by defining the actual relative offset as

$$\begin{aligned} \overline{o}_{i,m} &= \tau^i(\bar{t} + \delta_{i,m}) - \overline{\nu}_{i,m}\tau^m(\bar{t}) - \delta_{i,m} = \\ &= o_i - \overline{\nu}_{i,m} o_m - (1 - \nu_i)\delta_{i,m}, \end{aligned} \tag{2.36}$$

we have that

$$\overline{o}_{i,m}{}^\star(\bar{t}) = \tau^{i\star}(\bar{t} + \delta_{i,m}) - \overline{\nu}_{i,m}{}^\star \tau^{m\star}(\bar{t}) - \delta_{i,m} \approx \overline{o}_{i,m} + \gamma(\bar{t}), \tag{2.37}$$

whose uncertainty has mean $\mu_\gamma(\bar{t}) = \mathrm{E}\left\{\gamma(\bar{t})\right\} = 0$ and variance

$$\sigma_\gamma^2(\bar{t}) = \mathrm{E}\left\{\gamma(\bar{t})^2\right\} = \left(1 - 2\frac{\tau^m(\bar{t})}{\nu_m \Delta_{i,m}}\right)\sigma_{\eta_i}^2 + \\ + \overline{v}_{i,m}^2\left(1 + 2\frac{\tau^m(\bar{t})}{\nu_m \Delta_{i,m}}\right)\sigma_{\eta_m}^2 + \tau^m(\bar{t})^2\sigma_\beta^2.$$

Applying (2.37) to the timestamp quantities delayed by $\Delta_{i,m}$, we have $\overline{o}_{i,m}{}^\star(\bar{t} + \Delta_{i,m})$. It is then possible to formulate a new estimate as

$$\hat{\overline{o}}_{i,m} = \frac{\overline{o}_{i,m}{}^\star(\bar{t}) + \overline{o}_{i,m}{}^\star(\bar{t} + \Delta_{i,m})}{2} = \overline{o}_{i,m} + \overline{\gamma}(\bar{t}), \tag{2.38}$$

that is now affected by a zero mean uncertainty with variance

$$\sigma_{\overline{\gamma}}^2(\bar{t}) = \frac{\sigma_{\eta_i}^2}{2} + \frac{\sigma_{\eta_m}^2}{2} + \tau^m\left(\bar{t} + \frac{\Delta_{i,m}}{2}\right)^2\sigma_\beta^2, \tag{2.39}$$

which may or may not be more useful than (2.37) depending on the value of $\Delta_{i,m}$. In fact, this is a direct consequence of the correlation between $\overline{o}_{i,m}{}^\star(\bar{t})$ and $\overline{o}_{i,m}{}^\star(\bar{t} + \Delta_{i,m})$ by means of $\overline{v}_{i,m}{}^\star$. In this case, the $\Delta_{i,m}$ should be chosen as small as possible. By assuming that the clock rates ν_m and ν_i are approximately constant between two synchronisation periods (usually executed every tens of seconds) and that the master and the anchors do not change their relative positions (i.e., the ToF $\delta_{i,m}$ is constant), the relative offset $\overline{o}_{i,m}$ is constant as well. With the previous quantities, we can convert the anchor time scale to the common master time-scale using again a first-order Taylor approximation to have

$$\frac{\tau^{i\star}(t) - \hat{\overline{o}}_{i,m}}{\overline{v}_{i,m}{}^\star} \approx \tau^m(t) + e_{i,m} + \varepsilon(t). \tag{2.40}$$

where $e_{i,m} = \frac{1-\nu_i}{\overline{v}_{i,m}}\delta_{i,m}$, $\mathrm{E}\left\{\varepsilon(t)\right\} = 0$ and

$$\sigma_\varepsilon^2(t) = \frac{\sigma_{\eta_i}^2}{\overline{v}_{i,m}^2} + \frac{\sigma_{\overline{\gamma}}^2(\bar{t})}{\overline{v}_{i,m}^2} + \\ + \left[\frac{(\tau^m(t) + e_{i,m})^2}{\overline{v}_{i,m}^2} - 2\frac{\tau^m(t) + e_{i,m}}{\overline{v}_{i,m}^2}\tau^m(\bar{t})\right]\sigma_\beta^2.$$

Tag clock analysis Due to the DTDoA approach used, also tag's clock have to be corrected. Let's consider the tag at time t be in position $\mathbf{p}(t) = [x(t), y(t)]^T$ in $\langle W \rangle$. By denoting with

$$\rho_i(t) = \|\mathbf{p}(t) - \mathbf{a}_i\| = \sqrt{(x(t) - x_i)^2 + (y(t) - y_i)^2},$$

the actual distance between the tag and the i-th anchor, we have that the ToF $\delta_i(t)$ is given by (2.34) when $\rho_{i,m}$ is substituted with $\rho_i(t)$. To perform the algorithm, the relative clock rate $\overline{\nu}_m = \frac{\nu}{\nu_m}$ between the tag and the master (i.e., the reference for all the anchors) is needed and it is computed using the relation (2.35) specialised for the tag. Therefore, two messages at time t_i and $t_i + \Delta_i$ are received by tag from the i-th anchor and containing the corrected anchor time (2.40). We first notice that the motion of the tag can induces a variability in the distance to the i-th anchor in the period Δ_i, which is expressed as

$$\rho_i(t_i + \Delta_i) = \|\mathbf{p}(t_i) + d_i(\Delta_i)\mathbf{u}_i(t_i) - \mathbf{a}_i\|,$$

where $d_i(\Delta_i)$ the tag displacement taking place at time t_i in the period Δ_i and $\mathbf{u}_i(t_i)$ it unit direction vector in the plane. An upper bound on the effect of $d_i(\Delta_i)$ can be found noticing that the maximum increase (or decrease) of the distance takes place when $\mathbf{u}_i(t_i) = [x(t) - x_i, y(t) - y_i]^T$, i.e., directed towards the anchor $\mathbf{a}_i$. Therefore the ToF (2.34) induced variation will be $\delta_i(t_i + \Delta_i) = \delta_i(t_i) + \alpha \frac{d_i(\Delta_i)}{c}$, where $\alpha \in [-1, 1]$ depends on the orientation of $\mathbf{u}_i(t_i)$ as explained before. Therefore, relative clock skew will be affected as well, which will be given by

$$\overline{\nu}_m = \frac{\nu}{\nu_m} \left(1 + \alpha \frac{d_i(\Delta_i)}{c\Delta_i}\right). \tag{2.41}$$

For what concerns the TDoA, the two timestamped messages are received by the tag at $\tau^\star(t_i + \delta_i(t_i))$ and $\tau^\star(t_i + \Delta_i + \delta_i(t_i + \Delta_i))$, both obviously

expressed in the tag time-scale. Therefore, using the relation (2.35), we have

$$\begin{aligned}&\frac{\tau^{\star}(t_i+\Delta_i+\delta_i(t_i+\Delta_i))-\tau^{\star}(t_i+\delta_i(t_i))}{\frac{\tau^{i^{\star}}(t_i+\Delta_i)-\hat{\delta}_{i,m}}{\overline{\nu}_{i,m}{}^{\star}}-\frac{\tau^{i^{\star}}(t_i)-\hat{\delta}_{i,m}}{\overline{\nu}_{i,m}{}^{\star}}}\approx\\&\approx\overline{\nu}_m+\xi(\Delta_i)=\overline{\nu}_m{}^{\star},\end{aligned}\tag{2.42}$$

with $\mathrm{E}\{\xi(\Delta_i)\}=0$ and

$$\sigma_{\xi}^2(\Delta_i)=\frac{2\overline{\nu}_m^2}{\nu_i^2\Delta_i^2}\sigma_{\eta_i}^2+\frac{2}{\nu_m^2\Delta_i^2}\sigma_{\eta}^2+\frac{\overline{\nu}_m^2}{\nu_{i,m}^2}\sigma_{\beta}^2.$$

Indoor GPS TDoA The UTDoA relies on an implicit event: all the anchors receive a tag's generated broadcast message that acts as an implicit synchronisation event. In the case of the proposed DTDoA with unbounded scalability, the messages are transmitted from anchors side to the tags side, hence a synchronisation event cannot be defined. Strictly speaking, if such a possibility would exist, the master and the anchors would send their packets simultaneously at time t_m. The tag would then measure the difference in reception times as $\tau(t_m+\delta_m(t_m))$ and $\tau(t_m+\delta_i(t_m))$ and, hence be able to compute the TDoA as

$$\begin{aligned}&c\left[\tau(t_m+\delta_i(t_m))-\tau(t_m+\delta_m(t_m))\right]=\\&=c\nu(\delta_i(t_m)-\delta_m(t_m))=\nu(\rho_i-\rho_m),\end{aligned}\tag{2.43}$$

$\forall i=1,\ldots,n$. Notice that such a measure is only affected by the relative clock rate ν, which is of course negligible since it generates an error in the order of some micrometers.

Since such a synchronised event cannot be generated, at time t_m a broadcast message is transmitted from the master, followed by a second message at time $t_m+\Delta_m$. The tag timestamps the messages at reception times, denoted as $\tau^{\star}(t_m+\delta_m(t_m))$ and $\tau^{\star}(t_m+\Delta_m+\delta_m(t_m+\Delta_m))$, and then stores the transmission timestamps $\tau^{m\star}(t_m)$ and $\tau^{m\star}(t_m+\Delta_m)$ encapsulated inside the broadcasted messages. The same mechanism is applied when the anchor i transmits at time t_i and $t_i+\Delta_i$, with tag's transmitted timestamps modified according to (2.40), which are then used by the tag to compute the

relative clock rate (2.42). The absence of a synchronisation event and the presence of the protocol time interval $\Delta_{i,m} = t_i - t_m$ generates the following protocol-induced uncertainty

$$\begin{aligned} g^\star(\Delta_{i,m}) &= \overline{\nu}_m{}^\star \left(\frac{\tau^{i\star}(t_i) - \hat{\overline{o}}_{i,m}}{\overline{\nu}_{i,m}{}^\star} - \tau^{m\star}(t_m) \right) \approx \\ &\approx \nu \Delta_{i,m} + \nu\alpha \frac{d_i(\Delta_{i,m})}{c} + \overline{\nu}_m e_{i,m} + \varphi(t_i, t_m) \\ &= g(\Delta_{i,m}) + \varphi(t_i, t_m). \end{aligned} \tag{2.44}$$

In this case $\mathrm{E}\{\varphi(t_i, t_m)\} = 0$ and

$$\begin{aligned} \sigma^2_\varphi(t_i, t_m) &= \overline{\nu}^2_m(\sigma^2_\varepsilon(t_i) + \sigma^2_{\nu_m}) + (\nu_m \Delta_{i,m} + e_{i,m})^2 \sigma^2_\xi(\Delta_i) + \\ &+ \frac{2\overline{\nu}^2_m}{\nu_m \Delta_i}(\nu_m \Delta_{i,m} + e_{i,m})(\sigma^2_\varepsilon(t_i) - \sigma_\varepsilon(t_i, t_i + \Delta_i)), \end{aligned} \tag{2.45}$$

where $\sigma_\varepsilon(t_i, t_i + \Delta_i)$ is the correlation between the uncertainties $\varepsilon(t_i)$ and $\varepsilon(t_i + \Delta_i)$, given by

$$\begin{aligned} \mathrm{E}\{\varepsilon(t_i)\varepsilon(t_i + \Delta_i)\} &= \frac{(\tau^m(t_i) + e_{i,m})(\tau^m(t_i + \Delta_i)}{\overline{\nu}^2_{i,m}} \sigma^2_\beta + \\ &+ \frac{\sigma^2_{\dot{\gamma}}(\bar{t})}{\overline{\nu}^2_{i,m}} - \frac{\tau^m(t_i) + \tau^m(t_i + \Delta_i) + 2e_{i,m}}{\overline{\nu}^2_{i,m}} \tau^m\left(\bar{t} + \frac{\Delta_{i,m}}{2}\right) \sigma^2_\beta. \end{aligned}$$

We are now ready to conclude the uncertainty analysis by computing the DTDoA relation (2.43) with measured quantities

$$\begin{aligned} &c\left[\tau^\star(t_i + \delta_i(t_i)) - \tau^\star(t_m + \delta_m(t_m)) - g^\star(\Delta_{i,m})\right] = \\ &= \nu(\rho_i - \rho_m) - c\overline{\nu}_m e_{i,m} + \lambda(t_i, t_m), \end{aligned} \tag{2.46}$$

resulting in an overall uncertainty with mean $\mathrm{E}\{\lambda(t_i, t_m)\} = 0$ and variance

$$\sigma^2_\lambda(t_i, t_m) = c^2 \left[2\left(1 + \frac{\nu_m \Delta_{i,m} + e_{i,m}}{\nu_m \Delta_i}\right) \sigma^2_\eta + \sigma^2_\varphi(t_i, t_m) \right]. \tag{2.47}$$

It is worthwhile to note that those quantities can be equivalently computed for the delayed messages, by considering $\tau^{m\star}(t_m + \Delta_m)$ and $\tau^{\star i}(t_i + \Delta_i)$

in (2.44), and $\tau^{\star}(t_m + \Delta_m + \delta_m(t_m + \Delta_m))$ and $\tau^{\star}(t_i + \Delta_i + \delta_i(t_i + \Delta_i))$ in (2.46). Of course, comparing (2.46) and (2.43), we can notice that the presence of multiple time sources (i.e., having n anchors) induces potential errors stemming from the synchronisation uncertainty with the master $\varepsilon(t)$, highlighted in (2.40), which is, unfortunately unavoidable.

2.5.2 Uncertainty Models Validation

The article [66] showed that the first-order approximation for (2.47) works remarkably well in simulation. We present here the experimental set-up and the detailed analysis towards experimental validation of the proposed models in an actual environment, also focusing on the detrimental effects of the target motion described in Section 2.5.1, thus deriving the practical relevance of the performed analysis.

Indoor testing environment The testing environment is depicted in Figure 2.28. The environment is equipped with a MoCap system for ground truth and a network of UWB anchors, described in what follows. It has to be noted that the laboratory in which the system has been tested is very challenging (see Figure 2.29), due to the presence of many artefacts generating additional sources of uncertainty on the LPS.

MoCap system To create a ground truth trajectory to evaluate the accuracy of the UWB positioning system, we have adopted a Motion Capture system, specifically a system provided by Qualisys with 8 Arqus A9 cameras, a sync unit, and the workstation for system configuration (see Figure 2.28). The cameras are configured to work at a frequency of 240 Hz to achieve a suitable frame rate with respect to the UWB data rate. The tag is equipped with a Hand Rigid Bodies Marker and tracked by the MoCap software, measuring its 3D position at each captured frame. After calibration, the system reports a sub-millimetre accuracy with less than 1 mm standard uncertainty [9].

[9]The adopted calibration procedure can be found here https://docs.qualisys.com/getting-started/content/getting_started/running_your _qualisys_system/calibrating_your_system/calibrating_your_system.html

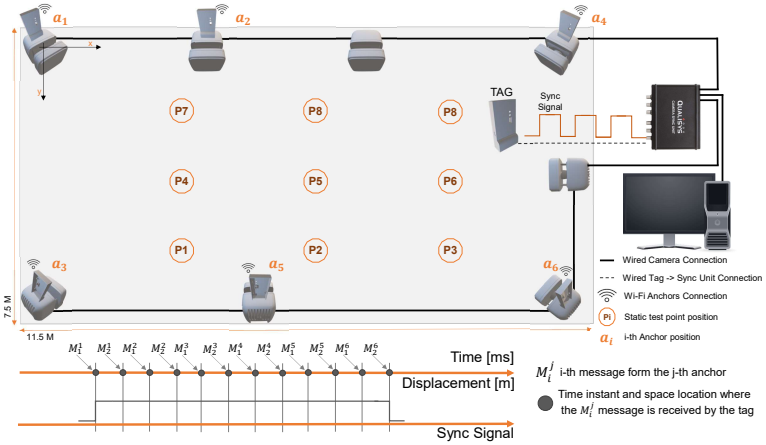

FIGURE 2.28: Indoor testing infrastructure. In the top, we show the MoCap cameras along with the UWB anchors and the acquisition chain. The bottom part depicts the effect of tag moving affecting reception's time instant and the spatial location of the 12 messages sent by the $n = 5$ reference anchors (the sixth is the master). Each message is received at a different time/space instant/location, causing the estimation shifting problem. The highlighted P_i locations show where the static tests were conducted.

UWB system To implement our LPS, we decided to use the commercial-off-the-shelf COTS) Decawave DWM1001[10] SoM, a customary choice for indoor positioning systems [129]. The DWM1001 is a compact module that integrates both a low-power nRF52832 MCU and the Decawave DW1000[11] UWB transceiver. It also integrates RF circuitry, a UWB antenna, and a motion sensor for sensor fusion applications [130].

The DW1000 chip is an IEEE 802.15.4-2011 [125] compliant UWB transceiver, which can operate on six different frequency bands with centre frequencies between 3.5 to 6.5 GHz and bandwidth of 500 or 900 MHz. It provides the possibility of ranging measurements and retrieving the measured CIR.

[10] https://www.decawave.com/sites/default/files/dwm1001_datasheet.pdf
[11] https://www.decawave.com/sites/default/files/resources/dw1000-datasheet-v2.09.pdf

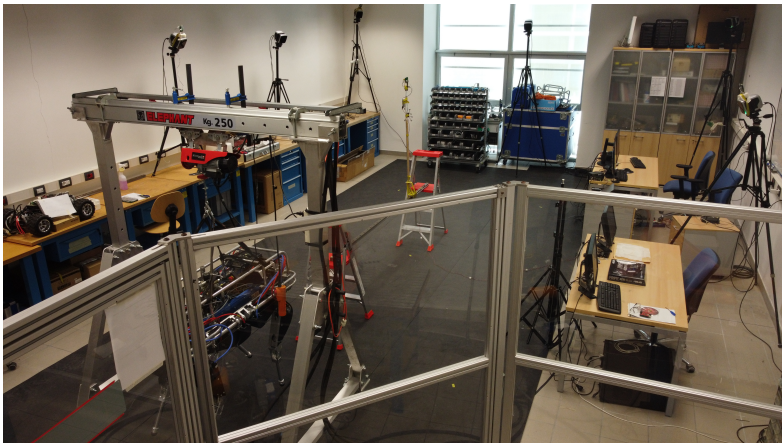

FIGURE 2.29: Laboratory environment. In particular, the quadruped and barrier for the anthropomorphic robotic arm created the conditions for the multi-path effect and NLoS condition, respectively.

The chip also offers three different data rates: 110 kbps, 850 kbps, and 6.8 Mbps. The DW1000 clocking scheme is based on three main circuits; crystal oscillator (trimmed in production to reduce the initial frequency error to approximately 3 ppm), Clock Phase-Locked Loop (PLL), and RF PLL. The on-chip oscillator is designed to operate at a frequency of 38.4 MHz. This clock is then used as the reference input to the two on-chip PLLs. The clock PLL generates a 63.8976 GHz reference clock required by the digital backend for signal processing. The RF PLL generates the clock for the receive and transmit chain. The DW1000 automatically timestamps transmitted and received frames with a precision of 40 bits. Working at a nominal 64 GHz resolution, packets are timestamped with a 15.65 ps event timing precision[12].

The DWM1001 SoM was configured, during the experimental tests, to use UWB Channel 5 (with a frequency of 6489.6 MHz and a bandwidth of 499.2 MHz) preamble length of 128 symbols, the highest Pulse Rate of 64 MHz and the highest Data Rate of 6.8 Mbps.

[12]https://www.decawave.com/dw1000/usermanual/

To implement the LPS method on UWB, a specific number of DWM1001 modules are programmed to act as anchors to provide a reference infrastructure for the tags. Hence, each anchor is interfaced with a Raspberry PI 3 and a DWM1001 module. Finally, data sharing and acquisition is implemented by leveraging the MQTT protocol to enable data transfer by a remote system. To create an infrastructure referenced by the motion capture, we have installed the UWB anchors on top of the MoCap cameras, while the MoCap sync unit is connected with a wired cable to one of the GPIO of the DWM1001's MCU of the tag for synchronisation of all the sensor readings. Indeed, the sync unit allows external recording events and matching them with the captured frames. Given the standard uncertainty of the MoCap system previously mentioned and the typical accuracy of the UWB positioning system (typically, in the order of some centimetres), we limit the uncertainty analysis to 1 mm of minimum resolution.

The infrastructure parameters for the algorithm are: $\Delta_{i,m} = 3$ ms, $\Delta_i = 1.1$ ms, $\rho_{i,m} = \{6.063, 11.230, 9.716, 7.484, 4.048\}$ m for the $n = 5$ anchors, $c = 299792458$ m/s.

Model validation Notice that, to validate the final DTDoA uncertainty (2.47), the compounding experimental quantities must be retrieved, which are impossible to be gathered from any measurement system. Therefore, we adopt a mixture of simplifications and nominal values to validate the equation. The results presented in this section refer to the static case, i.e., where $\alpha = 0$ in (2.41) and (2.44). We first analyse the synchronisation period $\Delta_{i,m}$ influence, as mentioned in Section 2.5.1,Anchors clock analysis. Indeed, there is a linear dependency between the offset estimation error $\tilde{o}_{i,m} = \hat{o}_{i,m} - o_{i,m}$ and $\Delta_{i,m}$, which is empirically evaluated to be $\tilde{o}_{i,m} \approx 8 \cdot 10^{-6} \Delta_{i,m}$ (e.g., for $\Delta_{i,m} = 10$ ms, $\tilde{o}_{i,m} = 80$ ns). Similarly, increasing the anchors transmission delay $\Delta_{i+1,m} - \Delta_{i,m}$ of some milliseconds, the relative clock rate estimation error $\hat{\nu}_{i,m} - \nu_{i,m}$ increases of some ppm. We then recall that the reference time for our platform is given by the master clock, hence we assume for the model (2.31) that $\nu_m = 1$, so as that (2.44)

TABLE 2.8: Experimental standard uncertainty $\overline{\sigma}_\lambda(t_i, t_m)$ collected from the positions reported in Figure 2.28. All the quantities are expressed in millimetres and should be compared with the model-based value of the standard uncertainty $\sigma_\lambda(t_i, t_m)$. Results are the same for all the testing positions P_1, P_2, ..., P_9 in Figure 2.28.

Anchors	1	2	3	4	5
$\overline{\sigma}_\lambda(t_i, t_m)$	97	125	147	167	184
$\sigma_\lambda(t_i, t_m)$	72	93	110	124	137

turns to

$$g^\star(\Delta_{i,m}) = (\nu + \xi(\Delta_i)) \left(\frac{\tau^{i\star}(t_i) - \hat{\overline{o}}_{i,m}}{(\nu_i + \beta)} - \tau^{m\star}(t_m) \right) \approx$$
$$\approx \nu(\Delta_{i,m} + e_{i,m}) + \varphi(t_i, t_m).$$

Moreover, considering the standard uncertainty of the DWM1001's clock of 10 ppm [131], we assume that $\sigma_{\eta_m} = \sigma_{\eta_i} = \sigma_\eta = 0.45$ ns for all the uncertainty sources in (2.31), (2.32) and (2.33). Given these rated uncertainties and the fact that the involved time intervals $\Delta_{i,m}$ and Δ_i are in the order of few milliseconds, we can safely assume for the sake of validation that $\nu \approx 1$, thus (2.47) turns to

$$\sigma^2_\lambda(t_i, t_m) = \\ c^2 \left[2 \left(1 + \frac{\frac{\tau^{i\star}(t_i) - \hat{\overline{o}}_{i,m}}{\nu_i} - \tau^{m\star}(t_m)}{\Delta_i} \right) \sigma^2_\eta + \sigma^2_\varphi(t_i, t_m) \right]. \tag{2.48}$$

The only missing ingredient is $\sigma^2_\varphi(t_i, t_m)$ in (2.45), which is experimentally retrieved by directly computing the variance of (2.44), i.e., of the measured quantities $\frac{\tau^{i\star}(t_i) - \hat{\overline{o}}_{i,m}}{\overline{\nu}_{i,m}^\star} - \tau^{m\star}(t_m)$. Hence, with the described approach, we had the theoretical standard uncertainty $\sigma_\lambda(t_i, t_m)$ reported in Table 2.8. This value is then compared with the experimental standard uncertainty $\overline{\sigma}_\lambda(t_i, t_m)$ retrieved from the MoCap described in Section 2.5.2 and considering 5000 UWB samples from each position (see Table 2.8). In both cases, the standard uncertainties are independent from the testing positions $P_1, \ldots, P_9$ depicted in Figure 2.28, while the terms governing the equations are $\Delta_{i,m}$, σ^2_η and $\sigma^2_\varphi(t_i, t_m)$. Notice that the theoretical overall DTDoA uncertainty

TABLE 2.9: Comparison between the theoretical nonlinear value (2.48) and the CRLB. All the quantities are expressed in mm^2.

Anchor	1	2	3	4	5
Nonlinear (2.48)	3	10	21	37	55
CRLB	1	3	7	12	18

model (2.47) approaches remarkably well the results obtained in the field. Moreover, the synchronisation algorithm among the infrastructure nodes makes the proposed solution rather flexible and allows new receivers to join the network without any particular calibration procedure or reset of the infrastructure, which partially induces a part of the uncertainties subsumed in the statistical analysis of Table 2.8.

To further substantiate the analysis, we first experimentally verified that the DTDoA measurements actually follow a biased Gaussian distribution, with a bias that is mainly induced by non line of sight conditions and delays in the message timestamp processing times. Then we carried out a Cramer-Rao Lower Bound (CRLB) analysis as reported in [132] to be compared to the nonlinear (i.e., without first-order approximations) version of (2.48), both reported in Table 2.9. As can be seen, the analysis carried out is a good approximation of the actual CRLB, thus further validating the proposed analysis. Notice that the uncertainty is a function of the anchor position, thus showing a perfect match with the importance of anchor deployment geometry [3]. Moreover, as mentioned in Section 2.5.1, $\Delta_{i,m}$ should be chosen as small as possible to limit the uncertainty: from Table 2.9, it is evident a quadratic dependency for both the CRLB and the nonlinear (2.48) (indeed, $\Delta_{i,m} < \Delta_{i+1,m}$ as aforementioned), which, instead, is lost for the first order linearised values in Table 2.8. Nevertheless, by comparing the standard deviations in Table 2.8 and the variances in Table 2.9, it turns out that (2.47) is a good approximation of the nonlinear version of (2.48) despite the first-order approximations adopted, and thus can be considered as a nice figure of merit for the proposed solution.

Effect of a moving tag We now investigate the effects of the tag motion, thus $\alpha \neq 0$ and unknown in (2.41) and (2.44). The main effect is dictated,

once again, by the absence of a synchronisation event for the infrastructure, hence when the tag starts to move, the anchor timestamped values are acquired at different locations as shown at the bottom of Figure 2.28: the position signed as M_i^j stand for the i-th message ($i = 1, 2$) form the j-th anchor ($j = 2, \ldots, 5$, being $j = 1$ the master). Therefore, it is not defined as a unique position from the MoCap to act as the ground truth. Therefore, we decided to compare the DTDoA estimated values with three sample points: with reference to Figure 2.28, the first position M_1^1, the average position $\overline{M} = \frac{1}{2(n+1)} \sum_{j=1}^{5} M_1^j + M_2^j$ and the last position M_2^6. To synchronise the tag and the MoCap, we used the wired connection described in Section 2.5.2 and, in particular, we raised the GPIO of the DWM1001's MCU at M_1^1 and lowered at M_2^6, thus defining the UWB positioning cycle. It is worth to be noted that since $\Delta_i = 1.1$ ms and the sync unit maximum event capture rate is equal to 200 Hz, it was not possible to capture all the intermediate positions in the middle of the positioning cycle. To circumvent this limitation, the experimental setup comprised two support to hold a prismatic guide on which a vertical bar is mounted on the carriage. The experiment is performed over a distance of 3 m and moving the carriage linearly at a constant speed of about 1 m/s (e.g., an average walking speed of a human being) and only the first M_1^1 and last M_2^6 position of each positioning cycle were actually stored (see the bottom of Figure 2.28): with this setup, the average positions were computed correctly as well.

Nevertheless, such drawback makes the analysis of $\sigma_\lambda^2(t_i, t_m)$ in (2.47) carried out previously hard to be pursued. Therefore, we decided to consider the effect of the motion of the tag on the standard uncertainty of the estimated position. To this end, we adopted the standard Least Squares (LS) solution that can be found in [133]. Hence, the mean error on the X_w and Y_w axes computed on 5000 position cycles are reported in Table 2.10. It is evident how the tag's motion induces a constant bias, which is a consequence of the linear motion of the tag generating the effect described in Section 2.5.1, no matter the adopted ground truth reference and that the UWB positioning system underestimates the tag position. We also report in Figure 2.30 the probability mass function of the positioning error for the moving tag. Since the standard uncertainties, in this case, are $\sigma_x = 67$ mm

TABLE 2.10: Mean error of the UWB position estimates on 5000 position cycles for a linearly moving tag with respect to the three ground truth references. All the quantities are reported in millimetres.

	M_1^1	$\overline{M}$	M_2^6
μ_x	-93	-93	-94
μ_y	-173	-174	-173

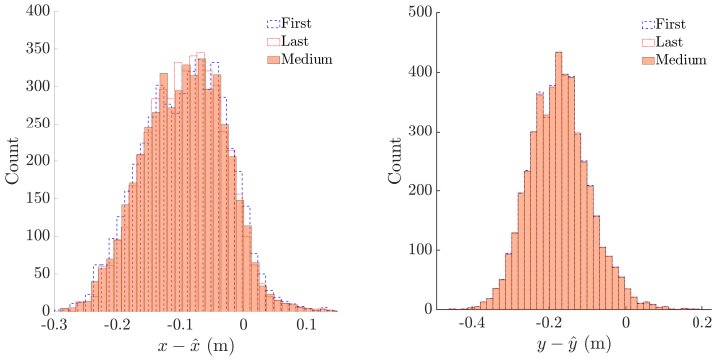

FIGURE 2.30: Histogram of the error for the dynamic test along the X_w (a) and Y_w (b) reference axes over 5000 repeated measurements.

and $\sigma_y = 78$ mm along the X_w and Y_w reference axes, they are comparable to standard deviations of the positioning experiments in Section 2.5.2, hence implying that the effect of the tag motion, for the typical human being velocity, is negligible in (2.47). It has to be noted that the proposed indoor positioning system is conceived for pedestrians or objects moving inside indoor environments. While such environments make the restriction to 2D scenarios quite natural, they also impose potential constraints once 3D problems are considered, since the anchor deployment is typically restricted by the presence of furniture or production machinery. As such, the anchors are most often placed at similar heights, thus increasing the uncertainty on the third dimension (i.e., Vertical Dilution of Precision (VDoP) issue [134]). In robotic systems, like Unmanned Aerial Vehicles (UAVs), where the z-coordinate plays a crucial role in navigation, obtaining

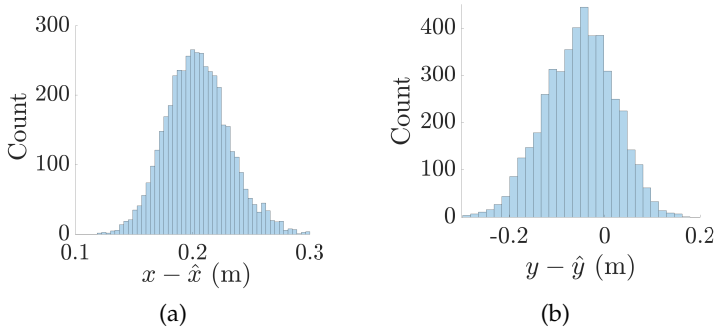

FIGURE 2.31: Distribution of the error in the static positions of Figure 2.28 along the X_w (a) and Y_w (b) over 5000 repeated measurements.

accurate altitude information is paramount. To this end, additional sensors such as barometers, ultrasonic sensors, Time-of-Flight (ToF) sensors, and LIDAR can be integrated into the system. The data from these sensors can then be fused to produce a more precise position estimation. An ad-hoc anchor deployment to account for this additional issue for 3D problems is a challenging research problem per se, thus left for future investigations.

Positioning Results We now present the results on the position of the tag that can be attained by the proposed solution by applying the mentioned multilateration solution for the TDoA. As a first comment, the validation analysis in Section 2.5.2 shows clearly that the standard LS solution can be adopted to solve the multilateration problem of the DTDoA, being a Weighted LS useless (i.e., the $\sigma^2_\lambda(t_i, t_m)$ in (2.47) is the same for all the anchors).

To evaluate the accuracy of the proposed system, we collected 5000 samples of a static tag in the positions P_i reported in Figure 2.28 and with the same choice of the parameters reported in Section 2.5.2. Figure 2.31 shows the empirical probability mass function of the positioning error with respect to the ground truth of the MoCap system. Despite the closeness to a Gaussian-shaped curve obtained (which has been correctly assumed

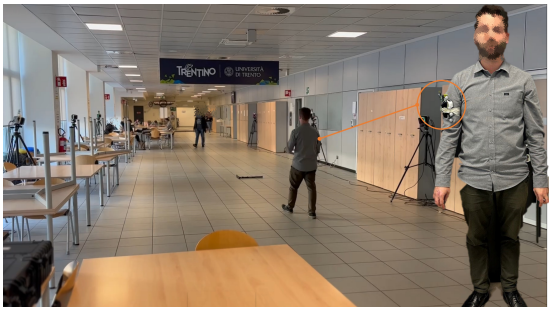

FIGURE 2.32: Experimental setup inside the hall of the "Dipartimento Ingegneria Industriale" of the University of Trento. Inside the orange circle the receiver mounting point on the tester arm.

throughout the analysis of Section 2.5.2), the distribution presents a bias induced by the previously mentioned angle-dependent UWB pulse distortion and path overlaps [135]. Moreover, the measure is also subjected to the anchors deployment geometry in the testing room that may cause reflections due to the presence of metallic objects (see Figure 2.29). In particular, the bias is quantifiable in $\mu_x = 203$ mm and $\mu_y = -49$ mm for the X_w and Y_w axes, respectively, while the standard uncertainty is $\sigma_x = 27$ mm and $\sigma_y = 69$ mm. To summarise, also considering the dynamic conditions reported in Figure 2.30, we can claim a positioning error that is below 30 cm, specifically a 2σ of 156 mm, and with an arbitrary number of positioned tags. To further assess the proposed system, we test the proposed solution in a larger area, as shown in Figure 2.32. Both static and dynamic tests are reported to assess the performance of the system in a natural scenario. In Figure 2.33, both the positions of the UWB anchors and the static tested points are reported, while Table 2.11 shows the mean error and the standard deviation in those static locations. In the same area, the dynamic tests are instead organised adopting two challenging paths: 8-shaped and Z-shape patterns, whose actual and estimated trajectories are reported in Figure 2.34. The result of the dynamic tests are reported in Table 2.12. The results of these experimental tests confirm how the environment affects performance: the mean error is indeed smaller than the one observed in Figure 2.30 due to the favourable environmental conditions for the initial wireless

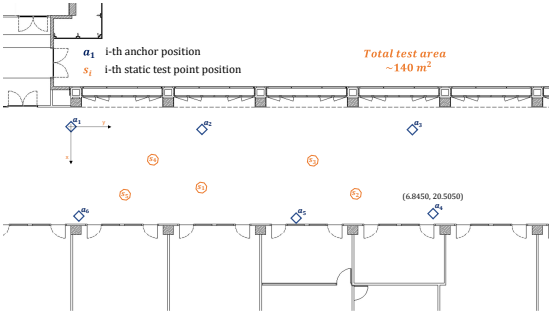

FIGURE 2.33: Graphical representation of the experimental setup, with the static testing point reported.

TABLE 2.11: Mean error $\{\mu_x, \mu_y\}$ and standard deviation $\{\sigma_x, \sigma_y\}$ along the X and Y axis, respectively, and computed in the five locations of Figure 2.33. All the quantities are expressed in millimetres.

Test Point	μ_x	μ_y	σ_x	σ_y
s_1	7	-56	119	82
s_2	50	-91	141	128
s_3	98	-92	166	111
s_4	131	-84	174	115
s_5	170	59	242	196

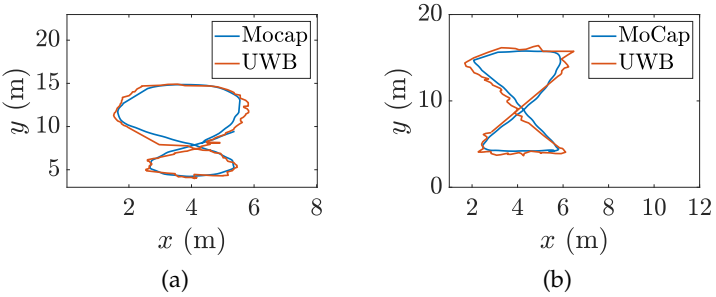

FIGURE 2.34: Dynamic test trajectories: 8-shape pattern (a) and Z-shape pattern (b). The trajectories are executed by the tester in the area depicted in Figure 2.32.

TABLE 2.12: Mean error $\{\mu_x, \mu_y\}$ and standard deviation $\{\sigma_x, \sigma_y\}$ for the dynamic tests of Figure 2.34. All the quantities are expressed in millimetres.

Pattern	μ_x	μ_y	σ_x	σ_y
Z-shape	45	8	207	201
8-shape	29	36	238	245

synchronisation and despite the more challenging trajectories adopted (in Figure 2.34-(b) it is possible to appreciate the antenna pattern effect at the sharp turns). The standard deviation, instead, is considerably increased due to the arm-mounted receiver position (See Figure 2.32), generating several NLoS conditions. We finally analyse the effect on the choice of the positioning cycle length. Indeed, at a first glance, making Δ_i large may have a positive effect on $\sigma^2_\lambda(t_i, t_m)$ in (2.47) (and, hence, on the positioning accuracy). However, $\Delta_{i,m}$ enters several times in the computation of the final uncertainties: for instance, the large is Δ_i, the more will be the synchronisation uncertainty due to the incorrect clock tag drift ν (2.33). We propose here empirical proof using the resulting positioning uncertainties as a figure of merit. Let us recall that $\Delta_{i,m} = 3$ ms, hence having $n = 5$ anchors (the first is the master), this corresponds to a positioning cycle of 15 ms. By setting $\Delta_{i,m} = 16$ ms, we obtain the empirical probability mass function in Figure 2.35 for the positioning error over 5000 repetitions. It can be immediately noticed how the effect of the not modelled nuisances becomes remarkable, generating quite long tails in the distribution. Moreover, we have $\mu_x = 288$ mm (with $\sigma_x = 797$ mm) and $\mu_y = -323$ mm (with $\sigma_y = 1.01$ m), i.e., highly noticeable detrimental effects. This is also reflected in the experimental value of (2.47), which turns to $\sigma_\lambda(t_i, t_m) = 279$ mm. Therefore, the longer is $\Delta_{i,m}$, the worse is the positioning accuracy, which verifies the hypothesis in [136].

Validation in challenging scenarios To further experimentally validate the proposed positioning system, we report here tests under different scenarios, including those with dominant NLoS conditions as well as under completely NLoS conditions. The experimental setup arena is the hall of our department shown in Figure 2.36. The area comprises obstacles

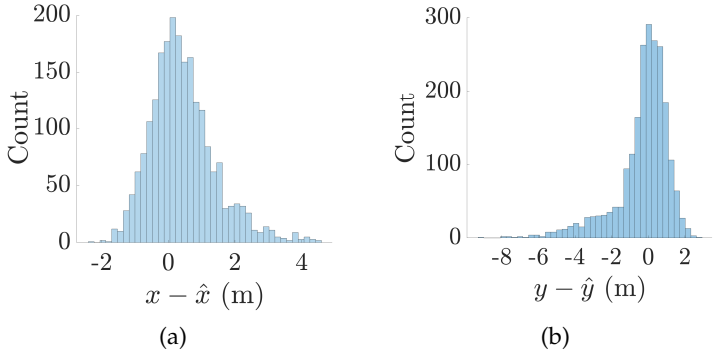

FIGURE 2.35: Distribution of the error in the static positions of Figure 2.28 along the X_w (a) and Y_w (b) over 5000 repeated measurements and with $\Delta_{i,m} = 16$ ms.

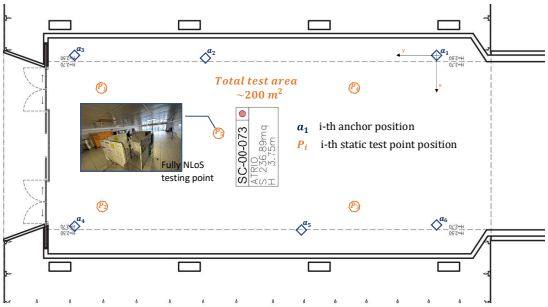

FIGURE 2.36: Graphical representation of the experimental setup, with the static testing point reported.

and vending machines, while the experiments have being conducted in a working day populated with many students. The system was firstly tested at static points $[P_1, P_2, P_3, P_4, P_5]$ selected to cover an area from the infrastructure boundary, where the positioning performance is known to be reduced due to the Position Dilution of Precision (PDoP) [134] value, to the center of the area. Metal bulletin boards were intentionally placed

TABLE 2.13: Mean error $\{\mu_x, \mu_y\}$ and standard deviation $\{\sigma_x, \sigma_y\}$ along the X and Y axis, respectively, and computed in P_5 of Figure 2.36. All the quantities are expressed in millimetres.

Test Point	μ_x	μ_y	σ_x	σ_y
P_5	210	-270	125	245

in the middle to introduce dominant NLoS conditions during the tests at points $[P_1, P_2, P_3, P_4]$, obstructing the propagation of the UWB signal with at least three anchors. The experiment resulted in a maximum of 30 cm of uncertainty, consistent with the previously reported results. The point $P5$ was tested under fully NLoS conditions by creating a barrier using the metal bulletin boards, resulting in worse performance compared to the results obtained for the testing point s_1 of Figure 2.36 that present a similar spatially relationship with the anchors. The results of this experiment are reported in Table 2.13. We additionally consider dynamic tests in the same scenario. Unfortunately, since NLoS conditions are present, the motion capture system was not available (indeed, it works only when Line-of-Sight conditions hold). Therefore, we used fiducial points to walk through. The results obtained from this approach, albeit qualitative due to the explained shortcomings, are shown in Figure 2.37, demonstrating once more the effectiveness of the proposed solution in dynamic and natural populated environments.

2.6 INFALLIBLE: Positioning Systems Enhancing Human Welfare

This section provides a brief overview of the awarded grant and highlights the ongoing advancements in positioning systems research, showcasing its significance as a constantly evolving field. The research conducted in indoor positioning systems for humans has provided a tangible solution for fostering coexistence between humans and wild animals in shared spaces, leveraging previously proposed strategies. The project submitted to the prestigious *10th Fondazione VRT Mountain Innovators Grant*, which emerged as the grant recipient, is geared towards addressing the growing concern

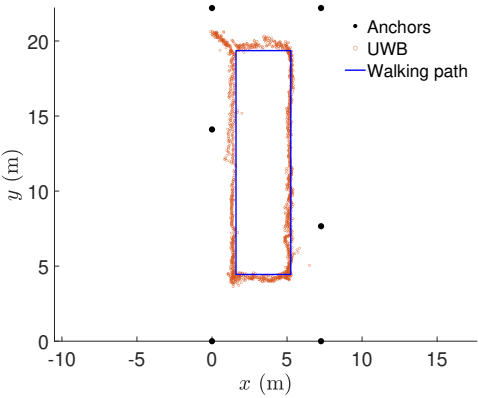

FIGURE 2.37: Dynamic test trajectory. The tester walks along a predefined path.

of heightened human activity in areas inhabited by potentially dangerous wildlife in recent times.

This phenomenon occurs in certain mountainous regions and/or at specific times of the year due to tourism. Moreover, the population's lifestyle changes have led to a rise in outdoor activities. Additionally, residents of mountainous areas spend a significant amount of time in these zones, engaging in activities such as grazing, wood collection, haymaking, litter collection, and hunting.

Among the animals considered potentially dangerous to human life in our territories are bears, wolves, and lynxes. Bears have always been present in the western Trentino territories, and in recent years, there has been a process of spontaneous recolonization by bears, as well as involvement by wolves and lynxes. The estimated total population of bears, based on the latest official data from 2019, is 82-93 individuals, with population trends illustrated in Figure 2.38. The INFALLIBLE project, accessible at `https://www.fondazionevrt.it/mountaininnovatos2023`, seeks to respond to the challenges posed by the resurgence of animals, notably bears, in regions increasingly frequented by humans for both work and leisure activities. It

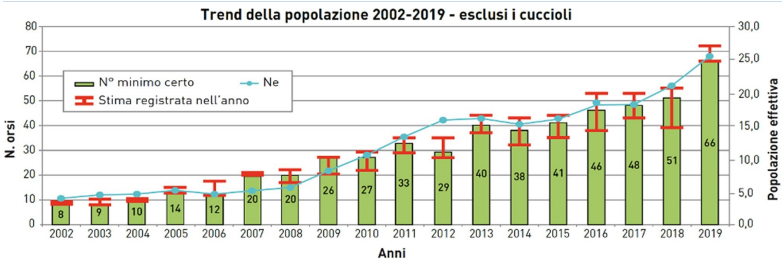

FIGURE 2.38: Bear Population Trend

endeavors to establish a cooperative and distributed localization network encompassing both humans and animals, thereby eliminating the necessity for deploying extensive infrastructure solely for bear localization across the territory. Presently, the province of Trento employs radio collars to track bear movements; however, this method often proves ineffective due to unreliable GPS signals or poor position information as outlined in the previous chapter. A cooperative positioning network renders the current GPS framework obsolete, offering the following advantages:

- No service interruption due to GPS signal gaps
- No need for a dedicated server and data coverage to access information for users directly involved
- A distributed system provides a level of robustness and flexibility unattainable with traditional centralized systems, reusable for any area and number of users without modification
- Strategic fiducial points within the area offer global information on positioning

The strategies implemented in this project are detailed in the preceding sections. For a more comprehensive understanding, please visit the dedicated webpage at `https://www.youtube.com/@fondazionevrt8859`.

Chapter 3

Robot-Centric Positioning Systems: Enhancing Spatial Awareness and Navigation

In this chapter, we delve into the realm of positioning systems designed for robotic applications. Building upon the algorithms and fundamental techniques discussed in the previous chapter, we specifically focus on exploring the utilization of Unmanned Aerial Vehicles (UAVs) as transformative robotic platforms for diverse applications.

UAVs have transitioned from specialized tools to commonplace devices, making their way into both households and industrial installations. Concurrently, the spectrum of their applications continues to expand. Researchers have directed their attention towards investigating various application challenges, including autonomous navigation [137], obstacle avoidance [138], goods transportation [139, 140], logistics management [141], and precision agriculture [142].

In recent years, UAV control techniques have progressed steadily, and one of the still most investigated topics tackle the localisation and positioning problem. In the classical approach, UAVs obtain their position, and eventually the one of a target, exploiting the Global Positioning System (GPS). This approach, however, is not always reliable or available as in the case of GPS-denied environments [143], such as airports, alleys, parking lots and

underground locations, where satellite signals and other technologies lack precision or fail entirely.

To solve this problem, researchers have proposed different positioning and localisation technologies. These solutions can be categorised into 3 main families: *Vision based*, like Visual-Inertial Navigation, Infrared and/or Lidar; *Radio Frequency based*, such as Ultra-Wide Band (UWB), Bluetooth and Radio Frequency IDentification; *Audio signal based*, exploiting Ultrasound technologies [144–147]. Among all the listed solutions, UWB presents some unique characteristics like low-cost, low latency, low energy consumption, and centimeter-level accuracy that have attracted researchers' interest lately [148, 149]. Moreover, unlike vision-based technologies, the RF will never suffer from the low-visibility condition and does not require costly infrastructures or computationally hungry processing algorithms. Therefore, fuelled by recent advancements in the development of localisation infrastructures based on UWB [66, 150], researchers have investigated the application of such technologies in robotics [67, 100], even for multi-agent formation control [151]. For instance, in [152], a combination of UWB ranging with GPS way pointing is adopted to achieve cooperative flight for cooperative goods transportation. In [153], a swarm of miniature, fully autonomous flying robots capable of exploring unknown environments autonomously while satisfying various requirements, including flight efficiency, obstacle avoidance, inter-robot collision avoidance, and swarm coordination has been presented.

As the number of personal UAVs is constantly growing, it becomes important to study the interaction between humans and such systems [154, 155]. Currently, most of the research is devoted to the evaluation and the development of new control modalities to enhance human-drone interaction and extend the set of possible use cases [156, 157]. However, the need for complex hardware interfaces, such as joysticks or haptic devices along with visual/auditory control as voice recognition or the interpretation of face poses and body postures, limits the possible use cases and the wide spread application of UAVs in service robotics scenarios [158].

As the demand for robots continues to rise, there is a parallel escalation in

the necessity for robust positioning infrastructure. Specifically, in applications such as the exploration of unknown environments, the conventional approach for RF localisation involves human efforts to deploy a set of anchors in known coordinates.

The exploration of unknown environments has attracted increased attention due to its broad range of application scenarios, including search and rescue missions [159], disaster recovery [160], planetary exploration [161], photogrammetry [162], aerial inspection and monitoring of buildings and structures [163] [164], agriculture [165], and predictive maintenance [166]. Localisation and positioning capabilities are primary features for any autonomous exploration system. According to the application scenarios, several solutions can be used. The capability of positioning in an absolute reference system, usually with the GPS signal [167], is one of the most used techniques. However, many robot exploration activities are in GNSS-denied environments, such as indoor. In such challenging cases, alternative positioning methods are usually considered, e.g., visual-SLAM [168] [169], laser scanners [170]. Some of these techniques require non-negligible computing resources, work preferably in information-rich environment, and cannot guarantee a maximum target uncertainty (e.g., SLAM) [171]. Others, instead, have limited computational burden and can compute positioning under controlled uncertainty. Nevertheless, this class of solutions usually requires instrumented infrastructure in the surrounding with active or passive markers. Examples of this category are Radio Frequency (RF) active beacons for Radio Signal Strength Identification (RSSI) [172] or Ultra Wide Band (UWB) [100] [173] [66], while for passive solutions we can mention visual markers [174] or passive RFID tags [175]. The nature of the technology and the sensors embedded into the environment determine uncertainty during the exploration.

Providing positioning measurements with limited uncertainty for autonomous robot navigation is hard if an absolute reference as the GPS is not available. The achievable positioning performance depends both on the specific technology used by the sensing devices and on the algorithm

defined for the placement of such devices [176]. When RF ranging sensors are considered, two different approaches are usually implemented to achieve the optimal placement in an unknown environment:

1. **Off-line**. The environment is analyzed, e.g., using statistics about the navigation paths, and the placement positions are determined to guarantee the desired target uncertainty. For example, in [177], three off-line algorithms are assessed and compared to find the candidate points of an additional beacon that maximizes the accuracy of the localisation service over the entire region.

2. **Online**. In this case, the environment may not be known upfront, and the anchors are deployed on-demand, e.g., when the localisation uncertainty approaches the maximum tolerable value. For instance, in [178], the robots use two different strategies to place a new sensor in the environment: measure the average of RSSI, and place the new sensor when this value falls under a predetermined value or based on a fixed distance.

Expanding the scope of positioning systems for robotic applications, one of the most complex challenges is encountered in the realm of space exploration.

Within this context, the pivotal technological solution revolves around the localization and positioning of robots, human beings, and any other entities of interest navigating the environment. Presently, a myriad of solutions exists to address positioning from a comprehensive standpoint.

For instance, the Global Navigation Satellite System (GNSS) enables the computation of a receiver's position on the Earth's surface: in this respect, the Global Positioning Unit (GPS) is part of the quartet of available GNSSs, which also includes the GLONASS, the GALILEO and the BeiDou systems. However, it is widely acknowledged that signals from these systems may prove unreliable or unavailable in specific environments, such as mines. Moreover, in terrains with varying morphology featuring hills and valleys, the accuracy of GNSS significantly diminishes. Another fascinating scenario that has become quite popular in the last few years is the Mars

FIGURE 3.1: Scenario: a swarm of UAVs that localise themselves and provides simultaneously a positioning services to humans and robots on the ground. This image was created with the assistance of DALL-E.

Exploration Program[1]: exploring the most accessible locations in the solar system provides an opportunity to unravel the mysteries surrounding the origin and evolution of life.

As of the current writing, five active orbiter missions are dedicated to analysing Mars's atmosphere and categorising surface locations for autonomous robot exploration, with two missions currently in operation. As said, Mars lacks a Global Navigation Satellite System; hence huge and highly recognised positioning issues arise in such conditions, asking for the development of alternative strategies for localising robots, astronauts, and sensors on the ground, as shown in Figure 3.1. Due to the challenging operational constraints of such a scenario, there is also the clear need for a self-deployable system that should limit the human interventions just to sporadic high-level decision-making (such as controlling and managing the localisation network): this is also a field of growing interest in the community. Finally, there may be situations where a positioning network is essential for a specific task but only temporarily; hence, it becomes highly

[1] `https://mars.nasa.gov/mars-exploration/missions/?page=0&per_page=99&order=date+desc&search=&category=170%3A172`

desirable to have an autonomous system capable of rapidly providing such services without extensive human involvement.

In the literature, several works are proposed to supply a positioning system where the GNSS signal is not available or unreliable. In [63, 92, 179], a positioning system based on visible light communication (VLC) technology is proposed: the choice of this particular means of communication turns out to be intrinsically robust to the radio-frequency positioning systems downsides, like multipath reflections. Other researchers propose systems based on acoustic signals [62, 180, 181] to compute the receiver's position. The solution proposed in [182, 183] leverages a vision system to implement a tracking system. All the solutions mentioned above need a structured environment, where the human plays a central role in manually placing the positioning infrastructure, not to mention the cost of the devices (especially for vision systems), possible acoustic environmental pollution, and the need for power supply. A cooperative and self-organising positioning system is desirable to avoid these limitations and provide a viable solution for planetary explorations.

In [184], a cooperative localisation algorithm is proposed when no fixed infrastructure is available, building upon the theory of factor graph and the sum-product algorithm. In [67], a positioning infrastructure is built on the fly, orchestrating multiple vehicles. In [185], a localisation and target tracking system is proposed for an underwater autonomous vehicle using a particle filter, where a fraction of the involved vehicles act as temporary anchors for the others. In [186], a positioning system based on ranging information is proposed, leveraging the multidimensional scaling algorithm. Despite their effectiveness, all these solutions are either based on tracking, i.e., the positioning data is computed and stored in the temporary anchors and, hence, it should be sent to the receiver, thus affecting the overall update rate and limiting the scalability of the system, or they are solutions that do not explicitly consider the target motion.

The most promising solution to reduce the complexity of the problem and pass from a centralised to a decentralised system is the multidimensional scaling (MDS) algorithm. [186] provides a distributed and weighted version

of the traditional MDS assuming that an initial guess of the node positions, for instance provided by a GNSS module (indeed, the MDS encounters an intrinsic geometric ambiguity of the solutions [77]). Nonetheless, the problem of the scalability of the number of receivers and the limitations on the communication scheduling still needs to be addressed. In our previous work [187], we have proposed a solution for the geometry ambiguity that uses no additional information. Moreover, we have definitely solved the scalability problem on the receivers' side using an innovative algorithm to supply a positioning service based on the same principle of GNSS [66, 188] that guarantees a certified uncertainty level to all the receivers, which is not possible using the standard approach (if more receivers are asking for positioning information, dedicated messages should be sent, hence increasing the network congestion and, as a consequence, the positioning uncertainty).

3.1 Flight Dynamics: Exploring an Infrastructure-Less UWB-Based Leader-Follower System for Compact UAVs in a Relative Positioning Framework

As highlighted above, robots are becoming increasingly prevalent in our daily lives, with aerial robotic platforms being particularly prominent for various tasks. Section 3.1 delves into an initial exploration of human-robot interaction, focusing on a scenario where an autonomous UAV is assigned the role of tracking a human subject using solely UWB-based positioning technology. The approach, termed the "Leader-Follower" paradigm, entails an autonomous UAV follower mirroring the actions of a human leader. This paradigm is applicable to various mobile robots and involves computing a reference point near the human for guiding the follower's movements. The setup involves a human subject equipped with a single UWB transceiver (referred to as the "target" or "tag"), while the follower is a compact 250 mm wheelbase UAV fitted with three UWB transceivers (referred to as "anchors") arranged in a triangular formation to mitigate positioning ambiguities. (see Figure 3.2 for a snapshot of the developed UAV follower prototype). Within the described application, the main contributions of this section are:

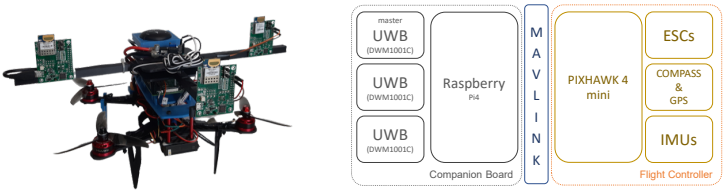

(a) (b)

FIGURE 3.2: (a) UAV follower prototype. (b) Follower system architecture. On the left the three UWB radios along with the RPi 4 companion board. The master DWM1001C is in charge of collecting the data from the other UWB radios and stream them to the RPi 4. On the right the UAV avionics. Companion board to flight controller communication is implemented using a MAVLINK.

- An analysis of the impact of the geometric shape and baseline of the 3 UWB anchors mounted on the follower on the accuracy of the position estimates;
- The development of an algorithm that given the position estimates, track the tag with desired precision;
- The development of Hardware-in-the-Loop simulations for the algorithm evaluation and the integration of the proposed solution on a commercial compact 250 mm UAV with preliminary experimental results.

3.1.1 The Catch-Me-If-You-Can Solution

Let us consider the UAV follower prototype reported in Figure 3.2, which is endowed with three UWB anchors placed at distance b with respect to the centre of mass of the UAV on an equilateral triangular configuration. The target person, i.e., the leader, is tracked using an UWB tag, whose position is determined by the Cartesian coordinates of the tag in the UAV reference frame, dubbed $\langle U \rangle$, and whose coordinates are expressed as $\mathbf{p} = [x, y, z]^T$. The three UWB anchor positions, i.e., $\mathbf{a}_i = [x_i, y_i, z_i]^T$, are known and expressed in the same reference frame $\langle U \rangle$, with $z_i = 0, \forall i = 1, 2, 3$, and are depicted with blue circles in Figure 3.3. The i-th anchor is able to deliver a

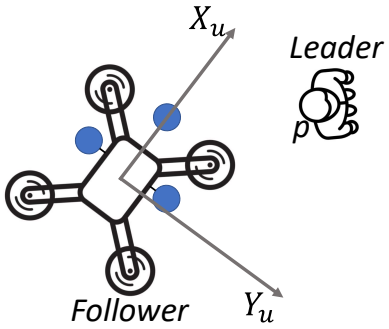

FIGURE 3.3: Reference systems considered for the leader-follower application. The blue circles represent the positions of the three UWB anchors, all expressed in the depicted UAV reference frame $\langle U \rangle$.

distance to the UWB tag, i.e.,

$$\rho_i = \sqrt{(x_i - x)^2 + (y_i - y)^2 + (z_i - z)^2} + \eta_i = \overline{\rho}_i + \eta_i, \tag{3.1}$$

where η_i is the uncertainty contribution, which is supposed to be normally distributed, zero-mean and white, that is $\eta_i \sim \mathcal{N}(0, \sigma(\overline{\rho}_i)^2)$. Its variance in general depends on the actual distance $\overline{\rho}_i$ and on the UWB signal bandwidth [189]. Considering Line of Sight (LOS) conditions and neglecting shadowing and multipath effects (a customary assumption for outdoor applications), the UWB module introduces a delay in the timestamp due to internal circuitry [190], which is different for each radio and a function of the actual distance [191]. Therefore, the ranging measurements (3.1) turns to

$$\rho_i = \beta_i(\overline{\rho}_i) + \overline{\rho}_i + \eta_i, \tag{3.2}$$

where $\beta_i(\overline{\rho}_i)$ is a bias that has to be taken into account for the foreseen application.

In order to keep the structure of the UAV compact and cheap, only three planar anchors can be installed on the platform at distance b. As a consequence, having just three anchors, only planar estimates can be carried out using trilateration [134], which is, however, a quite common assumption when

UAVs are considered [67]. To solve this issue for the problem at hand, we assume that the UAV collects the measurements about its height h from the ground using additional sensors (e.g., a sonar pointing downwards and/or a barometer). Assuming that the target moves on the ground as well, the z coordinate of the tag $\mathbf{p}$ in $\langle U \rangle$ along the Z_u axis (that is the axis pointing downwards in Figure 3.3) is actually unknown and cannot be estimated if no knowledge about the motion of the target is considered. Therefore, let us denote with d^* the desired distance between the leader and the follower along the X_u axis (see Figure 3.4), while $\overline{d}$ is the actual distance in $\langle U \rangle$, i.e., $\overline{d} = \|\mathbf{p}\| = \sqrt{x^2 + y^2 + z^2}$. If the z coordinate of the tag $\mathbf{p}$ would be known, it would be possible to consider the projection $\mathbf{p}^*$ of the vector $\mathbf{p}$ onto the $X_u \times Y_u$ plane, i.e., $\mathbf{p}^* = [x, y, 0]^T$, and then control the UAV in order to have $\mathbf{p}^* \to [d^*, 0, 0]^T$. Since the coordinate z is unknown and not observable, we conservatively assume that $z = h$, i.e., the height of the UAV from the ground, thus yielding a projection $\tilde{\mathbf{p}}^* = [x - \delta_x, y - \delta_y, 0]^T$, with $\delta_x \geq 0$ and $\delta_y \geq 0$. This way, the target appears closer than it is in reality. Hence, when $\tilde{\mathbf{p}}^* \to [d^*, 0, 0]^T$, the UAV will be at a larger distance from the leader. Notice that, in the worst scenario, that is when $z = 0$, the distance from the tag will be $\sqrt{d^{*2} + h^2}$.

Another issue to deal with is the presence of the bias, reported in (3.2). As a matter of fact, this bias cannot be estimated online without the knowledge of the motion of the leader. However, its effect can be highly mitigated through calibration. Indeed, by assuming that the bias is mainly induced by the available hardware, it can be considered time invariant. Albeit its value still depends on the actual distance, we can safely assume for the i-th anchor that $\beta_i(\overline{\rho}_i) \approx \beta_i(d^*)$, which allows us to increase the efficacy of this approximation once the UAV is driven towards the desired location. Similarly, we will assume that the uncertainty η_i standard deviation $\sigma(\overline{\rho}_i)$ is sufficiently small, constant and equals to σ. Therefore, we will consider from this point on the availability of the bias-compensated ranging measurement (3.1) instead of (3.2). The validity of this assumption and the calibration procedure will be investigated in Section 3.1.2.

In light of the previous discussion and the conservative assumption derived, we will consider henceforth the planar problem that can be solved with a trilateration approach. In particular, we will propose two different approaches for positioning, namely the *Linear Least Square* (LLS) and the *Non-Linear Least Square* (NLLS), and the Kalman filter for continuous tracking of the leader. Notice, nonetheless, that the distance between the anchors $\mathbf{a}_i$ plays a crucial role in the reachable positioning uncertainty of the leader. Indeed, geometry matters in the deployment of the anchors for positioning problem, which can be related to the Geometric Dilution of Precision and to the Cramer-Rao Lower Bound (CRLB), as reported in [3].

Leader positioning solutions

In what follows, we will assume that the sampling frequency of each anchor $\mathbf{a}_i$, $i = 1, 2, 3$, is approximately the same. As reported in [192], the estimates of the planar coordinates $\mathbf{p}_r = [x, y]^T$ in $\langle U \rangle$, dubbed $\hat{\mathbf{p}}_r = [\hat{x}, \hat{y}]^T$, can be retrieved by the following unconstrained minimisation problem

$$\hat{\mathbf{p}}_r = \arg\min_{\mathbf{p}_r} \sum_{i=2}^{3} \left(\|\mathbf{p}_r - \mathbf{a}_i\|^2 - \rho_i^2 \right) - \left(\|\mathbf{p}_r - \mathbf{a}_1\|^2 - \rho_1^2 \right), \tag{3.3}$$

which turns to the following LLS problem and related solution

$$\hat{\mathbf{p}}_r = \arg\min_{\mathbf{p}_r} (A\mathbf{p}_r - \mathbf{c})^T (A\mathbf{p}_r - \mathbf{c}) = (A^T A)^{-1} A^T \mathbf{c} \tag{3.4}$$

where

$$A = - \begin{bmatrix} 2(x_2 - x_1) & 2(y_2 - y_1) \\ 2(x_3 - x_1) & 2(y_3 - y_1) \end{bmatrix},$$

and

$$\mathbf{c} = \begin{bmatrix} (x_1^2 + y_1^2 - \rho_1^2) - (x_2^2 + y_2^2 - \rho_2^2) \\ (x_1^2 + y_1^2 - \rho_1^2) - (x_3^2 + y_3^2 - \rho_3^2) \end{bmatrix},$$

and the implicit approximation that $\hat{\mathbf{p}} = [\hat{\mathbf{p}}_r^T, h]^T$, i.e., the tag is on the motion plane, as discussed above.

The NLLS solution, instead, solves the following nonlinear cost index directly

$$\hat{\mathbf{p}}_r = \arg\min_{\mathbf{p}_r} \sum_{i=1}^{3} \left(\|\mathbf{p}_r - \mathbf{a}_i\| - \rho_i \right)^2 . \tag{3.5}$$

This problem can be solved with many different numerical methods, however it has been shown in [3] that, starting from the LLS solution (3.4) as first initial guess, the estimation precision reaches the CRLB with just a couple of iterations of the Gauss-Newton method.

It is worthwhile to point out that if the dynamic of the leader is slow enough in comparison with the sampling time of the anchors, it is possible to use multiple measurements from each anchor. In such a way, assuming that m_i is the number of measurements available for the i-th anchor, (3.3) turns to

$$\arg\min_{\mathbf{p}_r} \sum_{i=2}^{3} \sum_{j=1}^{m_i} \left(\|\mathbf{p}_r - \mathbf{a}_i\|^2 - \rho_{i,j}^2 \right) - \left(\|\mathbf{p}_r - \mathbf{a}_1\|^2 - \rho_{1,j}^2 \right),$$

while (3.5) turns to

$$\arg\min_{\mathbf{p}_r} \sum_{i=1}^{3} \sum_{j=1}^{m_i} \left(\|\mathbf{p}_r - \mathbf{a}_i\| - \rho_{i,j} \right)^2 ,$$

where $\rho_{i,j}$ stand for the j-th measurements from the anchor $\mathbf{a}_i$. Of course, in both cases, the solutions remains the same as in the single measurement case.

Kalman filter for tracking

The measured positions $\hat{p}_r$ obtained either by (3.4) or by (3.5) are used in the update step of a Kalman Filter (KF) that keeps track of the location of the leader in $\langle U \rangle$. Such measurements are considered affected by an uncertainty ν, which is assumed to be Gaussian, zero-mean and white, i.e., $\nu \sim \mathcal{N}(0, R)$. The covariance matrix R is hence a 2×2 matrix whose entries are experimentally determined in Section 3.1.2.

Instead, for the prediction step of the KF, we first assume that both the velocity of the UAV and of the target are limited by $v_m = 2.0$ m/s, which

is a standard choice when the leader is a human being walking in free space. The dynamic model considered in the prediction step represents the relative motion between the follower and the leader, i.e., a motion model expressing the difference of the dynamic between the UAV and the target. Even though human beings motion models exists in the literature, for instance [193], we decided to use a constant velocity model due to its simplicity and due to the effectiveness in non-cluttered environments [194]. The effect of such assumptions is that the motion of the human being does not change abruptly during the KF time step δ_t, which is usually the same of the sampling time of the ranging measurements and in the order of tens of milliseconds. As such, the Euclidean distance between the UAV and the tracked person does not change significantly, while a change of direction can be entirely devoted to the yaw angle rate of the UAV. Therefore, the simplified model for predicting the person's position in $\langle U \rangle$ boils down to

$$\hat{\mathbf{p}}_{f,k+1} = C_k \hat{\mathbf{p}}_{f,k} + \varepsilon_k \tag{3.6}$$

where $\hat{\mathbf{p}}_{f,k+1}$ is the estimate of the KF at time $(k+1)\delta_t$ and where, assuming that θ_k is the yaw of the UAV, the transition matrix

$$C_k = \begin{bmatrix} \cos(\theta_{k-1} - \theta_k) & -\sin(\theta_{k-1} - \theta_k) \\ \sin(\theta_{k-1} - \theta_k) & \cos(\theta_{k-1} - \theta_k) \end{bmatrix}.$$

The model uncertainty ε_k is responsible of the inaccurate motion model assumed, and it is generated by a Gaussian, zero-mean, white and stationary stochastic process, whose covariance matrix Q is given by

$$Q = \begin{bmatrix} (v_m \delta_t)^2 & 0 \\ 0 & (v_m \delta_t)^2 \end{bmatrix}.$$

The KF estimation error covariance matrix at time $k\delta_t$, i.e., P_k, is initialised with R, that is $P_0 = R$, since the first estimate of $\hat{\mathbf{p}}_{f,0}$ is given directly by (3.4) or by (3.5).

As reported in Figure 3.4, when two consecutive position estimates $\hat{\mathbf{p}}_{f,k+1}$ and $\hat{\mathbf{p}}_{f,k}$ are determined in $\langle U \rangle$ and by knowing the motion of the UAV (obtained directly by the applied control law), it is possible to identify the

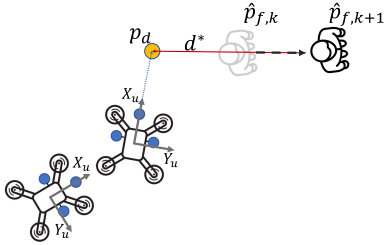

FIGURE 3.4: Position of the UAV desired position $\mathbf{p}_d$, which is computed using two consecutive KF position estimates $\hat{\mathbf{p}}_{f,k+1}$ and $\hat{\mathbf{p}}_{f,k}$.

desired robot position $\mathbf{p}_d$, which is on the back of the leader at distance d^*. Now, the controller has all the ingredients to generate a velocity set-point $v = [v_x, v_y]^T$ for the UAV in order to move towards $\mathbf{p}_d$ and, hence, follow the target at the desired distance d^*. In particular, v is generated so as to let the UAV asymptotically approach $\mathbf{p}_d$ plus the estimated target velocity, i.e., $\frac{1}{\delta_t}(\hat{\mathbf{p}}_{f,k+1} - \hat{\mathbf{p}}_{f,k})$. To further enforce safety, the UAV stops when the detected distance to the target is smaller than d^*.

3.1.2 Characterisation and preliminary results

A proper characterisation of the target positioning error is required for designing the system and finding the right balance among the elements to ensure the effectiveness of the system.

UWB characterisation and calibration

To characterise the precision and improve the accuracy of the ranging measurements, as well as to compensate for the effect of the bias term in (3.2), we conducted static and dynamic indoor experiments in which we compare the ranging measurements ρ_i obtained from the available UWB anchors with the distances $\overline{\rho}_i$ retrieved from the motion capture (MOCAP) system, here considered as ground truth. As aforementioned, considering an outdoor obstacle-free area, where the UWB anchors can operate in LoS conditions, we first analyse the influence of the bias $\beta_i(\overline{\rho}_i)$. From the results in Figure 3.5-a where the anchor $\mathbf{a}_1$ has been tested (similar results are

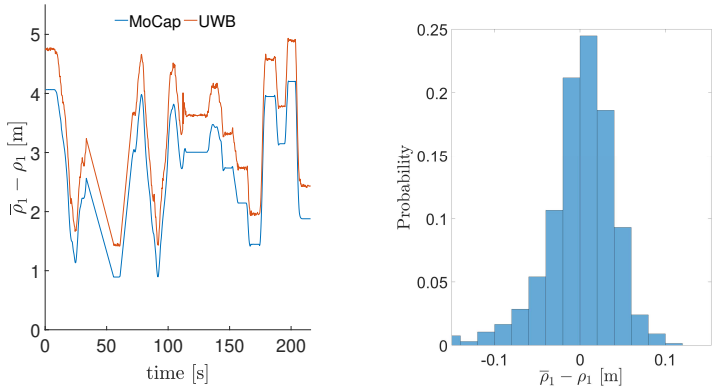

(a) (b)

FIGURE 3.5: (a) Distance measured by $\mathbf{a}_1$ (red line) and the actual distance (blue line) to infer the bias $\beta_1(\overline{\rho}_1)$. (b) Error histogram of $\overline{\rho}_1 - \rho_1$ after the bias in Table 3.1 has been compensated.

TABLE 3.1: Value of bias β_i and σ_i for the UWB anchors. The size of the batch for each anchor in each position is of 2000 samples.

Parameter	$\mathbf{a}_1$	$\mathbf{a}_2$	$\mathbf{a}_3$
β_i [mm]	584	695	617
σ_i [mm]	41	48	38

obtained for all the other anchors), it turned out how the bias is indeed independent from $\overline{\rho}_i$, since for different actual locations of the tag, the difference between the MoCap data (blue line, corresponding to $\overline{\rho}_i$) and the UWB data (red line, corresponding to ρ_i) is approximately the same. In order to collect quantitative results, during the calibration process, we removed the outliers that consist on average of around 0.5% of each given batch of data, thus obtaining the estimates for both the bias and the standard deviations for all the anchors reported in Table 3.1. Figure 3.5-(b) illustrates the histogram of the estimated distance after the bias compensation for anchor $\mathbf{a}_1$.

Simulation results

In this section, we assess the performance and the sensitivity of the positioning LLS and NLLS solutions presented in Section 3.1.1 through comprehensive simulations using the Gazebo simulator and with the purpose to analyse the effects of

1. Distance b between anchors and centre of mass of the UAV;
2. Bias in measurements;
3. Number of measurements available.

In the simulator the ranging measurements for the three anchors installed on the drone are corrupted by a gaussian noise $\eta \sim \mathcal{N}(0, \sigma_i^2)$ with reference to (3.2) and Table 3.1.

Anchors distance

The three UWB anchors are deployed around the UAV centre of mass in a triangular configuration to reduce the detrimental effects of the position dilution of precision [3]. The output of this first analysis shows how the performance of the positioning method is affected by the baseline b of the anchors. To this end, we set up a Monte Carlo experiment with 52000 trials in which we vary the baseline between the anchors as $b \in [0.1, \ldots, 0.5]$ [m]. The average position error considering $m_i = 5$ repeated ranging measurements for each anchor are reported in Figure 3.6. As expected, the increase of the baseline b leads to a better accuracy. However, a baseline $b = 20$ cm is sufficient to have good precision and to place the radio hardware on most compact commercial drone airframes (i.e., 250-class). Moreover, we also noticed that the NLLS solution yields better results with respect to the LLS.

Effect of bias on measurements

WE additionally conducted Monte Carlo simulations with 4000 trials to understand the effect of the bias β_i on both the solution NLLS and LLS. In each experiment, we change the value of the bias as $\beta_i = \{0, 5, 10, 15, 20\}$ [cm]. The results obtained in the worst case are reported in Figure 3.7 with respect

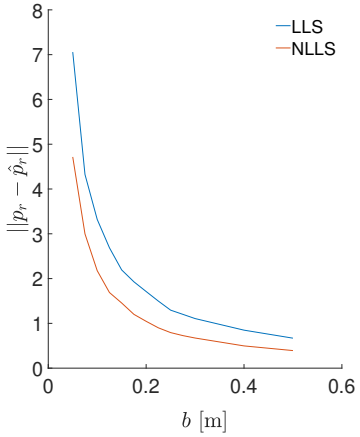

FIGURE 3.6: Average position error $\|\mathbf{p}_r - \hat{\mathbf{p}}_r\|$ of the Monte Carlo simulations for different values of the baseline b and for both the LLS and the NLSS solutions.

to the position error $\|\mathbf{p}_r - \hat{\mathbf{p}}_r\|$. Also in this case the error is well contained by the NLLS, while the LLS returns quite bad results. By comparing Figure 3.6 and Figure 3.7, it becomes evident how the bias calibration and compensation turns to be a clear performance booster.

Consistency of the position algorithms

To verify that the NLLS positioning algorithm is consistent even in our case when more data is made available [134], the following cycle is repeated N_{rep} times:

- A set of $m_i = 5$ ranging measurements between the target and each anchors is collected;
- The average position of the target is estimated using both the LLS and the NLLS algorithms.

Looking at Figure 3.8 we can see that increasing N_{rep} significantly improves the accuracy of the position estimate. Using the results obtained for the

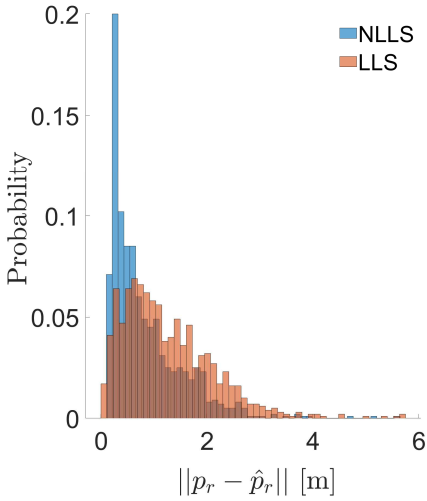

FIGURE 3.7: Histogram of the position error $\|\mathbf{p}_r - \hat{\mathbf{p}}_r\|$ for the NLLS and LLS solutions with a bias $\beta_i = 0.2$ m.

NLLS and with the aforementioned parameters, it is possible to compute the empirical Monte Carlo-based covariance matrix of the position estimation error for the NLLS solution to be used as the matrix R in the KF, i.e.

$$R = \mathrm{E}\left\{\mathbf{e}\mathbf{e}^T\right\} \approx \begin{bmatrix} 0.627\ \mathrm{m}^2 & 0.001\ \mathrm{m}^2 \\ 0.001\ \mathrm{m}^2 & 0.630\ \mathrm{m}^2 \end{bmatrix},$$

where $e_x = x - \hat{x}$ and $e_y = y - \hat{y}$ are the positioning errors along the X_u and Y_u axis of $\langle U \rangle$, respectively, while $\mathbf{e} = [e_x - \mathrm{E}\{e_x\}, e_y - \mathrm{E}\{e_y\}]^T$.

Validation

A Hardware-in-the-Loop (HITL) experiment was conducted to validate the proposed low-cost UWB-based person tracking system. Based on the previous analysis, the distance between the UAV centre and the UWB anchors is chosen to be $b = 20$ cm, while the number of repeated measurements for each UWB radio is set to $m_i = 5$. To test the positioning and control

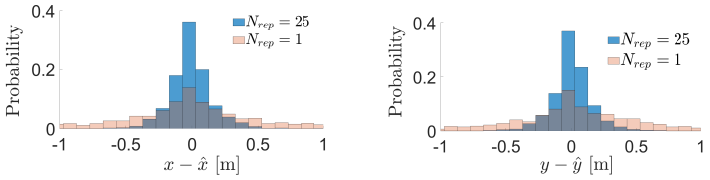

(a) (b)

FIGURE 3.8: Distributions of error $e_x = x - \hat{x}$ and $e_y = y - \hat{y}$ for the solutions with $N_{rep} = \{1, 25\}$.

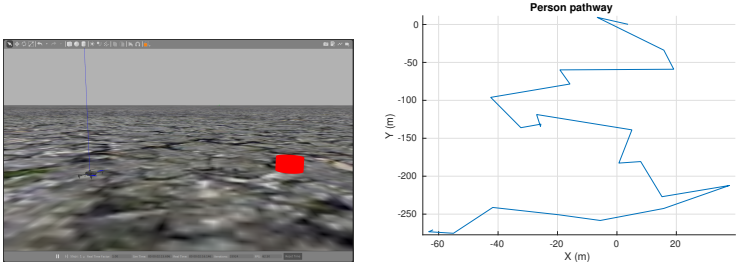

(a) (b)

FIGURE 3.9: (a) Gazebo simulation environment with the UAV (a quadrotor) and the target (represented by the red cylinder). (b) The path traveled by the target.

algorithms, a typical motion pattern is applied to the target based on [195], as shown in Figure 3.9.

The histogram of the error of the estimated positions is shown in Figure 3.10. It can be noticed that, despite the approximations described, the error remains limited even in the human beings sharp change of directions reported in Figure 3.9-b.

Preliminary experimental results

At the stage of the writing, the outdoor test are executed without a ground truth. In Figure 3.11 is shown a frame of the outdoor test, while a full video of the experiment is available at the following link[2]. In the video material,

[2]https://www.youtube.com/watch?v=_SPHzfz6aXU

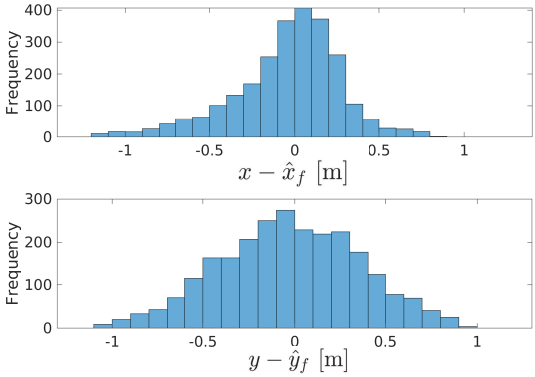

FIGURE 3.10: Histogram of the tracking error $x - \hat{x}_f$ and $y - \hat{y}_f$ returned by the KF.

FIGURE 3.11: Preliminary outdoor test.

there is a manoeuvre, called *twirl*, executed during the lock on target: its purpose is only to give a visual feedback to the user and increase the user confidence and trustfulness. The outdoor experiments are very promising and the system was able to correctly track the human being at the desired distance with minor errors (in the order of some tens of centimetres) even along sharp turns.

3.2 Optimizing Exploration: On-Line Deployment of Optimal Ranging Sensors for Robotic Exploration

In the previous section, we explored a specialized tracking system tailored for interactions between UAVs and humans. However, this system serves a specific purpose where a global reference frame for navigation is not required. In contrast, traditional indoor positioning systems rely on pre-deployed infrastructure for navigation. The key feature of UWB technology lies in its utilization of message exchange between mobile and fixed nodes. Generally, mobile nodes are installed on the robot, while fixed nodes, termed anchors, establish an infrastructure with predetermined geometric properties. The fixed structure of nodes is usually deployed before starting any operations in the environment [196], hence adopting an off-line placement procedure. Although it seems simple, off-line placement is time-consuming and critical because any fault in this phase or anchor position uncertainty seriously influences the positioning system's precision.

We devised a novel method to address inaccuracies in infrastructure setup and enable positioning in unstructured environments where offline analysis is impractical. The proposed approach involves dynamically placing and extending infrastructure anchors at runtime, a feature not found in existing literature. As a mobile robot explores the environment, it autonomously deploys new anchors to bolster the infrastructure, thereby expanding the positioning reference in real-time. This contrasts sharply with prior solutions which lack the capability to adapt infrastructure based on robot requirements or effectively manage information uncertainty introduced by new anchors. Unlike traditional methods that optimize the entire region at once, the proposed robot-centered solution is lightweight computationally and can operate in unknown or partially known environments. We propose an online-incremental algorithm, employing a genetic approach, to optimize anchor placement and minimize deployments while ensuring positioning uncertainty meets user-defined requirements, measured by Geometric Dilution of Precision (GDoP). While the proposed solution is compatible with various positioning uncertainty metrics, GDoP is particularly suited for this purpose.

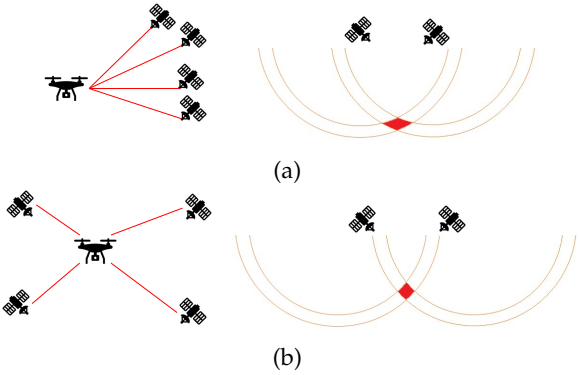

FIGURE 3.12: Circular sector intersections from (a) bad or (b) good distributions of satellites

In this section, we focus on positioning accuracy problems and not strictly on robot localisation, which requires the analysis of the problem's observability and the model of the robot dynamics [197]. We present how to use the proposed approach for a generic class of robot dynamics (e.g., ground or aerial vehicles), mainly focusing on positioning uncertainty.

3.2.1 Background and Problem Formulation

GDoP is a metric adopted to quantify the precision and accuracy of the data received from GPS satellites, which is now being adopted to the wider set of generic positioning system [198, 199]. This metric indicates how well the satellites are geometrically organized. The lower the value, the better is the position accuracy [200]. A graphical representation of a poor or good geometric configuration is given in Figure 3.12. GDoP is proportional to the ratio between the range error and position error [201], thus it is inversely proportional to the volume formed by the vectors from user to satellites and the number of satellites. Given the distance ρ_i from the i-th anchor and assuming that all the ranging measurements have the same finite variance (hence, the homoscedastic property is satisfied), we define the variance associated to the ranging as σ_ρ^2 and, from [202], the covariance matrix of the

positioning error is

$$C = \sigma_\rho^2 \begin{bmatrix} \sigma_{xx}^2 & \sigma_{xy}^2 & \sigma_{xz}^2 & \sigma_{xt}^2 \\ \sigma_{yx}^2 & \sigma_{yy}^2 & \sigma_{yz}^2 & \sigma_{yt}^2 \\ \sigma_{zx}^2 & \sigma_{zy}^2 & \sigma_{zz}^2 & \sigma_{zt}^2 \\ \sigma_{tx}^2 & \sigma_{ty}^2 & \sigma_{tz}^2 & \sigma_{tt}^2 \end{bmatrix}, \tag{3.7}$$

where $\sigma_\rho^2\sigma_{xx}^2, \sigma_\rho^2\sigma_{yy}^2, \sigma_\rho^2\sigma_{zz}^2$ represent the variance of the estimated location along the corresponding axes and σ_{tt}^2 is the time offset of the receiver. Sub-metrics can be defined from (3.7) by adopting the trace on different sub-matrices, such as

$$\begin{cases} \text{HDoP} = \sqrt{\sigma_{xx}^2 + \sigma_{yy}^2}, \\ \text{VDoP} = \sigma_{zz}^2, \\ \text{PDoP} = \sqrt{\sigma_{xx}^2 + \sigma_{yy}^2 + \sigma_{zz}^2}, \\ \text{GDoP} = \sqrt{\sigma_{xx}^2 + \sigma_{yy}^2 + \sigma_{zz}^2 + \sigma_{tt}^2}, \end{cases} \tag{3.8}$$

where HDoP, VDoP and PDoP are the Horizontal, Vertical and Position Dilution of Precision, respectively, all derived from the GDoP. We moved these metrics to UWB infrastructures. Thus the position estimate of a receiver (called *tag*) in a generic three-dimensional space requires at least four UWB devices (called anchors). In contrast to (3.7), the time t is not of interest for UWB ranging system because the propagation time of the signal is directly used for the time-of-flight measurement [203], hence the last column of C will be neglected. Consequently, the PDoP metric in (3.8) is used in place of the GDoP.

Problem formulation

The issue addressed in this section is to derive an optimal self-deployment on-line solution for UWB anchors during exploration problems and using the PDoP metric to define the target uncertainty. The optimal reduction of positioning uncertainties is tailored to the robotic platforms' requirements, saving onboard hardware and computation resources and time. The algorithm calculates the minimum number of anchors to deploy during

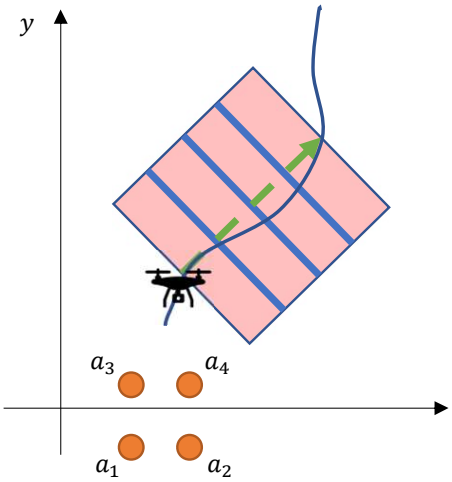

FIGURE 3.13: A graphical representation of the problem statement. Example of subareas $S(i+(j-1)r/n, jr/n)$, with j=1,...,n, using the described simplified approach.

the mission to accomplish the robot goal. More formally, let us consider the situation depicted in Figure 3.13. We assume that the anchors can only be deployed on the $X_w \times Y_w$ plane of the right-handed reference frame $\langle W \rangle = \{X_w, Y_w, Z_w\}$, since the altitude of the placement is assumed to be not controllable. Notice that assuming no knowledge about the environment, we consider the worst possible conditions for the z coordinates, i.e., that the multilateration algorithm is applied using coplanar anchors (flat terrain), hence we are assuming very poor VDoP. We denote with $a_i = [X_i, Y_i]^T$ the known coordinates of the anchor in $\langle W \rangle$ and projected on the plane $X_w \times Y_w$. Moreover, given $\mathcal{A}_k$ the set of all the anchors a_i, we define with $\overline{\mathcal{A}}_{k,n}$ as the set of all the combinations of n anchors in $\mathcal{A}_k$. Therefore, $\mathcal{D}_k(s) \in \overline{\mathcal{A}}_{k,4}$ denote the set of 4 anchors attaining the minimum value of PDoP in a certain position s. As a consequence, given:

- A sampling time T_s, which is induced by the sampling time of the available anchors;

- A planned exploration path $S_p = \{q_i\}_{i=1}^{h}$ is a set of h viapoints on the plane, i.e. $q_i = [x_{q_i}, y_{q_i}]^T$;
- The actual position of the robot $s_k = [x_k, y_k]^T$ at time kT_s, supposed to be projected on the plane $X \times Y$, while $S_k = \{s_i\}_{i=0}^{k}$;
- An initial set $\mathcal{A}_0$ of 4 anchors that are in communication with the robot;
- A set of the overall deployed anchors $\mathcal{A}_k$ up to time kT_s;
- A maximum tolerable value p^m of the PDoP along the exploration path;
- A maximum distance ρ^m from an anchor to retrieve the ranging measurement;
- A PDoP function $g(\mathcal{D}_k(s_k), s_k)$ computed on the position s_k given the anchors $a_i \in \mathcal{D}_k$;

the goal is to guarantee the existence of at least four anchors $\mathcal{D}_k \subset \mathcal{A}_k$ at time kT_s, such that the UWB positioning system can provide a PDoP $g(\mathcal{D}_k(s_k), s_k) \leq p^m$, $\forall s_k$ during the exploration while using the ranging data $\rho_{i,k} = \|s_k - a_i\| \leq \rho^m$. To this extend, we define two problems:
i) the first is the *Optimal placement problem* (OPP)

$$\begin{aligned} &\min \#\mathcal{A}_k \text{ s.t.} \\ &\exists \mathcal{D}_k(q_i) \subseteq \mathcal{A}_k \text{ with } g(\mathcal{D}_k(q_i), q_i) < p^m, \forall q_i \in S_p, \end{aligned}$$

where of course $\#\mathcal{A}_k$ are the number of elements in $\mathcal{A}_k$.
ii) The second, named *Optimal Exploration and Placement Problem* (OEPP), is based on OPP and defined on the actual robot positions s_k, instead of the planned positions q_i. The difference between the two problems is that OPP refers to the nominal robot trajectory, while OEPP considers all the maneuvers needed to deploy the new anchors.

In this application we will make explicit reference to a particular class of robots, namely Unmanned Aerial Vehicles (UAVs), even though the solution remains of general validity. It is worthwhile to mention that the algorithm

is totally agnostic about the planner used to synthesize the robot path. One of the most used exploration methods is the sampling-based algorithm such as RRT [204]. Moreover, notice that the robot should entirely cover the exploration path at least once, i.e. $\exists k \in \mathbb{N}$ such that $s_k = q_i, \forall q_i \in S_p$.

3.2.2 Anchors Deployment Algorithm

At a first glance, OPP may appear a trivial problem that could be solved by computing $g(\mathcal{D}_k(s_k), s_k)$ at time kT_s for the positions $s_k = q_i$ and place a new set of 4 anchors on the same pattern of Figure 3.13, when either $g(\mathcal{D}_k(s_k), s_k) = p^m$ or $\rho_{i,k} = \rho^m$ for some $a_i \in \mathcal{A}_k$. Then the robot starts over. However, we observe three different problems with this approach (which is inspired by [205] applied to ground wheeled vehicles):

1. While placing 4 anchors satisfies the sufficient requirement for positioning, it does not guarantee that it is the only possible deployment.

2. When the UAV places the 4 anchors, the PDoP should be kept under control on the placement trajectory as well, hence a PDoP threshold $p^* < p^m$ should be considered;

3. The next location to place the anchors may be a function of the future exploration path viapoints S_p, thus making some locations more favorable than others.

To address these issues, we propose the Genetic Anchor Node Placement (GANP) algorithm, which comprises a prediction of the PDoP function along the future path positions with a finite horizon r and then compute the most favourable locations using a Genetic Algorithm (GA). More precisely, let us consider the robot is in position $s_k = q_i$, the algorithm starts by evaluating if $\exists q_j \in \{q_i, q_{i+1}, \ldots, q_{i+r}\} = S_p^{(i,r)} \subset S_p$ such that $g(\mathcal{D}_k(q_j), q_j) > p^m$. In such a case, we need to add at least one anchor. We can then grow a region $\mathcal{S}_p^{(i,r)}$ around the path portion $S_p^{(i,r)}$ of width w by simply taking the local perpendicular to the path of length w passing through each position $q_j = S_p^{(i,r)}$. However, to avoid a placement that concentrates the anchors in nearby positions, we split the finite horizon r in n subsets of r/n points and then we could define non-overlapping regions $\mathcal{S}_p^{(i,r/n)}, \ldots, \mathcal{S}_p^{(i+r-r/n,i+r)}$

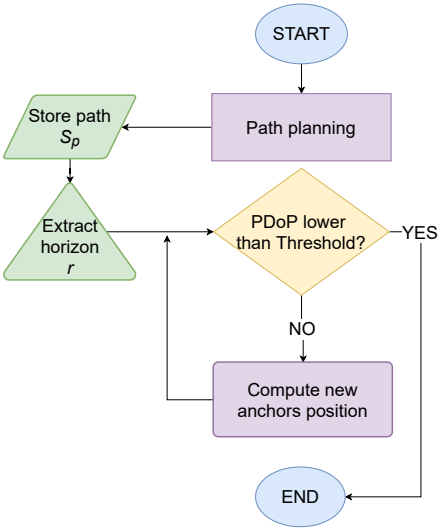

FIGURE 3.14: Flowchart of GANP algorithm.

each hosting at most one new anchor. To simplify the subareas splitting, we simply take the line joining q_i and q_{i+r} and consider it as an approximation of the path, thus simplifying the searching regions comprised in $\mathcal{S}_p^{(i,r)}$ as sketch in Figure 3.13. Of course, the width w of the searching region, the forecasting horizon r, and the number of sub-paths n plays a crucial role in the algorithm performance, hence a tuning procedure is presented in Section 3.2.4.

A flowchart of the GANP algorithm is depicted in Figure 3.14. Whenever one or more anchors should be placed according to the PDoP function, a list of the possible deployment coordinates is computed. The main idea is to allow at most one anchor in each subarea $\mathcal{S}_p^{(i+(j-1)r/n,jr/n)}$, with $j = 1,\ldots,n$. Suppose four anchors result placed in the j-th area to achieve an optimal PDoP value. In that case, it means that the considered j-th area is too detached (i.e., far) from the infrastructure, then $j-1$-th area is considered forcing the algorithm to generates at least one additional anchor.

The GA *fitness function* considers the optimal PDoP values for each point

$q_j \in S_p^{i,r}$ by determining the set $\mathcal{D}_k(q_j)$. The PDoP quantities are then stored into a list and weighted according to the distance from q_i: the more $\|q_j - q_i\|$ is larger, the higher is the weight. These values are then summed up and constitute the objective function to minimize, i.e.

$$Y = \sum_{i=1}^{r} g(\mathcal{D}_k(s_k), s_k)\ log(\|q_j - q_i\|).$$

Notice that the weighting mechanism pushes the new possible anchors deeper along the exploration path, maximizing the effect of the coverage and ensuring the minimum number of anchors for the considered subset $S_p^{i,r}$. The GA *constraint function* checks the following three conditions for each generated possible anchor location:

- The position of the generated anchor should have a PDoP value below the maximum threshold p^m;
- The path joining the robot position and the anchor candidate location should have a PDoP below p^m as well;
- The PDoP of all the positions in $S_p^{i,r}$ should be below p^m.

Notice that the GANP algorithm ensures the optimality of the OPP only. To extend the results to the OEPP, the nature of the deploying maneuver should be taken into account.

Deploying Manoeuvres

The GANP algorithm ensures that the value of PDoP never exceeds the maximum target value p^m. In fact, the algorithm governs the UAV controlled behaviour based on three states of a Finite State Machine. The UAV starts in *Mission State* (MS) where it follows the exploration path. When the condition is violated on the path horizon r, the optimal position of the anchor is determined, and the UAV switches to the *Deployment State* (DS). The UAV stores the last point reached along the mission path, say $q_i \in S_p$, and follows the shortest path towards the deploying location. After the anchor is positioned, the UAV either continues on the placement (if convenient, as described in the rest of this section) or it switches to the

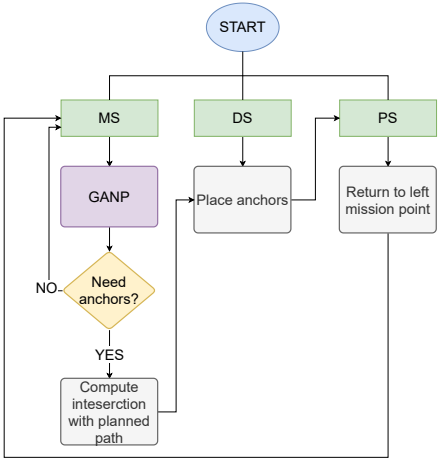

FIGURE 3.15: Overall logic that govern the behaviour of the drone during its mission.

Placed State (PS). Here, a return-path to q_i is generated and followed. When the robot reaches q_i either switches back to DS (if additional anchors should be placed, or returns to MS, where the exploration continues. This motion pattern is pursued until the last point of the mission is reach, where the UAV decides which action to perform:

- Landing (or stopping) and becoming an integral part of UWB positioning infrastructure with its tag that switches to an anchor. This action can be fired by the battery level when it falls below a certain threshold;
- Continue the exploration mission, selecting a new exploration area with a new synthesized path and executing the described process;
- Alternatively, the robot can move back to the starting position, increasing the accuracy of the placed anchors.

The flowchart of the depicted algorithm is reported in Figure 3.15. The path followed in the DS and PS states is crucial for any vehicle autonomy, especially when UAVs are considered. Therefore, the maneuver should

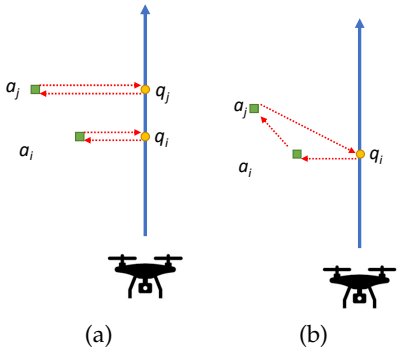

FIGURE 3.16: Deployment manoeuvres followed in DS and PS: (a) Deployment path generation, each anchor has its relative intersections point. (b) Deployment path generation, from first intersection point, all anchors in list are deployed.

take the shortest. While the placement path for a single anchor is straightforward, i.e., it is sufficient to move along the local perpendicular segment with respect to the planned path (see Figure 3.16-(a)), the placement of more than one anchor may be tricky. When the new anchor locations a_i and a_j are determined, two possible strategies are considered. The first is reported in Figure 3.16-(a): the back-and-forth motion is adopted whenever the UAV reaches an intersections points on the path (first q_i, then q_j). The second more involved situation is depicted in Figure 3.16-(b), where the UAV starts the deployment manoeuvres from the first intersection point, q_i, and sequentially place all the anchors before going back to the point q_i. The selection of the two strategies is made on the fly by comparing the perimeter of standard geometric shapes (recall that at most 4 anchors should be placed at once), with the constraint that the manoeuvre in DS starts and ends in the same point q_i (to cover the entire exploration path). For example, the path followed in DS for Figure 3.16-(b) is shorter than the path of Figure 3.16-(a), thus it will be selected. It is now evident that, by embedding this manoeuvre generation in the *constraint function* of the GA, the OEPP problem is solved requiring the limit of the PDoP to be satisfied along the shortest deployment manoeuvres.

3.2.3 Uncertainty analysis

In this section, we first present the explicit derivation of the PDoP function $g(\mathcal{D}_k(s_k), s_k)$ and an analysis of the positioning uncertainty accounting for the incorrect anchor deployment.

Position Dilution of Precision

As described in Section 3.2.1, the PDoP function used in this work $g(\mathcal{D}_k(s_k), s_k)$ is a function of the anchor locations $\mathcal{D}_k(s_k) = \{a_{i_1}, \dots, a_{i_m}\}$ and of the point s_k considered. In particular, defining with

$$P = \begin{bmatrix} \frac{x_k - X_{i_1}}{\rho_{i_1,k}} & \frac{y_k - Y_{i_1}}{\rho_{i_1,k}} \\ \vdots & \vdots \\ \frac{x_k - X_{i_m}}{\rho_{i_m,k}} & \frac{y_k - Y_{i_m}}{\rho_{i_m,k}} \end{bmatrix}, \tag{3.9}$$

the Jacobian of the ranging function (3.10) and denoting with Q the covariance matrix of the positioning error

$$Q = \sigma_\rho^2 (P^T P)^{-1} = \sigma_\rho^2 \begin{bmatrix} {\sigma_{xx}}^2 & {\sigma_{xy}}^2 \\ {\sigma_{yx}}^2 & {\sigma_{yy}}^2 \end{bmatrix},$$

the PDoP function $g(\mathcal{D}_k(s_k), s_k) = \sqrt{{\sigma_{xx}}^2 + {\sigma_{yy}}^2}$.

Anchor deployment uncertainty

The position of the UAV is computed using multilateration on distance measurements. The ranging measurements are collected by means of an UWB infrastructure, using a Single Side Two-Way-Ranging (SS-TWR) communication protocol. Assuming n UWB anchors in known positions $a_i = [X_i, Y_i]^T$, $i = 1, \dots, n$, the ranging measurement from the i-th anchor at time kT_s is defined as

$$\bar{\rho}_{i,k} = \rho_{i,k} + \epsilon_{i,k} = \sqrt{(x_k - X_i)^2 + (y_k - Y_i)^2} + \epsilon_{i,k}, \tag{3.10}$$

where $\epsilon_{i,k}$ is the ranging measurement uncertainty, usually considered as a white sequence with zero mean and variance σ_ρ^2 for all the anchors.

Computing the difference of the squares of the distances $\Delta_{ij,k} = \bar{\rho}_{i,k}^2 - \bar{\rho}_{j,k}^2$ from at least three anchors and using the same solution reported in [206], it is possible to derive the robot position estimates using a Weighted Least Squares (WLS) solution as

$$\hat{s}_k = \begin{bmatrix} \hat{x} \\ \hat{y} \end{bmatrix} = \frac{1}{2}(A^{(n)^T} N_k^{(n)^{-1}} A^{(n)})^{-1} A^{(n)^T} N_k^{(n)^{-1}} h_k^{(n)}, \tag{3.11}$$

where $h_k^{(n)}$ is the vector of the indirect measurements $\Delta_{ij,k}$ and anchor positions, $A^{(n)}$ is a matrix containing the known anchor positions, while

$$N_k^{(n)} = \sigma_\rho^2 \begin{bmatrix} \rho_{1,k}^2 + \rho_{2,k}^2 & \rho_{1,k}^2 & \cdots & \rho_{1,k}^2 \\ \rho_{1,k}^2 & \rho_{1,k}^2 + \rho_{3,k}^2 & \cdots & \rho_{1,k}^2 \\ \vdots & \vdots & \ddots & \vdots \\ \rho_{1,k}^2 & \rho_{1,k}^2 & \cdots & \rho_{1,k}^2 + \rho_{n,k}^2 \end{bmatrix}, \tag{3.12}$$

the covariance matrix of the measurements, which is a function of the actual distances $\rho_{i,k}$. The robot position uncertainty $\tilde{s}_k = \hat{s}_k - s_k$ derived from (3.11) has, hence, the following multilateration covariance matrix

$$\Xi^{(n)} = (A^{(n)^T} N_k^{(n)^{-1}} A^{(n)})^{-1} = \begin{bmatrix} \sigma_{x,k}^2 & \sigma_{xy,k}^2 \\ \sigma_{yx,k}^2 & \sigma_{yy,k}^2 \end{bmatrix}, \tag{3.13}$$

whose explicit form is reported in [206] and holds true when the anchor positions are perfectly known a-priori, i.e., a map of the anchors is available.

The problem presented in this section is different from the classic multilateration just reported, since for the problem at hand, the positions of the anchors are deployed by the robot, hence affected by uncertainty except for the very first set $\mathcal{A}_0$. From this perspective, the problem is more similar to a Simultaneous Localisation And Mapping (SLAM) problem rather than a standard positioning problem, since the anchor map is built on the fly. Indeed, while the ranging measurements from an anchor in $\mathcal{A}_0$ is simply (3.10), from the i-th deployed anchor turns to

$$\bar{\rho}_{i,k} = \sqrt{(x_k - \hat{X}_i + \delta_{i_x})^2 + (y_k - \hat{Y}_i + \delta_{i_y})^2} + \epsilon_{i,k}, \tag{3.14}$$

where we denote with $\delta_i = [\delta_{i_x}, \delta_{i_y}]^T$ the deployment error and with $\hat{a}_i = [\hat{X}_i, \hat{Y}_i]^T$ the estimated anchor position (i.e., $a_i = \hat{a}_i - \delta_i$). Assuming that the i-th anchor has been deployed at time kT_s, we have that $\hat{a}_i = \hat{s}_k$, hence given by (3.11), thus affected by an uncertainty described by the covariance matrix (3.13). In a typical SLAM problem, the first estimate of the position of a feature (which is used in the next steps as a landmark for localisation) is treated as the mean value of a random variable, usually considered as Gaussian. Applying this idea to the problem at hand, the feature estimate turns to be the anchor estimated position $\hat{a}_i$ and the δ_i the corresponding random variable of the uncertainty, customarily assumed with zero-mean and generated by a white stochastic process. To analyze the effect of this uncertainty, we may rewrite (3.14) with its first order Taylor approximation with respect to $\epsilon_{i,k}$ and δ_i, thus obtaining

$$\bar{\rho}_{i,k} = \rho_{i,k} + \epsilon_{i,k} + F\delta_i = \rho_{i,k} + \eta_{i,k}, \tag{3.15}$$

where $F = \frac{\partial \bar{\rho}_{i,k}}{\partial \delta_i}$ is the gradient of (3.14) evaluated in the mean value of δ_i, i.e. F is the same of P in (3.9), but evaluated in $\hat{a}_i$. Therefore, using (3.15) instead of (3.10), the overall uncertainty for the ranging measurements from deployed anchors is expressed by $\eta_{i,k}$, which is a white zero-mean sequence with variance

$$\sigma^2_{\eta_{i,k}} = \sigma^2_\rho + F\Xi^{(n)}F^T, \tag{3.16}$$

where $\Xi^{(n)}$ is given in (3.13) (i.e., the robot position uncertainty during the placement). Since $\sigma^2_{\eta_{i,k}} \geq \sigma^2_\rho$, when the i-th deployed anchor is used, the ranging uncertainty will be larger. For instance, assuming that at time kT_s the robot uses the anchors 1 and 2 from $\mathcal{A}_0$ and anchors i and j newly placed, i.e. for which only the estimates $\hat{a}_i$ and $\hat{a}_j$ are available, we have the new form of (3.12) as

$$N_k^{(n)} = \begin{bmatrix} \sigma^2_\rho(\rho^2_{1,k}+\rho^2_{2,k}) & \sigma^2_\rho\rho^2_{1,k} & \sigma^2_\rho\rho^2_{1,k} \\ \sigma^2_\rho\rho^2_{1,k} & \sigma^2_\rho\rho^2_{1,k}+\sigma^2_\eta\rho_{i,k} & \sigma^2_\rho\rho^2_{1,k} \\ \sigma^2_\rho\rho^2_{1,k} & \sigma^2_\rho\rho^2_{1,k} & \sigma^2_\rho\rho^2_{1,k}+\sigma^2_\eta\rho_{j,k} \end{bmatrix}.$$

However, the previous development along the lines of the classic SLAM approach is not entirely correct, as empirically proved in Section 3.2.4. Indeed,

δ_i should not be considered as a white random variable with zero-mean and covariance (3.13) but, instead, as a realization of a random variable at time kT_s, i.e., a realization of the random variable modelling the robot positioning uncertainty, hence an unknown but constant offset. With this assumption, a typical non Bayesian approach as the nonlinear WLS can be adopted. More precisely, given at least three consecutive ranging measurements $\bar{\rho}_{i,k}$, $\bar{\rho}_{i,k+1}$ and $\bar{\rho}_{i,k+2}$ described in (3.14), the value of δ_i is given by

$$\hat{\delta}_i = \underset{(\delta_{i_x},\delta_{i_y})}{\operatorname{argmin}} \sum_{j=k}^{k+2} [(\hat{x}_j - \hat{X}_i + \delta_{i_x})^2 + (\hat{y}_j - \hat{Y}_i + \delta_{i_y})^2 - \bar{\rho}_{i,j}^2]^2. \tag{3.17}$$

This way, the offset δ_i induced in the anchor placement by the robot position uncertainty $\tilde{s}_k$ can be estimated and, hence, removed from the anchor estimated position $\hat{a}_i$ by means of this nonlinear unconstrained regression problem, as shown in the next section. It is important to remark that the PDoP in (3.9) does not consider the effect of the offset on the deployed anchors position. These effects are voluntarily neglected because their contributions to the estimation of the PDoP generate. In the worst case of an offset in the order of tens of centimetres, a difference with the actual PDoP is less than 3% of p^m. Therefore, being the offset errors after (3.17) of the order of few centimetres, we simply impose a PDoP threshold of 95% of p^m to account for those effects and design a conservative approach.

3.2.4 Simulations and Experiments

To evaluate the effectiveness of the GANP algorithm, we first present here the simulation results. We assume that the maximum ranging distance is $\rho^m = 60$ m, which is derived by the hardware specification of the Decawave DWM1001 UWB anchors. To fine-tune the parameters of the GANP algorithm, i.e., the area width w, the number of subareas n and the horizon of the prediction r, we report here an analysis based on the Taguchi Orthogonal Array (OA) design [207]. To this end, we impose the maximum PDoP value to be $p^m = 1.5$ (a value guaranteeing low positioning uncertainty and a sufficiently large feasible placement region) and an exploration

TABLE 3.2: Performance of the GANP algorithm versus parameter choices.

Parameters			Performance indices		
w [m]	r [m]	n	m	d_t [m]	c_t [s]
10	10	2	12	138	1118
10	20	4	12	140	1007
10	30	3	11	145	450
30	10	4	10	166	307
30	20	3	9	154	362
30	30	2	9	146	895
50	10	3	9	170	680
50	20	2	9	180	650
50	30	4	9	176	526

TABLE 3.3: Optimal choices of the parameters.

Performance indices	w [m]	r [m]	n
m	50	30	3
d_t	10	30	2
c_t	30	30	3
Average value	27	30	3

path length of approximately 60 m. The result of the analysis, reported in terms of the performance indices number of anchors m, travelled distance d_t and computational time c_t, is subsumed in Table 3.2. It is evident that a larger area minimises the number of deployed anchors, since the feasible deploying space increases, at the price of a higher travelled distance. Instead, while the computation time clearly increases for larger areas (i.e., a larger space to explore for the GA algorithm), too small areas may imply difficulties in the search for a suitable solution. Hence the computation time increases as well. An optimal choice of the parameters would lead to the optimization of all the performance indices at once, which is hardly possible for the contrasting goals explained. Therefore, we compute the choice of the parameters w, r and n minimising each selected performance index at once and then compute the average among them, as reported in Table 3.3. The placement obtained with the depicted tuning is then applied to a simulation example, thus obtaining the level curves of the PDoP reported in Figure 3.17-(a). In this case, just 4 new anchors have been added to cover the entire exploration path and respecting the PDoP

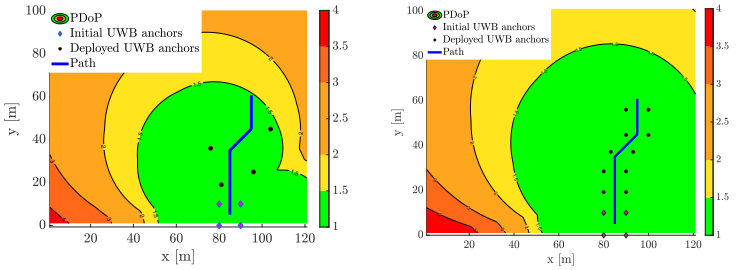

FIGURE 3.17: (a) PDoP level curves computed using $\mathcal{D}_k(s_k)$, where s_k covers the entire map; (b) PDoP level curves computed using $\mathcal{D}_k(s_k)$ for the straightforward algorithm sketched at the beginning of Section 3.2.2.

limit $p^m = 1.5$. For comparison, Figure 3.17-(b) reports the same scenario assuming the trivial approach sketched at the beginning of Section 3.2.2. It is evident that, albeit simple, this algorithm implies a waste of resources, imposing the PDoP region $g(\mathcal{D}_k(s_k), s_k) \geq p^m$ to be too wide comapred to the exploration task. Moreover, as it can be observed from Figure 3.18, the PDoP constraint is not always verified along the exploration path or the placement path for the simple approach, while it is strictly satisfied for the GANP algorithm. As a final simulation test, we verified that the SLAM-like assumption of the anchor estimated positions $\hat{a}_i$ cannot be considered as a random variable, as discussed in Section 3.2.3. To empirically prove this fact, we have carried out 10^6 Monte Carlo trials where δ_i uncertainty is treated as a random variable contributing to the random, zero-mean white noise in (3.16) and hence applying the multilateration (3.11), which results in the position uncertainty in Figure 3.19, dashed line. As can be noticed, this assumption end up with a non-negligible bias on the estimates of the estimated position $\hat{s}_k$ (the Figure 3.19 reports the bias on the $\hat{x}_k$ axis, but it acts similarly on $\hat{y}_k$). Consequently, the bias should be treated as a constant but unknown quantity using (3.17), thus resulting in the unbiased estimation uncertainty of Figure 3.19, solid line. In the next section, this phenomenon is additionally highlighted in the experiments.

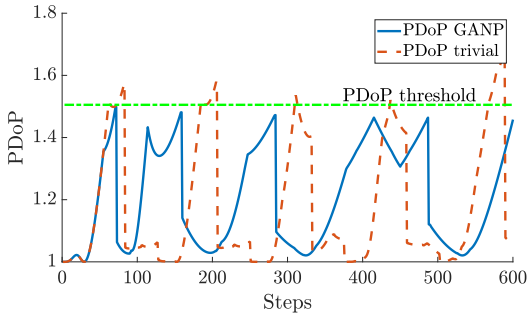

FIGURE 3.18: PDoP evolution along the simulations in Figure 3.17-(a) (GANP) and Figure 3.17-(b) (trivial), respectively.

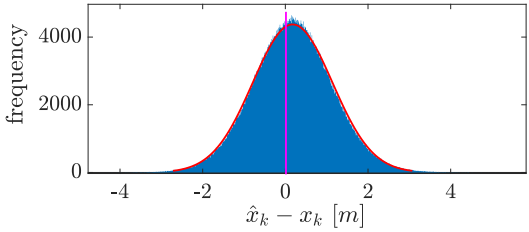

FIGURE 3.19: Monte Carlo trials for the placement problem. When the placement error δ_i is treated as a random variable, a bias of about 15 cm is induced (dashed line), while if it is treated as an unknown but constant quantity estimated through (3.17) (solid line), the estimator is practically unbiased (bias around 1 mm).

Experimental results

To test the algorithm on an actual set-up, we first characterise the UWB anchors at disposal. To this end, we carried out a Type A analysis [208], collecting at first repeated ranging measurements from known distances, i.e., at 1, 3 and 7 meters. As an example, the histogram of the ranging measurements $\bar{\rho}_{i,k}$ in (3.10) collected from an UWB anchor Decawave DWM1001 at a distance of 3 m is reported for reference in Figure 3.20-a. Figure 3.20-b reports the histogram of the error on the position. Albeit all the available anchors behave similarly and with a relatively small variance σ_ρ^2, they all exhibit an approximately linear dependency on the actual distance $\rho_{i,k}$, as

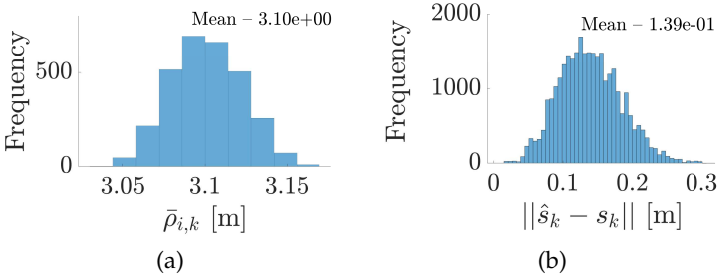

FIGURE 3.20: (a) Characterisation of the ranging measurements $\bar{\rho}_{i,k}$ by means of an histogram obtained with 3000 consecutive measurements (b) Histogram of positioning error with 30000 consecutive measurements

TABLE 3.4: Characterisation of bias and standard deviation of the ranging measurements

$\rho_{i,k}$ [m]	Bias [m]	σ_ρ [m]
1	0.06	0.029
3	0.10	0.0231
7	0.18	0.16

reported in Table 3.4 for the three sampled distances. We may noticed a slight increase of the bias and of the standard deviation σ_ρ, which can be compensated with a simple linear fitting model. Since we do not have a large arena to test the system, we test the GANP placement algorithm forcing the anchors to be closed to each other by selecting $p^m = 2$ to be above the minimum PDoP value obtained for the known first four anchors, which was $g(\mathcal{D}_k(s_0), s_0) = 1.1$ ($\mathcal{D}_k(s_0) = \{a_1, \ldots, a_4\}$ in Figure 3.21-(a)). As stated previously, once the new anchor has been deployed in position a_5 and due to the positioning uncertainty of the UAV, the robot actually believes that the anchor is in $\hat{a}_5$ (Figure 3.21-(a)). After the placement, the UAV comes back to the exploration path (solid line in Figure 3.21-(a)) and, as described in Section 3.2.3, it stores three consecutive estimated positions, namely $\hat{s}_k$, $\hat{s}_{k+1}$ and $\hat{s}_{k+2}$, which actually corresponds to the ideal values to be reached s_k, s_{k+1} and s_{k+2} (see Figure 3.21-(a) for reference). To estimate the bias δ_5, the robot collects 10 consecutive ranging measurements

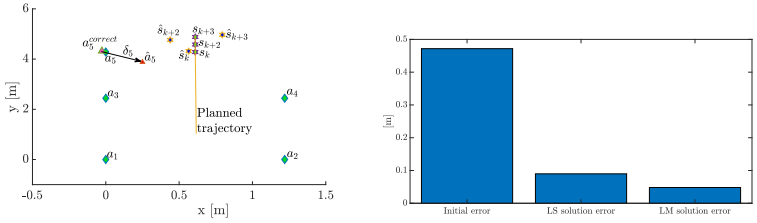

(a) (b)

FIGURE 3.21: (a) Experimental results for the bias δ_5 compensation; (b) Comparison between the LM and the LS solution to (3.17) with respect to the initial deployment error.

$\overline{\rho}_{5,k}$ from position s_k and then compute the average. The process is then repeated from s_{k+1} and s_{k+2}. The solution to (3.17) is then obtained using the Levenberg-Marquardt (LM) algorithm applied to the averages, thus obtaining the corrected location $a_5^{correct}$ of Figure 3.21-(a), exhibiting a far reduced bias compared to $\hat{a}_5$. The method thus described has been compared with a linearized least square (LS) solution to (3.17) on such experimental data, which results in the comparison of Figure 3.21-(b). Of course the iterative and incrementally precise approach of LM gives better results than LS for the bias estimation. Similarly, LM performs better of LS also for the standard positioning problem using multilateration. However, since the algorithm can be executed on board the vehicle and with constrained resources, the LM should be adopted with parsimony (its computation times is about 40 times compared to a linearized LS). As a consequence, we decided to keep the LM solution uniquely for the bias estimation problem.

3.3 Roaming the Red Planet: Revolutionizing Mars Exploration with Dynamic Mobile Infrastructure

So far, we've discussed two contrasting approaches for positioning systems. One relies on a relative approach, where the target's movement generates an attractor point for the robot. This method utilizes an infrastructure mounted on the robot for trilaterating the moving target. The second approach involves robots extending an initial infrastructure based

on their requirements of navigation. By combining these approaches, an innovative system can emerge. Here, a moving infrastructure of anchors localizes itself while simultaneously supplying information to other nodes in need of positioning services. This advancement pushes the boundaries of positioning systems, introducing the first solution capable of offering scalability, flexibility, and on-the-spot positioning services simultaneously. This section presents notable advancements in the challenging domain of exploration, particularly in planetary exploration. These contributions include: i) Design of a distributed algorithm for Unmanned Aerial Vehicles (UAVs) cooperative localisation; ii) Establishing a positioning framework capable of accommodating multiple robots with unrestricted scalability; iii) Analysis of the uncertainties involved in the process and their experimental validation.

3.3.1 Background and Problem Formulation

The problem tackled with this contribution is to provide a (mobile) localisation infrastructure to a set of ground entities using ranging measurements. The first step to solve is to find the coordinates of a set of q UAVs distributed in a certain area, representing the team of q robots forming the localisation infrastructure. In this work, we are considering the robots moving at known heights by the presence of, e.g., a barometer or a sonar (this limitation allows a clearer description of the method and will be removed as a future work). Hence, we can describe the i-th UAV by its unknown Cartesian planar coordinates (x_i, y_i), thus having the team matrix representation

$$X = \begin{bmatrix} \mathbf{p}_1 & \dots & \mathbf{p}_q \end{bmatrix} = \begin{bmatrix} x_1 & \dots & x_q \\ y_1 & \dots & y_q \end{bmatrix}. \tag{3.18}$$

Let us assume that the i-th UAV is able to collect a measurement about the distance to the j-th UAV, i.e.

$$\rho_{i,j} = \sqrt{(x_i - x_j)^2 + (y_i - y_j)^2}, \tag{3.19}$$

so that the symmetric squared Euclidean distance matrix

$$D = \begin{bmatrix} 0 & \rho_{1,2}^2 & \cdots & \rho_{1,q}^2 \\ \rho_{2,1}^2 & 0 & \cdots & \rho_{2,q}^2 \\ \vdots & \vdots & \ddots & \vdots \\ \rho_{q,1}^2 & \rho_{q,2}^2 & \cdots & 0 \end{bmatrix} \tag{3.20}$$

can be computed. Defining H as the double centring matrix, i.e., $H = I_q - \frac{e\, e^T}{q}$, where $e\, e^T = \mathbf{1}_q \times \mathbf{1}_q^T$, $\mathbf{1}_q$ is a column vector with q ones and I_q is the identity matrix of dimension $q \times q$, it follows that

$$G = -\frac{1}{2} HDH = HX^T XH. \tag{3.21}$$

From (3.21), we can retrieve the matrix $\hat{X}$ (i.e., the estimates of X in (3.18)), up to a roto-translation transformation, as the solution of the optimisation problem

$$\arg\min_X \|G - \hat{X}\hat{X}^T\|^2. \tag{3.22}$$

The solution to (3.22) is given by the eigen-decomposition of (3.21), that is $\hat{X} = U\sqrt{V}$, where V and U are the eigenvalues diagonal matrix and the eigenvector matrix of G, respectively. As aforementioned, the points $\hat{X}$ are affine transformations of the original set X, i.e., both verifying the Euclidean distance matrix D. More precisely, there may exists an angle $\theta \neq 2k\pi$ with $k \in \mathbb{N}$ such that

$$X = \begin{bmatrix} \cos\theta & -\sin\theta \\ \sin\theta & \cos\theta \end{bmatrix} \hat{X} = R(\theta)\hat{X}, \tag{3.23}$$

which corresponds to a rotation ambiguity occurs. Moreover, there may also exists a flipping problem, i.e.

$$X = \alpha \begin{bmatrix} -1 & 0 \\ 0 & 1 \end{bmatrix} \hat{X} = \alpha A \hat{X}, \tag{3.24}$$

where $\alpha \in \{-1, 1\}$.

Problem formulation and solution overview

Given, $\forall i = 1, \ldots, q$, the ranging measurements

$$\tilde{\rho}_{i,j} = \rho_{i,j} + \epsilon_{i,j}, \tag{3.25}$$

where $\rho_{i,j}$ is given in (3.19) and $\epsilon_{i,j}$ is the ranging uncertainty, we want to estimate the location of all the nodes X in a local reference frame centred in one agent, say $\mathbf{p}_1$. Moreover, we assume that the team of q robots is split in two groups: n robots moves in the environment, whereas $m = q - n$ are standing in a hovering position to give precise references to the n moving robots. The n robots act as a moving infrastructure meant to localise the set of entities moving on the ground, while the m hovering robots act similarly as a fixed infrastructure. It is worthwhile to note that moving the entire group would increase the uncertainty on their location, which propagates on the uncertainty of the localised ground entities; on the other hand, letting all the q robots to stand still, will inevitably degrade the ranging measurements when the ground vehicles are too far apart. With the proposed approach, instead, the n and m groups alternate their motions to keep track of the ground entities.

In order to tackle this problem, we first need to continuously keep track of the relative positions of the q robots of the localisation infrastructure. Therefore, we first use the solution provided in [187] that derives an estimate $\hat{X}$as the solution of the minimisation problem (3.22), and then, solves for the ambiguity given in $R(\theta)$ and $\alpha \in \{-1, 1\}$ such that

$$\hat{X} = [\hat{\mathbf{p}}_1, \ldots, \hat{\mathbf{p}}_q] = R(\theta)\alpha AX. \tag{3.26}$$

It is worthwhile to note that the only assumption to apply the solution in [187] is that only one agent moves at the beginning and that its turning direction is known (clockwise and counter-clockwise rotations). Notably, these assumptions are necessary and sufficient to solve the problem: hence, from this point on we assume that the estimates $\hat{X}$ are without the rotational (3.23) and flipping (3.24) ambiguities when the algorithm starts. Therefore, once a first guess $\hat{X}$ is available, we adopt the recursive updating

of the UAVs positions using [186], which is a cooperative and uncertainty-aware adaptation of the MDS. More in depth, by computing the difference between the ranging measurements $\tilde{\rho}_{i,j}$ and its estimated quantity $\hat{\rho}_{i,j}$ computed from $\hat{X}$ using (3.19), we compute the *innovation*, as usually called in filtering theory. Moreover, by defining the weights $w_{i,j}$ and γ_i modulating the innovation and the prior knowledge regarding the position of the i–th node, respectively (more on this in Section 3.3.3), we define the following cost function to be minimised

$$S_i = 2\sum_{i=1}^{n}\sum_{j=i}^{n+m} w_{i,j}(\tilde{\rho}_{i,j} - \hat{\rho}_{i,j})^2 + \sum_{i=1}^{n}\gamma_i\|\mathbf{p}_i^\star - \hat{\mathbf{p}}_i\|^2, \tag{3.27}$$

where n is the number of moving robots, m is the number of hovering robots and $\mathbf{p}_i^\star$ is the solution for the i-th agent minimising (3.27). Starting from the solution provided in [186], which minimises a cost function similar to (3.27) for a fixed infrastructure, we use a similar approach to provide a distributed system that retrieves (without ambiguity) all the positions of the members of the team of UAVs and continuously updates their positions based on relative ranging measurements despite of the motions of the agents inside the team. Since, the team of UAVs acts as a localisation infrastructure for the ground entities and, thus, to scale-up the number of ground entities localised with desired position uncertainty, our solution, as presented in [188], introduces a distributed system where information is stored directly on each entity to be localised. This unique feature let each agent to independently select the appropriate update rate for its purposes, regardless of the number of entities accessing the position information, while guaranteeing the desired level of position uncertainty.

3.3.2 Infrastructure Positioning

The algorithm presented next is conceived for the infrastructure distributed position estimates. More precisely, assuming that the UAVs exchange the distance informations, i.e., builds up the matrix D in (3.20), every δ_t seconds, the infrastructure positioning algorithm is executed at each time $l\delta_t$, where $l = 1, 2, \ldots$. At the initial time $l = 0$, we assume an initial guess $\hat{X}_0$ given

the solution provided in [187]. For the generic time instant $l\delta_t$, we are interested to estimate the positions $\hat{X}_l$ using the measurements $\tilde{\rho}_{i,j,l}$ (3.25) and the prior estimates at time $\hat{X}_{l-1}$. We consider that the ranging uncertainties in (3.25) are given by $\epsilon_{i,j} \sim \mathcal{N}(\mu_\rho, \sigma_\rho^2)$, determined with a Type A analysis [209]. For notation simplicity, we drop the explicit reference to the time $l\delta_t$ and we denote the prior estimates with $\hat{X}^{(0)}$, i.e., $\hat{\mathbf{p}}_i^{(0)}$, $\forall i = 1, \ldots, q$, the prior distances with $\hat{\rho}_{i,j}^{(0)}$ and the measurements available at time $l\delta_t$ with $\tilde{\rho}_{i,j}$. Moreover, since we are searching for an iterative solution to minimise a cost function inspired by (3.27), we denote with $\hat{X}^{(k)}$, i.e., $\hat{\mathbf{p}}_i^{(k)}$, $\forall i = 1, \ldots, q$, the position and the distance $\hat{\rho}_{i,j}^{(k)}$ estimates, respectively, available at the k-th iteration of the iterative algorithm.

Hence, for the generic k-th step of the algorithm, we assume that all the UAVs are in line-of-sight, hence they can measure the distances between each other, which accounts to have non-negative values for the weights $w_{i,j} = 1/\sigma_\rho^2$ in (3.27). Without loss of generality, we have that $w_{i,j} = w_{j,i}$ (bidirectional communication link) and $w_{i,i} = 0$ (no self-distance measured). It is worthwhile to note that the i-th UAV has access only to the measurements it is able to collect, that is it only know the components of the i-th row of the matrix D in (3.20), thus making evident the distributed nature of the proposed solution. Therefore, we can rewrite (3.27) for the i-th moving UAVs among the n available as

$$\begin{aligned} S_i^{(k)} = &\sum_{j=1}^{n} w_{i,j}(\tilde{\rho}_{i,j} - \hat{\rho}_{i,j}^{(k)})^2 + \\ &+ \sum_{j=n+1}^{n+m} 2w_{i,j}(\tilde{\rho}_{i,j} - \hat{\rho}_{i,j}^{(k)})^2 + \gamma_i \|\mathbf{p}_i^{(k)} - \hat{\mathbf{p}}_i^{(0)}\|^2. \end{aligned} \tag{3.28}$$

Since each UAV computes its estimation steps independently, we assume that when the best estimate has been reached, the estimated positions are transmitted to the other agents, in order to have the same $\hat{X}^{(0)}$ for all the UAVs for the next iteration step of the algorithm. The iterative minimisation step of (3.28) is based on a quadratic upper-bounding function [210], which

leads to the following position update rule

$$\mathbf{p}_i^{(k+1)} = \frac{1}{a_i}(\gamma_i \hat{\mathbf{p}}_i^{(0)} + X^{(k)} \mathbf{b}_i^{(k)}), \tag{3.29}$$

where

$$a_i = \sum_{j=1, j\neq i}^{n} w_{i,j} + \sum_{j=n+1}^{q} 2w_{i,j} + \gamma_i, \tag{3.30}$$

and $\mathbf{b}_i^{(k)} = [b_1^{(k)}, \ldots, b_q^{(k)}]^T$ is a column vector whose entries are

$$\begin{aligned} b_i^{(k)} &= \sum_{j=1, j\neq i}^{n} w_{i,j} \frac{\tilde{\rho}_{i,j}}{\hat{\rho}_{i,j}^{(k)}} + \sum_{j=n+1}^{m} 2w_{i,j} \frac{\tilde{\rho}_{i,j}}{\hat{\rho}_{i,j}^{(k)}}, \\ b_j^{(k)} &= w_{i,j} \left(1 - \frac{\tilde{\rho}_{i,j}}{\hat{\rho}_{i,j}^{(k)}}\right), \text{ if } j \leq n \text{ and } j \neq i, \\ b_j^{(k)} &= 2w_{i,j} \left(1 - \frac{\tilde{\rho}_{i,j}}{\hat{\rho}_{i,j}^{(k)}}\right), \text{ if } j \geq n. \end{aligned} \tag{3.31}$$

Notice that now the role of γ_i is clear: when γ_i gets larger, the solution to (3.29) tends to be closer to the provided prior information $\hat{\mathbf{p}}_i^{(0)}$. The algorithm terminates when the accumulated cost function for the i-th agent (3.28), i.e., $S_{a,i}^{(k)} = \sum_{j=0}^{k} S_i^{(j)}$, tends towards a limiting, steady state value, i.e., when $|S_{a,i}^{(k)} - S_{a,i}^{(k-1)}| \leq \Delta$, where Δ is a stopping criterion. The entire algorithm thus described is depicted in Figure 3.22. We finally highlights that the position estimates for the m robots that are hovering is not updated using the same algorithm, since they are assumed to have accurate enough information (more on this aspect in the experimental analysis).

3.3.3 Results

This section presents the preliminary experimental results that prove the effectiveness of the proposed solution. The assessment is carried out in two stages: an evaluation of the positioning uncertainties on the ground entities obtained perturbating the infrastructural UAVs positions and an analysis of the uncertainties of the entire positioning framework.

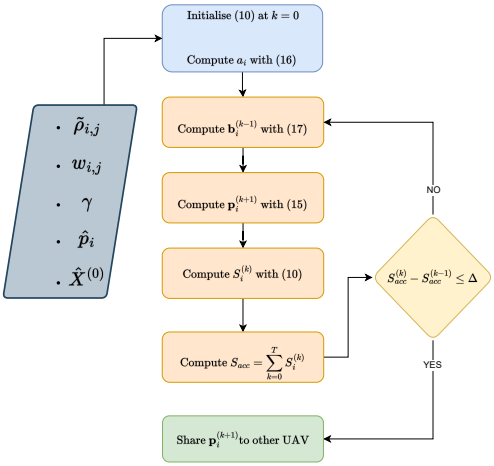

FIGURE 3.22: Flowchart of the cooperative positioning algorithm.

Uncertainties evaluation

As mentioned, the position of the q UAVs is obtained through cooperative collection of ranging measurements. The uncertainties associated with the ranging measurements $\tilde{\rho}_{i,j}$ in (3.25) propagate through the entire positioning algorithm, affecting the accuracy of the ground entities positions. While the uncertainties of the DTDoA algorithm used to derive the position of the ground entities is extensively discussed in [188], this study analyses the entire chain of the propagation of the uncertainties. As described in Section 3.3.1, the positions of the /uAVs generating the localisation infrastructure are determined by minimisation of (3.28). As such, the knowledge of the infrastructure positions is limited by the precision of this estimation process: henceforth, we consider that the estimates are given by $\hat{\mathbf{p}}_i = \mathbf{p}_i + \eta_i$, where $\eta_i = [\eta_{x_i}, \eta_{y_i}]^T$ denotes the Cartesian uncertainties. Given the complex algorithm adopted for the estimates, a Type A analysis of the uncertainties is conducted, as described in [209]. To empirically assess the accuracy of the proposed system, two Monte Carlo simulations were conducted with 5000 trials each. In both simulations, we adopt $q = 6$ UAVs and the swarm was divided into two equal groups, with $m = 3$ hovering

robots and the other $n = 3$ covering a convex area to follow the ground entity for positioning. Upon reaching a maximum distance between the two groups and related to the hardware constraints, the roles are swapped, with the formerly moving group switching to a hovering condition, while the others moving towards them. It is important to note that the focus of this contribution does not delve into the strategy for swarm control, leaving this aspect for future work. To properly incorporate the different positioning accuracy between the hovering and the manoeuvring UAVs in the minimisation of (3.28) and assuming that the standard deviation for the former group is $\hat{\sigma} = 0.1$, we empirically set $\gamma_i = 1/\hat{\sigma}^2 = 100$, while for the moving group $\gamma_i = 1/(5\hat{\sigma})^2 = 4$. Finally, the stopping criterion for the algorithm has been set empirically to $\Delta = 0.1$.

In the first simulation, we assume that the uncertainties on the infrastructure positions are i.i.d. and generated by a Gaussian process, i.e., $\eta_i \sim \mathcal{N}(M, Q)$. The vector of mean values is assumed to be $M = \mu_\eta [1, 1]^T$, with $\mu_\eta = [0, 500, 1000]$ mm, while the covariance matrix is $Q = \sigma_\eta^2 I_2$, where I_2 is the identity matrix of dimension 2 and $\sigma_\eta = [100, 300, 700, 1500]$ mm. The objective here is to assess the positioning accuracy of one ground entity, whose position is denoted with $\mathbf{p}_T = [x_T, y_T]^T$. By denoting with $\hat{\mathbf{p}}_T = [\hat{x}_T, \hat{y}_T]^T$ the estimated ground entity position, function of both $\hat{\mathbf{p}}_i$, $i = 1, \ldots, q$, and the uncertainties in the DTDoA, we have $\hat{\mathbf{p}}_T = \mathbf{p}_T + \xi_T$, where ξ_T has mean values $[\mu_{p_{T_x}}, \mu_{p_{T_y}}]^T$ and variances $\sigma^2_{p_{T_x}}$ and $\sigma^2_{p_{T_y}}$ along the X_w and Y_w reference axes, respectively.

In the second set of Monte Carlo simulations, we are instead acting on the ranging uncertainties $\eta_{i,j}$ in (3.25), again assumed to be generated by an i.i.d. Gaussian process with parameters $\mu_\rho = [0, 500]$ mm and $\sigma_\rho = [100, 500]$ mm. In this second analysis, both the position uncertainties of the different UAVs as well as the position of the ground entity are computed.

The results for the two Monte Carlo simulations are summarised in Table 3.5. The subsystem responsible for estimating $\hat{\mathbf{p}}_T$, operating locally on each agent, is significantly influenced by the statistical characteristics of the UAVs position estimation uncertainty η_i, with an almost linear dependency. As expected, a bias in the UAVs position induces an equivalent bias in

TABLE 3.5: Monte Carlo simulations results. Both the first (uncertainties in the positioning of the infrastructure) and the second (uncertainties on the ranging measurements) set of simulations are reported. All the quantities are reported in millimetres.

First Monte Carlo Simulations: $\hat{\mathbf{p}}_T - \mathbf{p}_T$																
	$\sigma_\eta = 100$				$\sigma_\eta = 300$				$\sigma_\eta = 700$				$\sigma_\eta = 1500$			
	$\mu_{P_{T_x}}$	$\mu_{P_{T_y}}$	$\sigma_{P_{T_x}}$	$\sigma_{P_{T_y}}$	$\mu_{P_{T_x}}$	$\mu_{P_{T_y}}$	$\sigma_{P_{T_x}}$	$\sigma_{P_{T_y}}$	$\mu_{P_{T_x}}$	$\mu_{P_{T_y}}$	$\sigma_{P_{T_x}}$	$\sigma_{P_{T_y}}$	$\mu_{P_{T_x}}$	$\mu_{P_{T_y}}$	$\sigma_{P_{T_x}}$	$\sigma_{P_{T_y}}$
$\mu_\eta = 0$	$\sim \mu_\eta$	$\sim \mu_\eta$	130	150	$\sim \mu_\eta$	$\sim \mu_\eta$	280	420	$\sim \mu_\eta$	$\sim \mu_\eta$	670	970	$\sim \mu_\eta$	$\sim \mu_\eta$	> 1000	> 1000
$\mu_\eta = 500$	$\sim \mu_\eta$	$\sim \mu_\eta$	~ 130	~ 150	$\sim \mu_\eta$	$\sim \mu_\eta$	~ 280	~ 420	$\sim \mu_\eta$	$\sim \mu_\eta$	~ 670	~ 970	$\sim \mu_\eta$	$\sim \mu_\eta$	> 1000	> 1000
$\mu_\eta = 1000$	$\sim \mu_\eta$	$\sim \mu_\eta$	~ 130	~ 150	$\sim \mu_\eta$	$\sim \mu_\eta$	~ 280	~ 420	$\sim \mu_\eta$	$\sim \mu_\eta$	~ 670	~ 970	$\sim \mu_\eta$	$\sim \mu_\eta$	> 1000	> 1000
Second Monte Carlo Simulations: $\hat{\mathbf{p}}_i - \mathbf{p}_i, \forall i = 1, \ldots, 6$ and $\hat{\mathbf{p}}_T - \mathbf{p}_T$																
	$\mu_\rho = 0$								$\mu_\rho = 500$							
	$\sigma_\rho = 100$				$\sigma_\rho = 500$				$\sigma_\rho = 100$				$\sigma_\rho = 500$			
	$\mu_{P_{T_x}}$	$\mu_{P_{T_y}}$	$\sigma_{P_{T_x}}$	$\sigma_{P_{T_y}}$	$\mu_{P_{T_x}}$	$\mu_{P_{T_y}}$	$\sigma_{P_{T_x}}$	$\sigma_{P_{T_y}}$	$\mu_{P_{T_x}}$	$\mu_{P_{T_y}}$	$\sigma_{P_{T_x}}$	$\sigma_{P_{T_y}}$	$\mu_{P_{T_x}}$	$\mu_{P_{T_y}}$	$\sigma_{P_{T_x}}$	$\sigma_{P_{T_y}}$
$\hat{\mathbf{p}}_1 - \mathbf{p}_1$	<50	<50	270	170	<50	<50	>1000	800	340	430	270	170	330	-420	>1000	800
$\hat{\mathbf{p}}_2 - \mathbf{p}_2$	<50	<50	310	120	<50	<50	>1000	600	<50	<50	320	120	<50	-510	>1000	800
$\hat{\mathbf{p}}_3 - \mathbf{p}_3$	<50	<50	260	160	<50	<50	>1000	800	-310	-450	270	160	-280	-450	>1000	830
$\hat{\mathbf{p}}_4 - \mathbf{p}_4$	<50	<50	210	150	>1000	300	800	>1000	230	<50	210	150	300	-240	>1000	860
$\hat{\mathbf{p}}_5 - \mathbf{p}_5$	<50	<50	240	120	-550	-70	>1000	600	230	<50	230	120	610	220	>1000	630
$\hat{\mathbf{p}}_6 - \mathbf{p}_6$	<50	<50	200	150	170	200	>1000	700	210	<50	240	150	270	800	>1000	800
$\hat{\mathbf{p}}_T - \mathbf{p}_T$	-140	-54	300	290	-400	<50	>1000	900	200	-250	640	390	<50	-450	>1000	950

the final estimation of the ground entity, while it is not affecting the precision. Instead, the uncertainties in the ranging measurements have a higher impact on both the positions of the UAVs and the position of the ground entity, while the bias in the ranging exhibits a similar behaviour of the previous case. However, even in the worst-case scenario with parameters $\mu_\rho = \sigma_\rho = 500$ mm, the estimation precision is sufficiently accurate for outdoor navigation purposes and, notably, greater than a standard commercial GNSS module. This postive effect comes from the switching behavior between the moving and the hovering UAVs roles, even though a more in depth ablation study will be performed in the future work. Nevertheless, it is evident how the hovering UAVs continuously accumulate observations about their relative positions, leading to the computation of an ever increasing accurate and precise position. This fact is modelled through the introduction of the parameter γ_i, representing the accuracy of prior information. In our case, it quantifies the mean squared error between the node's mean position and its expected movement, that is a perturbation around the hovering position. Nitce that, following the Bayesian perspective, the influence of γ_i diminishes in the final solution as more measurements are collected.

We finally present a validation with a dynamic ground entity following an eight shaped trajectory (shown in Figure 3.23), where $q = 6$ UAVs are moving along straight trajectories, alternating their role between hovering

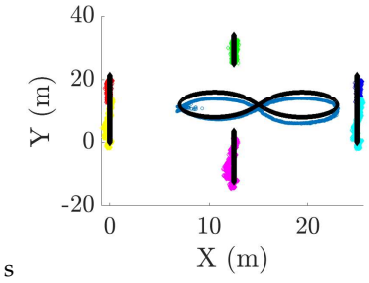

FIGURE 3.23: Dynamic example with a ground entity following an 8-shape trajectory, while the surrounding $q = 6$ UAVs move along straight trajectories and denoted with different colors (the black trajectories denote the actual positions in time).

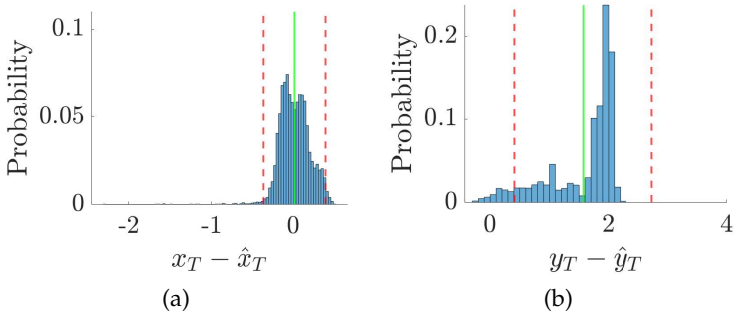

FIGURE 3.24: Distribution of the estimation error in the positions of a moving ground entity, moving according to Figure 3.23, along the X_w (a) and Y_w (b) axes over 5000 repeated measurements.

and manoeuvring. In this case, the estimation error results are reported in Figure 3.24 considering challenging ranging uncertainties of $\mu_\rho = \sigma_\rho = 500$ mm. The results confirm the validity of the proposed approach, while the analysis of the histograms reveals distinct behaviours along the X_w and Y_w axes. This discrepancy is attributed to a geometric issue known as position dilution of precision [3], hence addressing the motion of the UAVs taking into account this issue will be definitely beneficial.

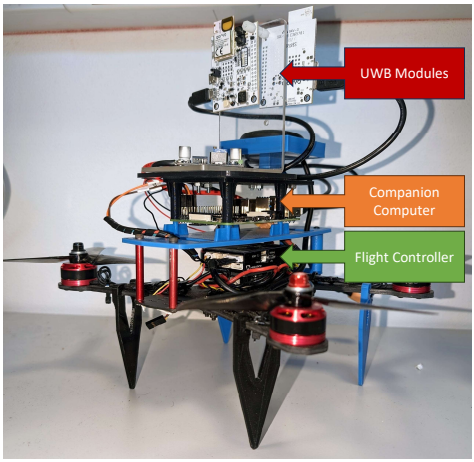

FIGURE 3.25: The UAV prototype

Preliminary Hardware Implementation

Qorvo's latest commercial-off-the-shelf UWB module release provides an opportunity to construct a flexible and robust infrastructure. Operating in accordance with the IEEE *802.15.4z* standard, this transceiver utilizes the new communication channel 9 with a carrier frequency of 7987.2 MHz. The synergy of this channel with the advancements in the developed module significantly enhances ranging estimation precision and accuracy, as detailed in [211]. The proposed system implementation revolves around adopting two DWM3001 modules connected through the serial port to the companion board of the UAVs. Precisely, one module is configured to operate on channel 5 for data transmission to ground entities, providing the positioning service. Simultaneously, the second module is configured on channel 9 to serve as a ranging module among the UAVs. The UAV computes its position on-board, and this computed position is appended to the message payload for the second module. Consequently, during transmission to the ground, the message includes not only the timestamp, as in our previous work, but also the updated position of the infrastructure nodes. The preliminary prototype of the UAV is shown in Figure 3.25.

Chapter 4

Conclusion

In this comprehensive thesis, a multifaceted exploration of ultrawide-band technology has been undertaken to address diverse challenges in localization systems. The work begins by introducing an inexpensive and anonymous contact tracing technology tailored for industrial environments amidst the COVID-19 pandemic. This innovative solution combines ultra-wideband positioning, Bluetooth low-energy, and inertial measurement units, offering not only real-time risk detection, but become an innovative tool for workplace assessment capabilities.

The subsequent sections delve into relative positioning systems, device-free localization, UWB bistatic radar sensors, and UAV-based tracking. Each section presents novel methodologies and hardware implementations, showcasing promising results such as mean RMSE position errors below 20 cm, efficient tracking speeds, and successful deployment scenarios. The work also addresses key challenges in scalability, uncertainties, and dynamic environments, demonstrating a commitment to practical and effective solutions.

Furthermore, the thesis explores groundbreaking approaches in deploying UWB infrastructure through self-deployable robots and cooperative positioning schemes utilizing a swarm of UAVs. These advancements extend the applicability of localization systems to challenging scenarios where traditional infrastructures are impractical.

The work not only contributes novel algorithms, hardware designs, and methodologies but also highlights the potential for future extensions and advancements. The proposed solutions exhibit versatility, cost-effectiveness, and scalability, opening new possibilities for applications in security, logistics, IoT services, and even space exploration.

In conclusion, this thesis represents a significant contribution to the field of localization systems, offering a diverse set of solutions to address real-world challenges. The innovative technologies presented herein pave the way for further research and applications, marking a substantial step forward in enhancing the capabilities of localization systems across various domains.

Bibliography

[1] A. K. Melikov, Z. T. Ai, and D. G. Markov. "Intermittent occupancy combined with ventilation: An efficient strategy for the reduction of airborne transmission indoors". In: *The Science of the total environment* 744 (Nov. 2020), pp. 140908–140908.

[2] Rifqi Rafifandi et al. "Leader–follower formation control of two quadrotor UAVs". In: *SN Applied Sciences* 1.6 (May 2019), p. 539. ISSN: 2523-3971. DOI: 10.1007/s42452-019-0551-z. URL: https://doi.org/10.1007/s42452-019-0551-z.

[3] D. Fontanelli, F. Shamsfakhr, and L. Palopoli. "Cramer-Rao Lower Bound Attainment in Range-only Positioning using Geometry: The G-WLS". In: *IEEE Trans. on Instrumentation and Measurement* 70 (Oct. 2021). Early Access, pp. 1–14. ISSN: 0018-9456. DOI: 10.1109/TIM.2021.3122521.

[4] Javier Díez-González et al. "Local Wireless Sensor Networks Positioning Reliability Under Sensor Failure". In: *Sensors* 20.5 (2020). ISSN: 1424-8220.

[5] Ala' Darabseh et al. "On ADS-B Sensor Placement for Secure Wide-Area Multilateration". In: *Proceedings* 59.1 (2020). ISSN: 2504-3900.

[6] Gaoang Feng et al. "GDOP index in UWB indoor location system experiment". In: *2015 IEEE SENSORS*. 2015, pp. 1–4. DOI: 10.1109/ICSENS.2015.7370254.

[7] Haosheng Huang and Georg Gartner. "A Survey of Mobile Indoor Navigation Systems". In: Jan. 2010, pp. 305–319. ISBN: 978-3-642-03293-6. DOI: 10.1007/978-3-642-03294-3_20.

[8] Yanying Gu, Anthony Lo, and Ignas Niemegeers. "A Survey of Indoor Positioning Systems for Wireless Personal Networks". In:

IEEE COMMUNICATIONS SURVEYS AND TUTORIALS 11.1 (2009), pp. 13–32. DOI: 10.1109/SURV.2009.090103.

[9] Gints Jekabsons, Vadim Kairish, and Vadim Zuravlyov. "An Analysis of Wi-Fi Based Indoor Positioning Accuracy." In: *Computer Science (1407-7493)* 47 (2011).

[10] Mostafa Abdel-Aleem, Shawki Shaaban, and Moustafa Aly. "Ultra Wideband Systems and Modulation Techniques Using Different Gaussian Monopulse Waveforms". In: Sept. 2006, pp. 38–38. ISBN: 0-7695-2911-9. DOI: 10.1109/ICIMP.2007.31.

[11] Rainer Mautz. "Indoor positioning technologies". In: (2012).

[12] JD Shi. "The Challenges of Indoor Positioning". In: *National University of Singapore: Singapore* (2013).

[13] Hui Liu et al. "Survey of wireless indoor positioning techniques and systems". In: *IEEE TRANSACTIONS ON SYSTEMS MAN AND CYBERNETICS PART C-APPLICATIONS AND REVIEWS* 37.6 (Nov. 2007), pp. 1067–1080. ISSN: 1094-6977. DOI: 10.1109/TSMCC.2007.905750.

[14] Klaithem Al Nuaimi and Hesham Kamel. "A survey of indoor positioning systems and algorithms". In: *2011 international conference on innovations in information technology*. IEEE. 2011, pp. 185–190.

[15] Jeffrey Hightower and Gaetano Borriello. "Location sensing techniques". In: *IEEE Computer* 34.8 (2001), pp. 57–66.

[16] Ernesto Martín Gorostiza et al. "Infrared sensor system for mobile-robot positioning in intelligent spaces". In: *Sensors* 11.5 (2011), pp. 5416–5438.

[17] E Brassart, C Pegard, and M Mouaddib. "Localization using infrared beacons". In: *ROBOTICA* 18.2 (Mar. 2000), pp. 153–161. ISSN: 0263-5747. DOI: 10.1017/S0263574799001927.

[18] E Aitenbichler and M Mühlhäuser. "An IR local positioning system for smart items and devices". In: *23RD INTERNATIONAL CONFERENCE ON DISTRIBUTED COMPUTING SYSTEMS WORKSHOPS*. Ed. by FM Titsworth. 23rd International Conference on Distributed Computing Systems Workshops, PROVIDENCE, RI, MAY 19-22, 2003. IEEE Comp Soc. 2003, pp. 334–339. ISBN: 0-7695-1921-0.

[19] Mari Saua Svalastog. “Indoor positioning-technologies, services and architectures”. MA thesis. 2007.

[20] Jacek Rapinski and Michal Smieja. “ZigBee Ranging using Phase Shift Measurements”. In: *JOURNAL OF NAVIGATION* 68.4 (July 2015), pp. 665–677. ISSN: 0373-4633. DOI: 10.1017/S0373463315000028.

[21] Jacek Rapinski. “THE APPLICATION OF ZIGBEE PHASE SHIFT MEASUREMENT IN RANGING”. In: *ACTA GEODYNAMICA ET GEOMATERIALIA* 12.2 (2015), pp. 145–149. ISSN: 1214-9705.

[22] Liang Chen et al. “Carrier Phase Ranging for Indoor Positioning With 5G NR Signals”. In: *IEEE Internet of Things Journal* 9.13 (2022), pp. 10908–10919. DOI: 10.1109/JIOT.2021.3125373.

[23] Stephane Beauregard and Harald Haas. “Pedestrian dead reckoning: A basis for personal positioning”. In: *Proceedings of the 3rd Workshop on Positioning, Navigation and Communication*. 2006, pp. 27–35.

[24] Rosen Ivanov. “Indoor navigation system for visually impaired”. In: *Proceedings of the 11th International Conference on Computer Systems and Technologies and Workshop for PhD Students in Computing on International Conference on Computer Systems and Technologies*. 2010, pp. 143–149.

[25] R. Mautz and S. Tilch. “Survey of optical indoor positioning systems”. In: *Proc. Int. Conference on Indoor Positioning and Indoor Navigation (IPIN)*. 2011, pp. 1–7.

[26] Zhenlong Song, Gangyi Jiang, and Chao Huang. “A Survey on Indoor Positioning Technologies”. In: *THEORETICAL AND MATHEMATICAL FOUNDATIONS OF COMPUTER SCIENCE*. Ed. by QH Zhou. Vol. 164. Communications in Computer and Information Science. 2nd International Conference on Theoretical and Mathematical Foundations of Computer Science (ICTMF 2011), Singapore, MALAYSIA, MAY, 2011. Intelligent Informat Technol Appl Res Assoc; Nanyang Technol Univ; SMU. 2011, pp. 198+. ISBN: 978-3-642-24998-3.

[27] Mohammad Ghavami, Lachlan Michael, and Ryuji Kohno. *Ultra wideband signals and systems in communication engineering*. John Wiley & Sons, 2007.

[28] Guangliang Cheng. "Accurate TOA-Based UWB Localization System in Coal Mine Based on WSN". In: *INTERNATIONAL CONFERENCE ON APPLIED PHYSICS AND INDUSTRIAL ENGINEERING 2012, PT A*. Ed. by D Yang. Vol. 24. Physics Procedia A. International Conference on Applied Physics and Industrial Engineering (ICAPIE), Wuhan, PEOPLES R CHINA, MAR 01-02, 2012. 2012, pp. 534–540. DOI: 10.1016/j.phpro.2012.02.078.

[29] Kazimierz Siwiak and Debra McKeown. *Ultra-wideband radio technology*. John Wiley & Sons, 2004.

[30] Arash Shahi et al. "Deterioration of UWB positioning during construction". In: *AUTOMATION IN CONSTRUCTION* 24 (July 2012), pp. 72–80. ISSN: 0926-5805. DOI: 10.1016/j.autcon.2012.02.009.

[31] M Segura, V Mut, and C Sisterna. "Ultra wideband indoor navigation system". In: *IET Radar, Sonar & Navigation* 6.5 (2012), pp. 402–411.

[32] Eva Arias-de Reyna and Umberto Mengali. "A Maximum Likelihood UWB Localization Algorithm Exploiting Knowledge of the Service Area Layout". In: *WIRELESS PERSONAL COMMUNICATIONS* 69.4 (Apr. 2013), pp. 1413–1426. ISSN: 0929-6212. DOI: 10.1007/s11277-012-0642-2.

[33] Sivanand Krishnan et al. "A UWB based localization system for indoor robot navigation". In: *2007 IEEE International Conference on Ultra-Wideband*. IEEE. 2007, pp. 77–82.

[34] Luigi Cirrincione et al. "COVID-19 Pandemic: Prevention and Protection Measures to Be Adopted at the Workplace". In: *Sustainability* 12.9 (2020).

[35] Jonathan W. Dyal. "COVID-19 Among Workers in Meat and Poultry Processing Facilities - 19 States, April 2020." In: *MMWR. Morbidity and mortality weekly report* 69.18 (May 2020).

[36] Jack T. Dennerlein et al. “An Integrative Total Worker Health Framework for Keeping Workers Safe and Healthy During the COVID-19 Pandemic”. In: *Human Factors* 62.5 (2020), pp. 689–696.

[37] Siswoyo Haryono Agung Sedaju and Nurlaila Anisahwati. “Flexible Work Arrangement in Manufacturing during the Covid19 Pandemic: An Evidence-Based Study of Indonesian Employees”. In: *International Journal of Advanced Science and Technology* 29.06 (Apr. 2020), pp. 3914–3924.

[38] Marco Bortolini et al. “Multi-objective assembly line balancing considering component picking and ergonomic risk”. In: *Computers and Industrial Engineering* 112 (2017), pp. 348–367. DOI: 10.1016/j.cie.2017.08.029.

[39] D. Dardari, P. Closas, and P. Djurić. “Indoor Tracking: Theory, Methods, and Technologies”. In: *IEEE Transactions on Vehicular Technology* 64 (2015), pp. 1263–1278.

[40] Maurizio Faccio et al. “Human Factor Analyser for work measurement of manual manufacturing and assembly processes”. In: *The International Journal of Advanced Manufacturing Technology* 103.1 (July 2019), pp. 861–877.

[41] Xiaoyue Hou and Tughrul Arslan. “Monte Carlo localization algorithm for indoor positioning using Bluetooth low energy devices”. In: *2017 International Conference on Localization and GNSS (ICL-GNSS)*. 2017, pp. 1–6.

[42] Syed A. Arif et al. “RSSI Based Trilatertion for Outdoor Localization in Zigbee based Wireless Sensor Networks (WSNs)”. In: *2018 10th International Conference on Computational Intelligence and Communication Networks (CICN)*. 2018, pp. 1–5.

[43] Francesco Guarato, Vanessa Laudan, and James F.C. Windmill. “Ultrasonic sonar system for target localization with one emitter and four receivers: Ultrasonic 3D localization”. In: *2017 IEEE SENSORS*. 2017, pp. 1–3.

[44] Shubham Sharma et al. “Use of Motion Capture in 3D Animation: Motion Capture Systems, Challenges, and Recent Trends”. In: *2019*

International Conference on Machine Learning, Big Data, Cloud and Parallel Computing (COMITCon). 2019, pp. 289–294.

[45] Muhammad Fikri Norazman and Norashikin M. Thamrin. "Landmark scanning by using infrared sensor for simultaneous localization and mapping application". In: *2018 IEEE 14th International Colloquium on Signal Processing Its Applications (CSPA)*. 2018, pp. 145–149.

[46] Shenghong Li et al. "Passive Localization of Standard WiFi Devices". In: *IEEE Systems Journal* 13.4 (2019), pp. 3929–3932.

[47] Alice Buffi and Paolo Nepa. "An RFID-based technique for train localization with passive tags". In: *2017 IEEE International Conference on RFID (RFID)*. 2017, pp. 155–160.

[48] Alwin Poulose et al. "An Accurate Indoor User Position Estimator For Multiple Anchor UWB Localization". In: *2020 International Conference on Information and Communication Technology Convergence (ICTC)*. 2020, pp. 478–482.

[49] Yuval Cohen et al. "Assembly systems in Industry 4.0 era: a road map to understand Assembly 4.0". In: *International Journal of Advanced Manufacturing Technology* 105.9 (Dec. 2019), pp. 4037–4054.

[50] Farouq Halawa et al. "Introduction of a real time location system to enhance the warehouse safety and operational efficiency". In: *International Journal of Production Economics* 224 (June 2020).

[51] Sourour Trab et al. "Product allocation planning with safety compatibility constraints in IoT-based warehouse". In: *Procedia Computer Science* 73 (2015), pp. 290–297.

[52] S. Gezici et al. "Localization via ultra-wideband radios: a look at positioning aspects for future sensor networks". In: *IEEE Signal Processing Magazine* 22.4 (2005), pp. 70–84.

[53] Chun-Hung Cheng, Yong-Hong Kuo, and Ziye Zhou. "Tracking Nosocomial Diseases at Individual Level with a Real-Time Indoor Positioning System". In: *Journal of Medical Systems* 42.11 (Oct. 2018), p. 222.

[54] Hanley J. Ho et al. "Use of a Real-Time Locating System for Contact Tracing of Health Care Workers During the COVID-19 Pandemic

at an Infectious Disease Center in Singapore: Validation Study". In: *Journal of medical Internet research* 22.5 (May 2020), e19437–e19437.

[55] T. Alanzi. "A Review of Mobile Applications Available in the App and Google Play Stores Used During the COVID-19 Outbreak". In: *J Multidiscip Healthc* 14 (2021), pp. 45–57.

[56] Timofei Istomin et al. *Janus: Efficient and Accurate Dual-radio Social Contact Detection*. 2021. arXiv: 2101.01514 [cs.NI].

[57] Yuan Zhang et al. "Ubiquitous WSN for Healthcare: Recent Advances and Future Prospects". In: *IEEE Internet of Things Journal* 1.4 (2014), pp. 311–318. DOI: 10.1109/JIOT.2014.2329462.

[58] Andres L. Bleda et al. "Smart Sensory Furniture Based on WSN for Ambient Assisted Living". In: *IEEE Sensors Journal* 17.17 (2017), pp. 5626–5636. DOI: 10.1109/JSEN.2017.2721434.

[59] Stefano Melzi, Luca Pietro Borsani, and Matteo Cesana. "The Virtual Trainer: Supervising Movements Through a Wearable Wireless Sensor Network". In: *2009 6th IEEE Annual Communications Society Conference on Sensor, Mesh and Ad Hoc Communications and Networks Workshops*. 2009, pp. 1–3. DOI: 10.1109/SAHCNW.2009.5172966.

[60] Daniel Ramsauer et al. "Human Perception and Building Automation Systems". In: *Energies* 15.5 (2022). ISSN: 1996-1073. DOI: 10.3390/en15051745. URL: https://www.mdpi.com/1996-1073/15/5/1745.

[61] F. Viani et al. "WSN-based solutions for security and surveillance". In: *The 40th European Microwave Conference*. 2010, pp. 1762–1765. DOI: 10.23919/EUMC.2010.5616285.

[62] Deborah A. Kuban et al. "Ultrasound-Based Localization". In: *Seminars in Radiation Oncology* 15.3 (2005), pp. 180–191. ISSN: 1053-4296. DOI: https://doi.org/10.1016/j.semradonc.2005.01.009. URL: https://www.sciencedirect.com/science/article/pii/S1053429605000111.

[63] Panarat Cherntanomwong and Wisarut Chantharasena. "Indoor localization system using visible light communication". In: *2015 7th International Conference on Information Technology and Electrical*

Engineering (ICITEE). 2015, pp. 480–483. DOI: 10.1109/ICITEED.2015.7408994.

[64] Heng Fan and Zhongmin Chen. "WiFi based indoor localization with multiple kernel learning". In: *2016 8th IEEE International Conference on Communication Software and Networks (ICCSN)*. 2016, pp. 474–477. DOI: 10.1109/ICCSN.2016.7587204.

[65] Matteo Nardello et al. "Preventing COVID-19 contagion in industrial environments through anonymous contact tracing". In: *2021 IEEE International Workshop on Metrology for Industry 4.0 & IoT (MetroInd4.0&IoT)*. 2021, pp. 99–104. DOI: 10.1109/MetroInd4.0IoT51437.2021.9488522.

[66] Luca Santoro et al. "Scale up to infinity: the UWB Indoor Global Positioning System". In: *2021 IEEE International Symposium on Robotic and Sensors Environments (ROSE) Proceedings*. IEEE, 2021, pp. 1–8. ISBN: 978-1-6654-4062-2.

[67] L. Santoro, D. Brunelli, and D. Fontanelli. "On-line Optimal Ranging Sensor Deployment for Robotic Exploration". In: *IEEE Sensors Journal* 22.6 (Mar. 2022), pp. 5417–5426. ISSN: 1530-437X. DOI: 10.1109/JSEN.2021.3120889.

[68] Maria Doglioni et al. "Cost-effective bistatic radar with ultrawideband radio". In: *2022 IEEE International Workshop on Metrology for Industry 4.0 and IoT (MetroInd4.0andIoT)*. 2022, pp. 207–211. DOI: 10.1109/MetroInd4.0IoT54413.2022.9831767.

[69] Luca Santoro et al. "Scalable centimetric tracking system for team sports". In: *2022 IEEE International Workshop on Sport, Technology and Research (STAR)*. 2022, pp. 1–6. DOI: 10.1109/STAR53492.2022.9859930.

[70] Rejane Dalce, Adrien van den Bossche, and Thierry Val. "Indoor self-localization in a WSN, based on Time Of Flight: Propositions and demonstrator". In: *International Conference on Indoor Positioning and Indoor Navigation*. 2013, pp. 1–6. DOI: 10.1109/IPIN.2013.6817852.

[71] Mirko Ivanić and Ivan Mezei. "Distance Estimation Based on RSSI Improvements of Orientation Aware Nodes". In: *2018 Zooming Innovation in Consumer Technologies Conference (ZINC)*. 2018, pp. 140–143. DOI: 10.1109/ZINC.2018.8448660.

[72] Carmelo Di Franco et al. "Multidimensional scaling localization with anchors". In: *2017 IEEE International Conference on Autonomous Robot Systems and Competitions (ICARSC)*. 2017, pp. 49–54. DOI: 10.1109/ICARSC.2017.7964051.

[73] Zhiqiang Cao et al. "Relative Localization of Mobile Robots with Multiple Ultra-WideBand Ranging Measurements". In: *2021 IEEE/RSJ International Conference on Intelligent Robots and Systems (IROS)*. 2021, pp. 5857–5863. DOI: 10.1109/IROS51168.2021.9636017.

[74] Yanhui Lv et al. "A Range-Based Distributed Localization Algorithm for Wireless Sensor Networks". In: *2016 3rd International Conference on Information Science and Control Engineering (ICISCE)*. 2016, pp. 1235–1239. DOI: 10.1109/ICISCE.2016.264.

[75] C. De Marziani et al. "Relative localization and mapping combining multidimensional scaling and Levenberg-Marquardt optimization". In: *2009 IEEE International Symposium on Intelligent Signal Processing*. 2009, pp. 43–47. DOI: 10.1109/WISP.2009.5286543.

[76] Jose Maria Cabero et al. "Indoor People Tracking Based on Dynamic Weighted Multidimensional Scaling". In: *Proceedings of the 10th ACM Symposium on Modeling, Analysis, and Simulation of Wireless and Mobile Systems*. MSWiM '07. Association for Computing Machinery, 2007, 328–335. ISBN: 9781595938510. DOI: 10.1145/1298126.1298183. URL: https://doi.org/10.1145/1298126.1298183.

[77] Carmelo Di Franco, Alessandra Melani, and Mauro Marinoni. "Solving ambiguities in MDS relative localization". In: *2015 International Conference on Advanced Robotics (ICAR)*. 2015, pp. 230–236. DOI: 10.1109/ICAR.2015.7251461.

[78] Sandeep Kumar, Raju Kumar, and Ketan Rajawat. "Cooperative Localization of Mobile Networks Via Velocity-Assisted Multidimensional Scaling". In: *IEEE Transactions on Signal Processing* 64.7 (2016), pp. 1744–1758. DOI: 10.1109/TSP.2015.2507548.

[79] Alon Amar, Yiyin Wang, and Geert Leus. "Extending the Classical Multidimensional Scaling Algorithm Given Partial Pairwise Distance Measurements". In: *IEEE Signal Processing Letters* 17.5 (2010), pp. 473–476. DOI: 10.1109/LSP.2010.2043890.

[80] P. Drineas et al. "Distance Matrix Reconstruction from Incomplete Distance Information for Sensor Network Localization". In: *2006 3rd Annual IEEE Communications Society on Sensor and Ad Hoc Communications and Networks*. Vol. 2. 2006, pp. 536–544. DOI: 10.1109/SAHCN.2006.288510.

[81] Yongqiang Han et al. "A Multi - platform Cooperative Localization Method Based on Dead Reckoning and Particle Filtering". In: *2019 Chinese Control Conference (CCC)*. 2019, pp. 4037–4041.

[82] Brian Beck and Robert Baxley. "Anchor free node tracking using ranges, odometry, and multidimensional scaling". In: *2014 IEEE International Conference on Acoustics, Speech and Signal Processing (ICASSP)*. 2014, pp. 2209–2213. DOI: 10.1109/ICASSP.2014.6853991.

[83] Wenchao Li et al. "Cooperative Localization Using Distance Measurements for Mobile Nodes". In: *Sensors* 21.4 (2021). DOI: 10.3390/s21041507.

[84] Huthaifa Obeidat et al. "A of Indoor Localization Techniques and Wireless Technologies". In: *Wireless Personal Communications* 119.1 (July 2021), pp. 289–327. ISSN: 1572-834X. DOI: 10.1007/s11277-021-08209-5. URL: https://doi.org/10.1007/s11277-021-08209-5.

[85] Jayakanth Kunhoth et al. "Indoor positioning and wayfinding systems: a survey". In: *Human-centric Computing and Information Sciences* 10.1 (May 2020), p. 18. ISSN: 2192-1962. DOI: 10.1186/s13673-020-00222-0. URL: https://doi.org/10.1186/s13673-020-00222-0.

[86] Germán Martín Mendoza-Silva, Joaquín Torres-Sospedra, and Joaquín Huerta. "A Meta-Review of Indoor Positioning Systems". In: *Sensors* 19.20 (2019). ISSN: 1424-8220. DOI: 10.3390/s19204507. URL: https://www.mdpi.com/1424-8220/19/20/4507.

[87] Sameera Palipana, Bastien Pietropaoli, and Dirk Pesch. "Recent advances in RF-based passive device-free localisation for indoor applications". In: *Ad Hoc Networks* 64 (2017), pp. 80–98. ISSN: 1570-8705. DOI: https://doi.org/10.1016/j.adhoc.2017.06.007.

[88] Stijn Denis, Rafael Berkvens, and Maarten Weyn. "A Survey on Detection, Tracking and Identification in Radio Frequency-Based Device-Free Localization". In: *Sensors* 19.23 (2019). ISSN: 1424-8220. DOI: 10.3390/s19235329.

[89] Matteo Nardello et al. "Preventing COVID-19 contagion in industrial environments through anonymous contact tracing". In: *2021 IEEE International Workshop on Metrology for Industry 4.0 and IoT: Proceedings*. Institute of Electrical and Electronics Engineers Inc., 2021, pp. 99–104. ISBN: 978-1-6654-1980-2.

[90] Alessandro Luchetti et al. "Human identification and tracking using ultra-wideband-vision data fusion in unstructured environments". In: *ACTA IMEKO* 10 (2021), pp. 124–131.

[91] Fares Alkhawaja, Mohammad Jaradat, and Lotfi Romdhane. "Techniques of Indoor Positioning Systems (IPS): A Survey". In: *2019 Advances in Science and Engineering Technology International Conferences (ASET)*. 2019, pp. 1–8. DOI: 10.1109/ICASET.2019.8714291.

[92] Malith Maheepala, Abbas Z. Kouzani, and Matthew A. Joordens. "Light-Based Indoor Positioning Systems: A Review". In: *IEEE Sensors Journal* 20.8 (2020), pp. 3971–3995. DOI: 10.1109/JSEN.2020.2964380.

[93] Nathaniel Faulkner et al. "Device-Free Localization Using Privacy-Preserving Infrared Signatures Acquired From Thermopiles and Machine Learning". In: *IEEE Access* 9 (2021), pp. 81786–81797. DOI: 10.1109/ACCESS.2021.3086431.

[94] Jiang Xiao et al. "A Survey on Wireless Indoor Localization from the Device Perspective". In: *ACM Comput. Surv.* 49.2 (June 2016). ISSN: 0360-0300. DOI: 10.1145/2933232.

[95] Faheem Ijaz et al. "Indoor positioning: A review of indoor ultrasonic positioning systems". In: *2013 15th International Conference on Advanced Communications Technology (ICACT)*. 2013, pp. 1146–1150.

[96] Pooyan Shams Farahsari et al. "A Survey on Indoor Positioning Systems for IoT-Based Applications". In: *IEEE Internet of Things Journal* 9.10 (2022), pp. 7680–7699. DOI: 10.1109/JIOT.2022.3149048.

[97] Suiyan Geng et al. "Multipath propagation characterization of ultra-wide band indoor radio channels". In: *2005 IEEE International Conference on Ultra-Wideband*. 2005, pp. 11–15. DOI: 10.1109/ICU.2005.1569948.

[98] Anton Ledergerber and Raffaello D'Andrea. "A Multi-Static Radar Network with Ultra-Wideband Radio-Equipped Devices". In: *Sensors (Basel)* 20.6 (Mar. 2020).

[99] Cung Lian Sang et al. "An Analytical Study of Time of Flight Error Estimation in Two-Way Ranging Methods". In: *2018 International Conference on Indoor Positioning and Indoor Navigation (IPIN)*. 2018, pp. 1–8. DOI: 10.1109/IPIN.2018.8533697.

[100] V. Magnago et al. "Robot Localization via Odometry-assisted Ultra-wideband Ranging with Stochastic Guarantees". In: *Proc. IEEE/RSJ International Conference on Intelligent Robots and System (IROS)*. IEEE, Nov. 2019, pp. 1607–1613. DOI: 10.1109/IROS40897.2019.8968019.

[101] Yun Cheng and Taoyun Zhou. "UWB Indoor Positioning Algorithm Based on TDOA Technology". In: *2019 10th International Conference on Information Technology in Medicine and Education (ITME)*. 2019, pp. 777–782. DOI: 10.1109/ITME.2019.00177.

[102] Pablo Corbalán, Gian Pietro Picco, and Sameera Palipana. "Chorus: UWB Concurrent Transmissions for GPS-like Passive Localization of Countless Targets". In: *2019 18th ACM/IEEE International Conference on Information Processing in Sensor Networks (IPSN)*. 2019, pp. 133–144. DOI: 10.1145/3302506.3310395.

[103] Reza Zandian and Ulf Witkowski. "Robot self-localization in ultra-wideband large scale multi-node setups". In: *2017 14th Workshop on Positioning, Navigation and Communications (WPNC)*. 2017, pp. 1–6.

[104] Mathias Pelka and Horst Hellbrück. "S-TDoA – Sequential time difference of arrival – A scalable and synchronization free approach forl Positioning". In: *2016 IEEE Wireless Communications and Networking Conference*. 2016, pp. 1–6. DOI: 10.1109/WCNC.2016.7565024.

[105] K. Yu et al. "A Novel NLOS Mitigation Algorithm for UWB Localization in Harsh Indoor Environments". In: *IEEE Transactions on Vehicular Technology* 68.1 (2019), pp. 686–699.

[106] Xin Li and Fucheng Cao. "Location Based TOA Algorithm for UWB Wireless Body Area Networks". In: *2014 IEEE 12th International Conference on Dependable, Autonomic and Secure Computing*. 2014, pp. 507–511.

[107] J. Tiemann and C. Wietfeld. "Scalability, Real-Time Capabilities, and Energy Efficiency in Ultra-Wideband Localization". In: *IEEE Transactions on Industrial Informatics* 15.12 (2019), pp. 6313–6321.

[108] Huibin Xu and Wang ying. "A linear algorithm based on TDOA technique for UWB localization". In: *2011 International Conference on Electric Information and Control Engineering*. 2011, pp. 1013–1015.

[109] Kan Ngamakeur et al. "A Survey on Device-Free Indoor Localization and Tracking in the Multi-Resident Environment". In: *ACM Comput. Surv.* 53.4 (July 2020). ISSN: 0360-0300. DOI: 10.1145/3396302.

[110] Pietro Cassarà et al. "Choosing an RSS device-free localization algorithm for Ambient Assisted Living". In: *2015 International Conference on Indoor Positioning and Indoor Navigation (IPIN)*. 2015, pp. 1–8. DOI: 10.1109/IPIN.2015.7346788.

[111] Shengxin Xu et al. "Compressive Sensing Based Radio Tomographic Imaging with Spatial Diversity". In: *Sensors* 19.3 (2019). ISSN: 1424-8220. DOI: 10.3390/s19030439. URL: https://www.mdpi.com/1424-8220/19/3/439.

[112] Yubin Luo et al. "A hierarchical RSS model for RF-based device-free localization". In: *Pervasive and Mobile Computing* 31 (2016), pp. 124–

136. ISSN: 1574-1192. DOI: https://doi.org/10.1016/j.pmcj.2016.03.002.

[113] Chenglong Li. "Multi-Static UWB Radar-based Passive Human Tracking Using COTS Devices". In: *IEEE Antennas and Wireless Propagation Letters* PP.4 (Jan. 2022), pp. 1–1. DOI: 10.1109/LAWP.2022.3141869.

[114] Alex Moschevikin et al. "Investigations on passive channel impulse response of ultra wide band signals for monitoring and safety applications". In: *2016 3rd International Symposium on Wireless Systems within the Conferences on Intelligent Data Acquisition and Advanced Computing Systems (IDAACS-SWS)*. 2016, pp. 97–104. DOI: 10.1109/IDAACS-SWS.2016.7805795.

[115] Marco Cimdins, Sven Ole Schmidt, and Horst Hellbrück. "MAMPI – Multipath-assisted Device-free Localization with Magnitude and Phase Information". In: *2020 International Conference on Localization and GNSS (ICL-GNSS)*. 2020, pp. 1–6. DOI: 10.1109/ICL-GNSS49876.2020.9115529.

[116] Josef Kulmer et al. "Using DecaWave UWB transceivers for high-accuracy multipath-assisted indoor positioning". In: *2017 IEEE International Conference on Communications Workshops (ICC Workshops)*. 2017, pp. 1239–1245.

[117] Ju Wang et al. "LiFS: Low Human-Effort, Device-Free Localization with Fine-Grained Subcarrier Information". In: *Proceedings of the 22nd Annual International Conference on Mobile Computing and Networking*. MobiCom '16. Association for Computing Machinery, 2016, 243–256. ISBN: 9781450342261. DOI: 10.1145/2973750.2973776.

[118] Nai-Tong Zhang and Jing Meng. "Reflection Characteristics Analysis of IR-UWB Signal". In: *2008 4th International Conference on Wireless Communications, Networking and Mobile Computing*. 2008, pp. 1–4. DOI: 10.1109/WiCom.2008.265.

[119] Enrico Paolini et al. "Localization Capability of Cooperative Anti-Intruder Radar Systems". In: *EURASIP Journal on Advances in Signal Processing* 2008.1 (Apr. 2008), p. 726854. ISSN: 1687-6180. DOI: 10.1155/2008/726854.

[120] Andreas F. Molisch. "Ultra-Wide-Band Propagation Channels". In: *Proceedings of the IEEE* 97.2 (2009), pp. 353–371. DOI: 10.1109/JPROC.2008.2008836.

[121] Z. Zhaohong. *White paper: Matched-Filter Ultrasonic Sensing: Theory and Implementation*. Tech. rep. SLAA814. Texas Instruments, Dec. 2017.

[122] Yuen-sam Kwok, Francois Chin, and Xiaoming Peng. "Ranging Mechanism, Preamble Generation, and Performance with IEEE 802.15.4a Low-Rate Low-Power UWB Systems". In: *2006 IEEE International Conference on Ultra-Wideband*. 2006, pp. 525–530. DOI: 10.1109/ICU.2006.281604.

[123] Dušan Kocur, Mária Švecová, and Jana Rovňáková. "Through-the-wall localization of a moving target by two independent ultra wideband (UWB) radar systems". In: *Sensors* 13.9 (2013), pp. 11969–11997.

[124] Cheng Xu et al. "Spatial-temporal constrained particle filter for cooperative target tracking". In: *Journal of network and computer applications* 176 (2021), p. 102913.

[125] IEEE 802 Working Group et al. "IEEE standard for local and metropolitan area networks–Part 15.4: Low-rate wireless personal area networks (lr-wpans)". In: *IEEE Std* 802 (2011), pp. 4–2011.

[126] Maria Doglioni et al. "Cost-effective bistatic radar with ultrawideband radio". In: *2022 IEEE International Workshop on Metrology for Industry 4.0 & IoT (MetroInd4. 0&IoT)*. IEEE. 2022, pp. 207–211.

[127] Rahul M. "Review on Motion Capture Technology". In: *Global Journal of Computer Science and Technology* (2018).

[128] D. Fontanelli et al. "A Clock State Estimator for PTP Time Synchronization in Harsh Environmental Conditions". In: *Proc. IEEE Int. Symp. on Precision Clock Synchronization for Measurement, Control and Communication (ISPCS)*. Best Academic Paper Award. Sept. 2011, pp. 99–104. DOI: 10.1109/ISPCS.2011.6070142.

[129] Josef Kulmer et al. "Using DecaWave UWB transceivers for high-accuracy multipath-assisted indoor positioning". In: *2017 IEEE International Conference on Communications Workshops (ICC Workshops)*. 2017, pp. 1239–1245. DOI: 10.1109/ICCW.2017.7962828.

[130] Mikael Frisk and Albin Nilsson. "Inertial sensor and ultra-wideband sensor fusion: Precision positioning of robot platform". PhD thesis. 2014. URL: http://urn.kb.se/resolve?urn=urn:nbn:se:uu:diva-231053.

[131] DecaWave. *DW1000 Data Sheet*. 2016.

[132] Steven M Kay. *Fundamentals of statistical signal processing: estimation theory*. Prentice-Hall, Inc., 1993.

[133] Yang Weng. "Source localization using TDOA measurements with sensor location uncertainty". In: *Proceedings of the 30th Chinese Control Conference*. 2011, pp. 5068–5072.

[134] Reza Zekavat and R Michael Buehrer. *Handbook of position location: Theory, practice and advances*. Vol. 27. John Wiley & Sons, 2011.

[135] Anton Ledergerber and Raffaello D'Andrea. "Ultra-wideband range measurement model with Gaussian processes". In: *2017 IEEE Conference on Control Technology and Applications (CCTA)*. 2017, pp. 1929–1934.

[136] Cung Lian Sang et al. "Numerical and Experimental Evaluation of Error Estimation for Two-Way Ranging Methods". In: *Sensors* 19.3 (2019). DOI: 10.3390/s19030616.

[137] Taha Elmokadem and Andrey V. Savkin. "Towards Fully Autonomous UAVs: A Survey". In: *Sensors* 21.18 (2021). ISSN: 1424-8220. URL: https://www.mdpi.com/1424-8220/21/18/6223.

[138] Jun Tang, Songyang Lao, and Yu Wan. "Systematic Review of Collision-Avoidance Approaches for Unmanned Aerial Vehicles". In: *IEEE Systems Journal* (2021), pp. 1–12. DOI: 10.1109/JSYST.2021.3101283.

[139] Anunay Gupta et al. "Advances of UAVs toward Future Transportation: The State-of-the-Art, Challenges, and Opportunities". In: *Future Transportation* 1.2 (2021), pp. 326–350. ISSN: 2673-7590. DOI:

10.3390/futuretransp1020019. URL: https://www.mdpi.com/2673-7590/1/2/19.

[140] Ines Khoufi, Anis Laouiti, and Cedric Adjih. "A Survey of Recent Extended Variants of the Traveling Salesman and Vehicle Routing Problems for Unmanned Aerial Vehicles". In: *Drones* 3.3 (2019). ISSN: 2504-446X. URL: https://www.mdpi.com/2504-446X/3/3/66.

[141] Marius Kloetzer et al. "Optimal Indoor Goods Delivery Using Drones". In: *2019 24th IEEE International Conference on Emerging Technologies and Factory Automation (ETFA)*. 2019, pp. 1579–1582. DOI: 10.1109/ETFA.2019.8869278.

[142] Nadia Delavarpour et al. "A Technical Study on UAV Characteristics for Precision Agriculture Applications and Associated Practical Challenges". In: *Remote Sensing* 13.6 (2021). ISSN: 2072-4292. DOI: 10.3390/rs13061204. URL: https://www.mdpi.com/2072-4292/13/6/1204.

[143] Beiya Yang and Erfu Yang. "A Survey on Radio Frequency based Precise Localisation Technology for UAV in GPS-denied Environment". In: *Journal of Intelligent & Robotic Systems* 103.3 (Oct. 2021), p. 38. ISSN: 1573-0409. DOI: 10.1007/s10846-021-01500-4. URL: https://doi.org/10.1007/s10846-021-01500-4.

[144] Guoquan Huang. "Visual-Inertial Navigation: A Concise Review". In: *2019 International Conference on Robotics and Automation (ICRA)*. 2019, pp. 9572–9582. DOI: 10.1109/ICRA.2019.8793604.

[145] Nasser Gyagenda et al. "A review of GNSS-independent UAV navigation techniques". In: *Robotics and Autonomous Systems* 152 (2022), p. 104069. ISSN: 0921-8890. DOI: https://doi.org/10.1016/j.robot.2022.104069. URL: https://www.sciencedirect.com/science/article/pii/S0921889022000343.

[146] G Balamurugan, J Valarmathi, and V P S Naidu. "Survey on UAV navigation in GPS denied environments". In: *2016 International Conference on Signal Processing, Communication, Power and Embedded System (SCOPES)*. 2016, pp. 198–204. DOI: 10.1109/SCOPES.2016.7955787.

[147] Rohan Kapoor et al. "UAV Navigation using Signals of Opportunity in Urban Environments: A Review". In: *Energy Procedia* 110 (2017). 1st International Conference on Energy and Power, ICEP2016, 14-16 December 2016, RMIT University, Melbourne, Australia, pp. 377–383. ISSN: 1876-6102. DOI: https://doi.org/10.1016/j.egypro.2017.03.156. URL: https://www.sciencedirect.com/science/article/pii/S1876610217301868.

[148] Zuin Silvia et al. "Ultra Wide Band Indoor Positioning System: analysis and testing of an IPS technology". In: *IFAC-PapersOnLine* 51.11 (2018). 16th IFAC Symposium on Information Control Problems in Manufacturing INCOM 2018, pp. 1488–1492. ISSN: 2405-8963. DOI: https://doi.org/10.1016/j.ifacol.2018.08.292. URL: https://www.sciencedirect.com/science/article/pii/S2405896318314162.

[149] Abdulrahman Alarifi et al. "Ultra Wideband Indoor Positioning Technologies: Analysis and Recent Advances". In: *Sensors* 16.5 (2016). ISSN: 1424-8220. DOI: 10.3390/s16050707. URL: https://www.mdpi.com/1424-8220/16/5/707.

[150] Beiya Yang et al. "High-Precision UWB-Based Localisation for UAV in Extremely Confined Environments". In: *IEEE Sensors Journal* 22.1 (2022), pp. 1020–1029. DOI: 10.1109/JSEN.2021.3130724.

[151] Seongbong Lee et al. "UWB based Relative Navigation and Leader-Follower Formation for UAVs using Maneuvering of a Follower". In: *2021 21st International Conference on Control, Automation and Systems (ICCAS)*. 2021, pp. 239–243. DOI: 10.23919/ICCAS52745.2021.9649880.

[152] Tao Chen, Qi Gao, and MingYu Guo. "An improved multiple UAVs cooperative flight algorithm based on Leader Follower strategy". In: *2018 Chinese Control And Decision Conference (CCDC)*. 2018, pp. 165–169. DOI: 10.1109/CCDC.2018.8407124.

[153] Xin Zhou et al. "Swarm of micro flying robots in the wild". In: *Science Robotics* 7.66 (2022), eabm5954. DOI: 10.1126/scirobotics.abm5954. eprint: https://www.science.org/doi/pdf/10.1126/

scirobotics.abm5954. URL: https://www.science.org/doi/abs/10.1126/scirobotics.abm5954.

[154] Mohammad Obaid, Wafa Johal, and Omar Mubin. "Domestic Drones: Context of Use in Research Literature". In: *Proceedings of the 8th International Conference on Human-Agent Interaction*. HAI '20. Association for Computing Machinery, 2020, 196–203. ISBN: 9781450380546. DOI: 10.1145/3406499.3415076. URL: https://doi.org/10.1145/3406499.3415076.

[155] Jessica R Cauchard et al. "Drone and me: an exploration into natural human-drone interaction". In: *Proceedings of the 2015 ACM international joint conference on pervasive and ubiquitous computing*. 2015, pp. 361–365.

[156] Sujit Rajappa, Heinrich Bülthoff, and Paolo Stegagno. "Design and implementation of a novel architecture for physical human-UAV interaction". In: *The International Journal of Robotics Research* 36.5-7 (2017), pp. 800–819. DOI: 10.1177/0278364917708038. eprint: https://doi.org/10.1177/0278364917708038. URL: https://doi.org/10.1177/0278364917708038.

[157] Dante Tezza and Marvin Andujar. "The State-of-the-Art of Human–Drone Interaction: A Survey". In: *IEEE Access* 7 (2019), pp. 167438–167454. DOI: 10.1109/ACCESS.2019.2953900.

[158] Kari Daniel Karjalainen et al. "Social Drone Companion for the Home Environment: A User-Centric Exploration". In: HAI '17. Association for Computing Machinery, 2017, 89–96. ISBN: 9781450351133. DOI: 10.1145/3125739.3125774. URL: https://doi.org/10.1145/3125739.3125774.

[159] M. A. Rahman et al. "Collab-SAR: A Collaborative Avalanche Search-and-Rescue Missions Exploiting Hostile Alpine Networks". In: *IEEE Access* 6 (2018), pp. 42094–42107.

[160] G. Seminara and D. Fontanelli. "First Responders Robotic Network for Disaster Management". In: *Modelling & Simulation for Autonomous Systems (MESAS)*. Ed. by Jan Mazal. Springer International Publishing, 2018, pp. 350–373. ISBN: 978-3-319-76072-8.

[161] D. St-Onge et al. “Planetary Exploration With Robot Teams: Implementing Higher Autonomy With Swarm Intelligence”. In: *IEEE Robotics Automation Magazine* 27.2 (2020), pp. 159–168.

[162] Z. Dawei et al. “Unmanned Aerial Vehicle (UAV) Photogrammetry Technology for Dynamic Mining Subsidence Monitoring and Parameter Inversion: A Case Study in China”. In: *IEEE Access* 8 (2020), pp. 16372–16386.

[163] T. He, Y. Zeng, and Z. Hu. “Research of Multi-Rotor UAVs Detailed Autonomous Inspection Technology of Transmission Lines Based on Route Planning”. In: *IEEE Access* 7 (2019), pp. 114955–114965.

[164] M. Bacco et al. “Monitoring Ancient Buildings: Real Deployment of an IoT System Enhanced by UAVs and Virtual Reality”. In: *IEEE Access* 8 (2020), pp. 50131–50148.

[165] D. Murugan, A. Garg, and D. Singh. “Development of an Adaptive Approach for Precision Agriculture Monitoring with Drone and Satellite Data”. In: *IEEE Journal of Selected Topics in Applied Earth Observations and Remote Sensing* 10.12 (2017), pp. 5322–5328.

[166] M. William Díaz and J. José Cáceres. “A novel application of drones: thermal diagnosis of electrical and telecommunications infrastructure”. In: *2018 IEEE 38th Central America and Panama Convention (CONCAPAN XXXVIII)*. 2018, pp. 1–6.

[167] Y. Wang et al. “A Novel Positioning System of UAV Based on IMA-GPS Three-Layer Data Fusion”. In: *IEEE Access* 8 (2020), pp. 158449–158458.

[168] A. Carrio et al. “Onboard Detection and Localization of Drones Using Depth Maps”. In: *IEEE Access* 8 (2020), pp. 30480–30490.

[169] O. De Silva, G. K. I. Mann, and R. G. Gosine. “An Ultrasonic and Vision-Based Relative Positioning Sensor for Multirobot Localization”. In: *IEEE Sensors Journal* 15.3 (2015), pp. 1716–1726.

[170] Y. Lin, J. Hyyppä, and A. Jaakkola. “Mini-UAV-Borne LIDAR for Fine-Scale Mapping”. In: *IEEE Geoscience and Remote Sensing Letters* 8.3 (2011), pp. 426–430.

[171] M. L. Rodríguez-Arévalo, J. Neira, and J. A. Castellanos. "On the Importance of Uncertainty Representation in Active SLAM". In: *IEEE Transactions on Robotics* 34.3 (2018), pp. 829–834.

[172] B. Yang et al. "A Novel Trilateration Algorithm for RSSI-Based Indoor Localization". In: *IEEE Sensors Journal* 20.14 (2020), pp. 8164–8172.

[173] M. Li et al. "UWB-Based Localization System Aided With Inertial Sensor for Underground Coal Mine Applications". In: *IEEE Sensors Journal* 20.12 (2020), pp. 6652–6669.

[174] P. Nazemzadeh et al. "Indoor Localization of Mobile Robots through QR Code Detection and Dead Reckoning Data Fusion". In: *IEEE/ASME Transactions on Mechatronics* 22.6 (Dec. 2017), pp. 2588–2599. ISSN: 1083-4435. DOI: 10.1109/TMECH.2017.2762598.

[175] V. Magnago et al. "Ranging-free UHF-RFID Robot Positioning through Phase Measurements of Passive Tags". In: *IEEE Trans. on Instrumentation and Measurement* 69.5 (May 2020), pp. 2408–2418. ISSN: 0018-9456. DOI: 10.1109/TIM.2019.2960900.

[176] V. Magnago et al. "Effective Landmark Placement for Robot Indoor Localization with Position Uncertainty Constraints". In: *IEEE Trans. on Instrumentation and Measurement* 68.11 (Nov. 2019), pp. 4443–4455. ISSN: 1557-9662. DOI: 10.1109/TIM.2018.2887071.

[177] N. Bulusu, J. Heidemann, and D. Estrin. "Adaptive beacon placement". In: *Proceedings 21st International Conference on Distributed Computing Systems*. 2001, pp. 489–498.

[178] Gurkan Tuna, V. Cagri Gungor, and Kayhan Gulez. "An autonomous wireless sensor network deployment system using mobile robots for human existence detection in case of disasters". In: *Ad Hoc Networks* 13 (2014). (1)Special Issue : Wireless Technologies for Humanitarian Relief and (2)Special Issue: Models And Algorithms For Wireless Mesh Networks, pp. 54–68.

[179] Chi Zhang and Xinyu Zhang. "Visible Light Localization Using Conventional Light Fixtures and Smartphones". In: *IEEE Transactions on Mobile Computing* 18.12 (2019), pp. 2968–2983. DOI: 10.1109/TMC.2018.2888973.

[180] Hong Hu et al. "Sound Source Localization Sensor of Robot for TDOA Method". In: *2011 Third International Conference on Intelligent Human-Machine Systems and Cybernetics*. Vol. 2. 2011, pp. 19–22. DOI: 10.1109/IHMSC.2011.75.

[181] Ugur Yayan, Hikmet Yucel, and Ahmet Yazıcı. "A Low Cost Ultrasonic Based Positioning System for the Indoor Navigation of Mobile Robots". In: *Journal of Intelligent & Robotic Systems* 78.3 (June 2015), pp. 541–552.

[182] A.J. Davison. "Real-time simultaneous localisation and mapping with a single camera". In: *Proceedings of the IEEE International Conference on Computer Vision*. 2003, pp. 1403–1410. DOI: 10.1109/iccv.2003.1238654.

[183] Gian Luca Mariottini et al. "Vision-based localization of leader-follower formations". In: *Proceedings of the 44th IEEE Conference on Decision and Control*. IEEE. 2005, pp. 635–640.

[184] Ulric Ferner, Henk Wymeersch, and Moe Z. Win. "Cooperative anchor-less localization for large dynamic networks". In: *2008 IEEE International Conference on Ultra-Wideband*. Vol. 2. 2008, pp. 181–185. DOI: 10.1109/ICUWB.2008.4653381.

[185] Yichen Li, Wenbin Yu, and Xinping Guan. "Current-Aided Multiple-AUV Cooperative Localization and Target Tracking in Anchor-Free Environments". In: *IEEE/CAA Journal of Automatica Sinica* 10.3 (2023), pp. 792–806. DOI: 10.1109/JAS.2022.105989.

[186] Jose A Costa, Neal Patwari, and Alfred O Hero III. "Distributed weighted-multidimensional scaling for node localization in sensor networks". In: *ACM Transactions on Sensor Networks (TOSN)* 2.1 (2006), pp. 39–64.

[187] Luca Santoro et al. "WhereAreYou: an UWB relative tracking system for pedestrian using only ranging information". In: *2023 IEEE International Instrumentation and Measurement Technology Conference (I2MTC)*. IEEE. 2023, pp. 1–6.

[188] Luca Santoro et al. "UWB-based Indoor Positioning System with Infinite Scalability". In: *IEEE Transactions on Instrumentation and Measurement* (2023).

[189] Junlin Yan. "Algorithms for indoor positioning systems using ultra-wideband signals". In: (2010).

[190] Andreas De Preter et al. "Range bias modeling and autocalibration of an UWB positioning system". In: *2019 International Conference on Indoor Positioning and Indoor Navigation (IPIN)*. IEEE. 2019, pp. 1–8.

[191] Vincenzo Di Pietra et al. "Evaluation of positioning and ranging errors for UWB indoor applications." In: *IPIN (Short Papers/Work-in-Progress Papers)*. 2019, pp. 227–234.

[192] D. Fontanelli et al. "An Uncertainty-driven and Observability-based State Estimator for Nonholonomic Robots". In: *IEEE Trans. on Instrumentation and Measurement* 70 (Jan. 2021), pp. 1–12. ISSN: 0018-9456. DOI: 10.1109/TIM.2021.3053066.

[193] F. Farina et al. "Walking Ahead: The Headed Social Force Model". In: *PLOS ONE* 12.1 (Jan. 2017), pp. 1–23. DOI: 10.1371/journal.pone.0169734.

[194] A. Antonucci et al. "Efficient Prediction of Human Motion for Real-Time Robotics Applications with Physics-inspired Neural Networks". In: *IEEE Access* 10 (Dec. 2021), pp. 144–157. ISSN: 2169-3536. DOI: 10.1109/ACCESS.2021.3138614.

[195] Halim Hicheur et al. "Velocity and curvature in human locomotion along complex curved paths: a comparison with hand movements". In: *Experimental brain research* 162.2 (2005), pp. 145–154.

[196] Q. Shi et al. "Anchor self-localization algorithm based on UWB ranging and inertial measurements". In: *Tsinghua Science and Technology* 24.6 (2019), pp. 728–737.

[197] D. Fontanelli. "Perception for Autonomous Systems: A Measurement Perspective on Localisation and Positioning". In: *Instrumentation and Measurement Magazine* (2021). To appear.

[198] Yang Yong and Miao Lingjuan. "GDOP results in all-in-view positioning and in four optimum satellites positioning with GPS PRN codes ranging". In: *PLANS 2004. Position Location and Navigation Symposium (IEEE Cat. No.04CH37556)*. 2004, pp. 723–727. DOI: 10.1109/PLANS.2004.1309065.

[199] I. Sharp, K. Yu, and Y. J. Guo. "GDOP Analysis for Positioning System Design". In: *IEEE Transactions on Vehicular Technology* 58.7 (2009), pp. 3371–3382. DOI: 10.1109/TVT.2009.2017270.

[200] C. Wu, W. Su, and Y. Ho. "A Study on GPS GDOP Approximation Using Support-Vector Machines". In: *IEEE Transactions on Instrumentation and Measurement* 60.1 (2011), pp. 137–145. DOI: 10.1109/TIM.2010.2049228.

[201] Peter H. Dana. "Global Positioning System (GPS) Time Dissemination for Real-Time Applications". In: *Real-Time Systems* 12.1 (Jan. 1997), pp. 9–40. ISSN: 1573-1383. DOI: 10.1023/A:1007906014916.

[202] R. J. Milliken and C. J. Zoller. "Principle of Operation of NAVSTAR and System Characteristics". In: *Navigation* 25.2 (1978), pp. 95–106.

[203] F. Lazzari et al. "Numerical Investigation of an UWB Localization Technique for Unmanned Aerial Vehicles in Outdoor Scenarios". In: *IEEE Sensors Journal* 17.9 (2017), pp. 2896–2903. DOI: 10.1109/JSEN.2017.2684817.

[204] Sertac Karaman and Emilio Frazzoli. "Sampling-based algorithms for optimal motion planning". In: *The international journal of robotics research* 30.7 (2011), pp. 846–894.

[205] Maximilian Beinhofer, Jörg Müller, and Wolfram Burgard. "Effective landmark placement for accurate and reliable mobile robot navigation". In: *Robotics and Autonomous Systems* 61.10 (2013). Selected Papers from the 5th European Conference on Mobile Robots (ECMR 2011), pp. 1060–1069. ISSN: 0921-8890. DOI: https://doi.org/10.1016/j.robot.2012.08.009.

[206] D. Fontanelli et al. "An Uncertainty-Driven and Observability-Based State Estimator for Nonholonomic Robots". In: *IEEE Transactions on Instrumentation and Measurement* 70 (2021), pp. 1–12.

[207] Genichi Taguchi. *Introduction to quality engineering: designing quality into products and processes*. 1986.

[208] Les Kirkup and Robert B Frenkel. *An introduction to uncertainty in measurement: using the GUM (guide to the expression of uncertainty in measurement)*. Cambridge University Press, 2006.

[209] BIPM et al. *Evaluation of measurement data – Guide to the expression of uncertainty in measurement*. JCGM, Sept. 2008.

[210] "A Majorization Algorithm for Solving MDS". In: *Modern Multidimensional Scaling: Theory and Applications*. Springer New York, 2005, pp. 169–197. ISBN: 978-0-387-28981-6. DOI: 10.1007/0-387-28981-X_8. URL: https://doi.org/10.1007/0-387-28981-X_8.

[211] Luca Santoro et al. "UWB Bistatic Radar Sensor: Across Channels Evaluation". In: *IEEE Sensors Letters* 7.10 (2023), pp. 1–4. DOI: 10.1109/LSENS.2023.3307087.